



UNIVERSITAT  
POLITÈCNICA  
DE VALÈNCIA

PROGRAMA DE DOCTORADO EN ARQUITECTURA, EDIFICACIÓN,  
URBANÍSTICA Y PAISAJE

FORM-FINDING AND PERFORMANCE OF  
BENDING-ACTIVE STRUCTURES

PROPOSALS OF APPLICATION TO LIGHTWEIGHT BRACED ARCHES

PHD DISSERTATION

Author:

**JUAN GABRIEL BESSINI MUÑOZ**  
MEng MSc in Civil Engineering

Supervisors:

DR. CARLOS LÁZARO  
DR. SALVADOR MONLEÓN

València, January 2021



Juan Gabriel Bessini Muñoz: *Form-finding and performance of bending-active structures. Proposals of application to lightweight braced arches.*

PhD Dissertation, © January 2021

**SUPERVISORS:**

Carlos Manuel Lázaro Fernández

Dr. Ingeniero de Caminos, Canales y Puertos

Salvador Monleón Cremades

Dr. Ingeniero de Caminos, Canales y Puertos

**LOCATION:**

València, Spain

**E-MAIL:**

[juabesmu@mes.upv.es](mailto:juabesmu@mes.upv.es)



*A mi familia*



## ABSTRACT

Nowadays, modern architecture is focused on the search of efficient uses of technological and sustainable materials, high-tech concept-design-erection processes and the possibility to produce lightweight solutions with maximum elegance in shape. These ideas are reflected on bending-active structures, which recently attracted considerable attention as a new paradigm to build lightweight structures both in research and practice.

The concept 'active bending' refers to a category of structures in which bending is used in the process of shape configuration. Bending-active structural systems include curved rods or shells which have been elastically bent from an initial straight or plane configuration. As of now, the number of realisations is limited; they are mostly experimental ones, with architectural or artistic nature. Form finding of the equilibrium configuration is one of the main difficulties during the conceptual phase, due to the non-linearity of the structural response of the active members, and also to the interaction with other form-active structural elements as membranes or cables, whose geometry cannot be prescribed in advance. Computational form-finding methods for bending-active structures include finite element models with non-linear virtual links that are shortened to reach the final form, or dynamic relaxation (explicit) algorithms to cope with the variables describing the response of the active members.

This PhD thesis aims to provide an indepth analysis on the applicability of the active bending principle to the design of lightweight structures, in particular pedestrian bridges. For that purpose, the work is carried out from three points of view: (a) computational modelling and simulation; (b) structural performance and efficiency; (c) design and construction. First of all, a literature review on the topic and an overview of realisations in the field of bending-active footbridges is provided. In the field of computational modelling, a novel form-finding method based on the geometrically exact rod model (or Reissner-Simo beam theory) is implemented. Numerical examples are also given to show the accuracy of the method. The part of the work related to the analysis of the structural performance and efficiency is focused on the bending-active configuration proposed in this PhD thesis for designing lightweight structures: the *bending-active braced* (or tied) *arch*. This is a simple planar arch composed of a continuous flexible member that is activated by the action of main cables pulling at both ends of the rod, and secondary struts or cables that deviate the main cable and act at certain cross-section of the rod. The computational-analytical part is completed with the development of a numerical procedure based on genetic algorithms to obtain efficient structural configurations. The thesis ends with the design, fabrication and assembling of a bending-active short footbridge made of GFRP tubes using this structural type, held in the laboratory of concept models of the Polytechnic University of Valencia.



## RESUMEN

Hoy en día, la arquitectura moderna está orientada principalmente al empleo eficiente de materiales tecnológicos y sostenibles, la tecnificación del proceso de diseño, proyecto y construcción, y la búsqueda de soluciones muy ligeras. Estas ideas se reflejan en las estructuras flexo-activas, que recientemente han atraído considerable atención como nuevo paradigma para construir estructuras ligeras, tanto en el ámbito de la investigación como en la práctica.

El término 'flexión activa' hace referencia a una categoría de estructuras en las que la flexión se emplea en el proceso de configuración de su forma. Los sistemas estructurales flexo-activos incluyen barras o láminas incurvadas cuya geometría es el resultado de su deformación elástica desde una configuración inicial recta o plana. Hasta el momento, el número de realizaciones es limitado; se trata sobre todo de aplicaciones experimentales con funcionalidad arquitectónica o artística. La obtención de la configuración de equilibrio es una de las principales dificultades que aparecen en la fase de concepción, debido precisamente a la no linealidad de la respuesta estructural de las barras activas, así como a la posible interacción con otros elementos estructurales como membranas o cables, que trabajan por forma, y cuya geometría no se puede fijar de modo arbitrario. Los métodos computacionales de determinación de forma para estructuras flexo-activas incluyen modelos de elementos finitos con cables virtuales no lineales que se acortan hasta alcanzar la configuración final, o algoritmos de relajación dinámica que consideran las variables que caracterizan la deformación de las barras activas.

Esta tesis doctoral tiene por objeto proporcionar un análisis en profundidad de la aplicabilidad del principio de flexión activa al diseño de estructuras ligeras, en particular a los puentes peatonales. Para ello, la investigación se aborda desde tres puntos de vista: a) modelización computacional; b) eficiencia estructural; c) diseño y construcción. En primer lugar, se lleva a cabo una revisión de la bibliografía existente, haciendo hincapié en los trabajos previos en el diseño de pasarelas con flexión activa. En el campo de la modelización computacional, se desarrolla un novedoso método numérico de determinación de forma para estructuras flexo-activas basado en el modelo geoméricamente exacto para piezas alargadas (también conocido como la teoría de vigas de Reissner-Simó). Distintos ejemplos numéricos han sido reproducidos para mostrar la exactitud del método. La parte de la investigación relacionada con el análisis de la eficiencia estructural se centra en el comportamiento del sistema flexo-activo propuesto en esta tesis para el diseño de estructuras ligeras: el *arco flexo-activo arriostrado* (o atirantado). Se trata de un arco plano compuesto por una barra flexible y continuo que se activa por la acción de los cables principales que tiran de ambos extremos de la varilla, y de los puntales o cables secundarios que desvían el cable principal y actúan en ciertas secciones transversales. La parte computacional-analítica se completa con el desarrollo de un procedimiento numérico basado en algoritmos genéticos, con el fin de obtener configuraciones estructurales eficientes. La tesis finaliza con el diseño, fabricación y montaje de una pasarela flexo-activa hecha con tubos PRFV utilizando este tipo estructural, realizada en el laboratorio de modelos de la Universitat Politècnica de València.



## RESUM

Hui dia, l'arquitectura moderna està orientada principalment a l'ús eficient de materials tecnològics i sostenibles, la tecnificació del procés de disseny, projecte i construcció, i la cerca de solucions molt lleugeres. Aquestes idees es reflecteixen en les estructures flexo-actives, que recentment han atret considerable atenció com a nou paradigma per a construir estructures lleugeres, tant en l'àmbit de la investigació com en la pràctica.

El terme 'flexió activa' fa referència a una categoria d'estructures en les quals la flexió s'empra en el procés de configuració de la seua forma. Els sistemes estructurals flexo-actius inclouen barres o làmines incorbades, la geometria de les quals és el resultat de la seua deformació elàstica des d'una configuració inicial recta o plana. Fins al moment, el nombre de realitzacions és limitat; es tracta sobretot d'aplicacions experimentals amb funcionalitat arquitectònica o artística. L'obtenció de la configuració d'equilibri és una de les principals dificultats que apareixen en la fase de concepció, degut precisament a la no linealitat de la resposta estructural de les barres actives, així com a la possible interacció amb altres elements estructurals com a membranes o cables, que treballen per forma, i la geometria de la qual no es pot fixar de manera arbitrària. Els mètodes computacionals de determinació de forma per a estructures flexo-actives inclouen models d'elements finits amb cables virtuals no lineals que s'escurcen fins a aconseguir la configuració final, o algorismes de relaxació dinàmica que consideren les variables que caracteritzen la deformació de les barres actives.

Aquesta tesi doctoral té per objecte proporcionar una anàlisi en profunditat de l'aplicabilitat del principi de flexió activa al disseny d'estructures lleugeres, en particular als ponts per als vianants. Per a això, la investigació s'aborda des de tres punts de vista: a) modelització computacional; b) eficiència estructural; c) disseny i construcció. En primer lloc, es duu a terme una revisió de la bibliografia existent, amb recalcament en els treballs previs en el disseny de passarel·les amb flexió activa. En el camp de la modelització computacional, es desenvolupa un nou mètode numèric de determinació de forma per a estructures flexo-actives basat en el model geomètricament exacte per a peces allargades (també conegut com la teoria de bigues de Reissner-Simó). Diferents exemples numèrics han sigut reproduïts per a mostrar l'exactitud del mètode. La part de la investigació relacionada amb l'anàlisi de l'eficiència estructural se centra en el comportament del sistema flexo-actiu proposat en aquesta tesi doctoral per al disseny d'estructures lleugeres: l' *arc flexo-actiu esbiaixat* (o lligat). Es tracta d'un arc pla compost per un membre flexible i continu que s'activa per l'acció dels cables principals que tiren de tots dos extrems de la vareta, i dels puntals o cables secundaris que desvien el cable principal i actuen en certa secció transversal de la vareta. La part computacional-analítica es completa amb el desenvolupament d'un procediment numèric basat en algorismes de tipus genètic, amb la finalitat d'obtindre configuracions estructurals eficients. La tesi finalitza amb el disseny, fabricació i muntatge d'una passarel·la flexo-activa feta amb tubs PRFV utilitzant aquest tipus estructural, realitzada en el laboratori de models de la Universitat Politècnica de València.



## PUBLICATIONS

The author, together with other colleagues, has published a number of peer-reviewed papers dealing with aspects of the work herein:

- 2021 **Shape generation of bending-active braced arches based on elastica curves**  
J. Bessini, S. Monleón, J. Casanova and C. Lázaro, In *Journal of the International Association for Shell and Spatial Structures*; submitted.
- 2020 **Design of bending-active tied arches by using a multi-objective optimization method**  
J. Bessini, P. Shepherd, S. Monleón and C. Lázaro, In *Structures*. Vol. 27, pp. 2319 – 2328.
- 2019 **Efficiency-based design of bending-active tied arches**  
J. Bessini, C. Lázaro, J. Casanova and S. Monleón, In *Engineering Structures*. Vol. 200, 109681.
- 2018 **Mechanical models in computational form finding of bending-active structures**  
C. Lázaro, J. Bessini and S. Monleón, In *International Journal of Space Structures*. Volume 33 (2), pp. 86 – 97.
- 2017 **A form-finding method based on the geometrically exact rod model for bending-active structures**  
J. Bessini, C. Lázaro and S. Monleón, In *Engineering Structures*. Volume 152, pp. 549 – 558.

Some ideas and figures have been presented in the following conferences:

- 2019 **Multi-objective optimization-based design for bending-active tied arches**  
J. Bessini, C. Lázaro and P. Shepherd, In *Proceedings of the IASS Symposium 2019*. International Association for Shell and Spatial Structures.
  
- 2018 **Design of an experimental lightweight footbridge based on the active bending principle**  
J. Bessini, R. Piñol, C. Lázaro and S. Monleón, In *Proceedings of the IASS Symposium 2018*. International Association for Shell and Spatial Structures.
  
- 2018 **Shape and performance of bending-active tied arches**  
C. Lázaro, J. Bessini and S. Monleón, In *Proceedings of the IASS Symposium 2018*. International Association for Shell and Spatial Structures.
  
- 2017 **Tangent stiffness in point-loaded elastica arches**  
C. Lázaro, S. Monleón and J. Bessini, In *Proceedings of the IASS Symposium 2017*. International Association for Shell and Spatial Structures.
  
- 2017 **Form-finding of bending-active structures using kinematic constraints**  
J. Bessini, C. Lázaro and S. Monleón, In *Proceedings of the IASS Symposium 2017*. International Association for Shell and Spatial Structures.
  
- 2016 **A review on geometrically exact models for very flexible rods**  
C. Lázaro and S. Monleón, J. Bessini and J. Casanova, In *Proceedings of the IASS Symposium 2016*. International Association for Shell and Spatial Structures.

## ACKNOWLEDGEMENTS

It seems like only yesterday that this journey began. I was finishing the Master's Degree in Structures in Madrid when I realised that I wanted to continue studying and learning about structures. On one of my visits to Valencia, I met with Prof. Salvador Monleón, who had been the supervisor of my final dissertation for the Civil Engineering Degree. I was sure that if I did a PhD, it would be with him. He immediately introduced me to Prof. Carlos Lázaro, whom I did not know despite having studied all the subjects on structures with his notes. He suggested that I did my thesis on *active bending*. I had no idea, but I accepted (a year after I started, I still didn't know what active bending was). Five years later, I can say that it was the best decision of my life. During this time, I have not only acquired knowledge of structures; I have learned to be self-critical, patient and rigorous; to overcome the difficult times with serenity, and above all, to work with love and passion. Personal skills that define a good professional and that I have learned from working with them. I am enormously grateful to Prof. Lázaro, for his kindness and patient guidance, for trusting me and encouraging me to always take tortuous ways and for sharing his extraordinary expertise in structural design. I would also like to thank Prof. Monleón, who originated my passion for the world of structures and bridge design, for giving me the opportunity to begin this journey and for being there whenever needed.

I wish to thank to Prof. Mario Lázaro for his valuable contribution in the last stage of this research. His expertise on dynamics and willingness to help have been crucial to design the experimental tests. I am also grateful to Roberto Piñol, who worked with me during his Master's thesis and whose outcomes have been important for this doctoral thesis. Furthermore, I would like to express my gratitude to a wonderful group of people who welcomed me and showed their friendship during this time: Prof. Josep Casanova, Prof. Carmen Castro, Prof. María José Pelufo, Prof. Lourdes Aznar and Prof. José Luís Bonet. Thanks a lot for the infinite number of coffees, for the moments we shared in *the Galileo* and for the constant encouragement. Finally, I am grateful to Prof. Pedro Museros, Prof. Juan Francisco Moyá and Prof. Carlos Sánchez for their inspiring conversations and continued support.

An important part of this research has been conducted at the University of Bath. I wish to thank Prof. Paul Shepherd for welcoming me as a visiting researcher in the Department of Architecture and Civil Engineering as well as for his valuable feedback about my research. I extend my thanks also to my colleagues at the University of Bath: Antiopi, Elisabetta, Beatriz, Daniel, Yasser, Lori, Sharareh, Rana, Carlos, Kaveh, Anna, Ben, Noor, Auri, Valeria, Federica, Pooja and Quingpeng Li. I felt at home thanks to them.

Most of all, I would like to express my deep gratitude to my parents for their relentless support. All that I am I owe to them. For last, I wish to sincerely thank Patri, for being patiently by my side during the years needed to complete my work and making brighter every day of my life.



# CONTENTS

|       |   |    |
|-------|---|----|
| 1     | INTRODUCTION  | 1  |
| 1.1   | Motivation  | 3  |
| 1.2   | Research objectives   | 4  |
| 1.3   | Dissertation outline  | 5  |
| 2     | STATE OF THE ART  | 7  |
| 2.1   | The active bending principle  | 7  |
| 2.2   | Required material properties  | 9  |
| 2.3   | Determination of the configuration  | 10 |
| 2.3.1 | Models based on discrete mechanics  | 12 |
| 2.3.2 | Models based on finite-difference discretisations                         | 13 |
| 2.3.3 | Models based on finite element discretisations                            | 15 |
| 2.4   | Previous works on the structural performance of bending-active structures | 17 |
| 3     | A FORM-FINDING METHOD BASED ON THE GEM FOR BENDING-ACTIVE STRUCTURES      | 19 |
| 3.1   | Introduction  | 19 |
| 3.1.1 | Outline of the chapter  | 20 |
| 3.2   | The geometrically exact rod model   | 20 |
| 3.2.1 | Basic kinematics  | 20 |
| 3.2.2 | Variation of the generalised strain measures                              | 22 |
| 3.2.3 | Equations of static equilibrium   | 22 |
| 3.2.4 | Equations of dynamic equilibrium  | 23 |
| 3.2.5 | Constitutive equations  | 23 |
| 3.3   | The dynamic relaxation method   | 24 |
| 3.4   | Fundamentals of the method  | 24 |
| 3.4.1 | Application of D'Alembert's principle                                     | 24 |
| 3.4.2 | Determination of element end forces                                       | 25 |
| 3.4.3 | Strains associated to rotations   | 26 |
| 3.4.4 | Strains associated to translations  | 27 |
| 3.5   | Numerical implementation  | 28 |
| 3.5.1 | Criterion for convergency   | 29 |
| 3.5.2 | Boundary conditions   | 29 |
| 3.6   | Numerical tests   | 30 |
| 3.6.1 | The elastica and the circular beam  | 30 |
| 3.6.2 | Bathe and Bolourchi cantilever beam                                       | 32 |
| 3.6.3 | Combined bending and torsion  | 32 |
| 3.6.4 | Shear deformability test  | 36 |
| 3.7   | Summary   | 37 |
| 4     | THE BENDING-ACTIVE TIED ARCH  | 39 |
| 4.1   | Introduction  | 39 |
| 4.1.1 | Outline of the chapter  | 41 |
| 4.2   | A brief review of the inflexional elastica                                | 41 |
| 4.2.1 | Configuration of the elastica   | 42 |
| 4.2.2 | Section forces  | 43 |

|         |  |     |
|---------|--|-----|
| 4.2.3   | Scalability of the solution  | 43  |
| 4.3     | Self-stress states in bending-active tied arches                       | 44  |
| 4.3.1   | Notation   | 44  |
| 4.3.2   | Equilibrium and compatibility conditions at joints                     | 45  |
| 4.4     | Direct determination of self-stress configurations                     | 47  |
| 4.4.1   | Examples   | 49  |
| 4.5     | Computation of self-stress configurations under additional constraints | 53  |
| 4.6     | Summary  | 57  |
| 5       | EFFICIENCY-BASED DESIGN OF BENDING-ACTIVE TIED ARCHES                  | 59  |
| 5.1     | Introduction   | 59  |
| 5.1.1   | Outline of the chapter   | 60  |
| 5.2     | Stress levels after activation in elastica semi-waves                  | 60  |
| 5.2.1   | Evaluation of the utilisation ratio                                    | 60  |
| 5.3     | Shape of the rod between deviators after activation                    | 64  |
| 5.4     | Numerical tests on bending-active tied arches with three deviators     | 66  |
| 5.4.1   | Relationship between shape and activation forces                       | 67  |
| 5.4.2   | Stress levels in the rod after activation                              | 67  |
| 5.4.3   | Structural performance of cables                                       | 70  |
| 5.4.4   | Performance for serviceability limit state (SLS)                       | 72  |
| 5.4.5   | Performance for ultimate limit state (ULS)                             | 72  |
| 5.5     | Example  | 73  |
| 5.6     | Procedure to design bending-active tied arches with n deviators        | 74  |
| 5.7     | Summary  | 76  |
| 6       | DESIGN OF BENDING-ACTIVE TIED ARCHES BY USING A MOO METHOD             | 77  |
| 6.1     | Introduction   | 77  |
| 6.1.1   | Outline of the chapter   | 78  |
| 6.2     | Problem description  | 78  |
| 6.3     | The multi-objective optimisation problem                               | 80  |
| 6.3.1   | Fitness  | 82  |
| 6.3.2   | Selection  | 84  |
| 6.3.3   | Recombination and evolution  | 84  |
| 6.3.4   | Sensitivity study  | 84  |
| 6.4     | Results  | 85  |
| 6.5     | Structural analysis and verification                                   | 90  |
| 6.6     | Summary  | 93  |
| 7       | EXPERIMENTAL FOOTBRIDGE BASED ON THE ACTIVE BENDING PRINCIPLE          | 95  |
| 7.1     | Introduction   | 95  |
| 7.1.1   | Outline of the chapter   | 95  |
| 7.2     | Design   | 96  |
| 7.2.1   | Specifications   | 96  |
| 7.2.2   | Materials  | 96  |
| 7.2.3   | Conceptual design  | 96  |
| 7.2.4   | Determination of the structural configuration                          | 99  |
| 7.3     | Verification of limit states   | 102 |
| 7.3.1   | Self-stress state  | 102 |
| 7.3.2   | Dead load  | 105 |
| 7.3.3   | Serviceability state   | 105 |
| 7.3.3.1 | Symmetric load case  | 105 |

|                 |  |     |
|-----------------|--|-----|
| 7.3.3.2         | Non-symmetric load case                      | 106 |
| 7.3.3.3         | Torsional load case                          | 107 |
| 7.4             | Fabrication                                  | 108 |
| 7.4.1           | Fabrication of the nodes                     | 109 |
| 7.4.2           | Assembling process                           | 112 |
| 7.4.3           | Future works                                 | 121 |
| 7.5             | Summary                                      | 121 |
| 8               | CONCLUSIONS AND FUTURE RESEARCH              | 123 |
| 8.1             | Summary of results                           | 123 |
| 8.2             | Main conclusions                             | 126 |
| 8.3             | Future lines of research                     | 127 |
| <b>APPENDIX</b> |  |     |
| A               | NUMERICAL RESULTS FOR THE PROTOTYPE FE MODEL | 131 |
| A.1             | Form-finding process                         | 131 |
| A.2             | Load testing                                 | 135 |
| A.2.1           | Dead load (pallets)                          | 135 |
| A.2.2           | Symmetric load case                          | 137 |
| A.2.3           | Non-symmetric load case                      | 139 |
| A.2.4           | Torsional load case                          | 141 |
|                 | BIBLIOGRAPHY                                 | 147 |



## LIST OF FIGURES

|           |   |    |
|-----------|---|----|
| Figure 1  | Some iconic gridshells built in the last years.   | 2  |
| Figure 2  | Activation process of an initially straight rod.  | 7  |
| Figure 3  | Examples of vernacular architecture built by means of elastically bent elements [97].   | 8  |
| Figure 4  | Mannheim Multihalle [43].   | 8  |
| Figure 5  | Experimental prototypes for bending-active footbridges.   | 9  |
| Figure 6  | A physical model subject to bending and torsion effects. (Bending of developable surfaces has been studied in [93].)  | 11 |
| Figure 7  | Discretisation in Adriaenssens and Barnes [3].  | 14 |
| Figure 8  | Discretisation in Barnes <i>et al.</i> [8].   | 14 |
| Figure 9  | Discretisation in Du Peloux <i>et al.</i> [39].   | 15 |
| Figure 10 | Co-rotational setup.  | 16 |
| Figure 11 | Simplified co-rotational setup.   | 16 |
| Figure 12 | Total stiffness of elastica arches with angle at the inflexion equal to $\phi_0$ for different values of rod slenderness $\lambda$ [58].  | 18 |
| Figure 13 | Kinematics of Reissner-Simo's model [60].   | 21 |
| Figure 14 | Scheme of forces and moments acting on the element $ij$ and the node $j$  | 24 |
| Figure 15 | A typical element showing the nodal frames and the reference frame. $\Lambda_r$ is computed through spherical interpolation between $\Lambda_i$ and $\Lambda_j$ .   | 27 |
| Figure 16 | Form-finding of the elastica and the circular beam defined by the same local reference frames at the beam ends.   | 30 |
| Figure 17 | Curvatures for the <i>elastica</i> (Elas.) in blue and curvatures for the circular beam (Cir.) in brown. Form-finding (F.F.) and theoretical solutions (T.).  | 31 |
| Figure 18 | Evolution of the curve lengths for the <i>elastica</i> and the circular beam during the form-finding process.   | 31 |
| Figure 19 | Evolution of the form-finding process of an <i>elastica</i> curve and its length (L) at different stages.   | 33 |
| Figure 20 | Original problem of the Bathe and Bolourchi cantilever beam.  | 34 |
| Figure 21 | Evolution of the kinetic energies for the Bathe and Bolourchi cantilever beam. Figure a) shows the initial geometry. Figure b) corresponds to the geometry at step 100. Figure c) shows the final equilibrium geometry. | 34 |
| Figure 22 | Coordinates X-Y-Z using the form-finding method (F.F.) and the implicit numerical solution based on Simo's theory (I.M.) for the Bathe and Bolourchi cantilever beam.   | 35 |
| Figure 23 | An initially straight rod is bent up to reach vertical tangents at supports and then twisted by rotating $30^\circ$ its ends.   | 36 |

|           |  |
|-----------|--|
| Figure 24 | Shear deformations for the <i>elastica</i> and a beam where transverse shear is not negligible. 37   |
| Figure 25 | Bending-active tied arch. 40   |
| Figure 26 | Full (notional) elastica corresponding to segment $i$ . 41   |
| Figure 27 | Inflexional elastica. 42   |
| Figure 28 | Elasticas (non-dimensional coordinates) for $\theta_0 = n\pi/20$ and $n \in \{2, 3, \dots, 17, 18\}$ . 44  |
| Figure 29 | Notation. 45   |
| Figure 30 | Equilibrium of nodes and elastica sections. 46   |
| Figure 31 | Cables, deviators and force polygon. 46  |
| Figure 32 | Generic bending-active tied arch with $n = 5$ elastica sections. 49  |
| Figure 33 | Bending-active tied arch with $n = 5$ elastica sections and perpendicular deviators. 50  |
| Figure 34 | Symmetric bending-active tied arch with $n = 4$ elastica sections. 52  |
| Figure 35 | Symmetric bending-active arch with $n = 4$ elastica sections of equal length (example 1). 55   |
| Figure 36 | Symmetric bending-active tied arch corresponding to the example 2. 56  |
| Figure 37 | Symmetric bending-active tied arch corresponding to the example 3. 56  |
| Figure 38 | Utilisation ratio of elastica semi-waves with rectangular cross-section $\Psi = 0.33$ , angle at the inflexion $\theta_0$ , material properties $E = 30$ GPa and $f_u = 400$ MPa, and different values of rod slenderness $\bar{\lambda}$ . 62   |
| Figure 39 | Influence of the shape factor $\Psi$ on the utilisation ratio of elastica semi-waves with rectangular cross-section, angle at the inflexion $\theta_0$ and different values of rod slenderness $\bar{\lambda}$ . 63  |
| Figure 40 | Influence of the term relative to axial forces on the utilisation ratio of elastica semi-waves with rectangular cross-section, angle at the inflexion $\theta_0$ and different values of rod slenderness $\bar{\lambda}$ . 63  |
| Figure 41 | Influence of the ratio $f_u/E$ on the utilisation ratio of elastica semi-waves with rectangular cross-section, angle at the inflexion $\theta_0$ and different values of rod slenderness $\bar{\lambda}$ . 64  |
| Figure 42 | Axial forces $N$ due to activation process. 65   |
| Figure 43 | Shear forces $V$ due to activation process. 65   |
| Figure 44 | Bending moments $M$ due to activation process. 65  |
| Figure 45 | Definition of the input parameters. 66   |
| Figure 46 | Different configurations for bending-active tied arches with three equally spaced deviators. 68  |
| Figure 47 | Relation between activation force ratios and non-dimensional shape ratios for a bending-active braced arch with three deviators equally spaced and perpendicular to the rod, where the length of central deviator equals 10% of the length of the rod and the length of lateral deviators equals 75% of the central deviator. 69 |

|           |  |
|-----------|--|
| Figure 48 | Stress ratio levels after activation in terms of rod slenderness and rise-to-span for a bending-active braced arch with three deviators equally spaced and perpendicular to the rod, where the length of central deviator equals 10% of the length of the rod and the length of lateral deviators equals 75% of the central deviator. 69 |
| Figure 49 | Loading model. 70  |
| Figure 50 | Configurations with the same rod slenderness $\bar{\lambda} = 1.5$ and different cable-rod slenderness ratios: a) $\bar{\lambda}_c/\bar{\lambda} = 5$ and b) $\bar{\lambda}_c/\bar{\lambda} = 15$ . 71   |
| Figure 51 | Region where stresses in cables are in the interval between 10% and 70% of the maximum allowable stress. 71  |
| Figure 52 | Dimensionless deflections from $L/200$ to $L/1000$ for different cable-rod slenderness ratios and a given load in terms of slenderness and shape. 72   |
| Figure 53 | Region where the utilisation ratio in the rod is less than 1 for the ultimate limit state. 73  |
| Figure 54 | Design diagram for the example of the section 5.5. 74  |
| Figure 55 | Procedure to design a bending-active tied arch with an arbitrary number of deviators. 75   |
| Figure 56 | Symmetric loading pattern. 80  |
| Figure 57 | Non-symmetric loading pattern. 80  |
| Figure 58 | Flowchart of the design method. 81   |
| Figure 59 | Fitness functions considered in the multi-objective optimisation problem. 83   |
| Figure 60 | Initial population. 86   |
| Figure 61 | Distribution of the population and results (red points) at final iteration. 87   |
| Figure 62 | Evolution of the fitness function. 88  |
| Figure 63 | Utilisation ratios of the rod and cables after activation (FF) and for the ultimate limit state (ULS). 88  |
| Figure 64 | Configuration for bending-active tied arches at different iterations. 89   |
| Figure 65 | Vertical deflections (mm) due to the non-symmetric loading pattern for the serviceability limit state (optimal solution). 90   |
| Figure 66 | Vertical deflections (mm) due to the non-symmetric loading pattern for the serviceability limit state (bad solution). 90   |
| Figure 67 | Bending moments $M$ (kN.m) in the rod due to activation process (optimal solution). 91   |
| Figure 68 | Bending moments $M$ (kN.m) in the rod due to activation process (bad solution). 91   |
| Figure 69 | Axial forces $N$ (kN) in the rod and deviators due to activation process (optimal solution). 91  |
| Figure 70 | Axial forces $N$ (kN) in the rod and deviators due to activation process (bad solution). 92  |
| Figure 71 | Bending moments $M$ (kN.m) in the rod due to the design loads for the ultimate limit state (optimal solution). 92  |

|            |   |
|------------|---|
| Figure 72  | Axial forces $N$ in the rod due to the design loads for the ultimate limit state (optimal solution). 92   |
| Figure 73  | Conceptual model with 3D-printed joints and X-shaped deviators. 97  |
| Figure 74  | Force diagram after connecting the bending-active arches. In red colour, internal forces on the rod exerted by the struts. In pink colour, their resultant, which is (ideally) vertical. 98 |
| Figure 75  | Side perspective rendered view of the prototype. 98   |
| Figure 76  | Definition of the parameters for the bending-active tied arch. 99   |
| Figure 77  | Relation between axial forces in deviators after activation for different ratios $h_q/h_m$ . 100  |
| Figure 78  | Dimensionless inverse of the deflections at mispan for different ratios $h_q/h_m$ and rod slenderness. 100  |
| Figure 79  | Stress levels after activation in terms of rod slenderness $\bar{\lambda}$ and rise-to-span of the structure $f/a$ . 101  |
| Figure 80  | Increase in stiffness $\Delta K$ after activation in terms of rod slenderness $\bar{\lambda}$ and rise-to-span of the structure $f/a$ . 102   |
| Figure 81  | Simulation of the assembling process of the structure. 104  |
| Figure 82  | Detail of deviators; 82a at midspan, 82b at quarters. 108   |
| Figure 83  | Experimental footbridge based on the active-bending principle. 109  |
| Figure 84  | Reproduction of the custom-made joints by using 3D printing. 110  |
| Figure 85  | Detail of the custom-made steel joints. 111   |
| Figure 86  | Erection process of the prototype (a). 113  |
| Figure 87  | Erection process of the prototype (b). 114  |
| Figure 88  | Erection process of the prototype (c). 115  |
| Figure 89  | Erection process of the prototype (d). 116  |
| Figure 90  | Erection process of the prototype (e). 117  |
| Figure 91  | Erection process of the prototype (f). 118  |
| Figure 92  | Erection process of the prototype (g). 119  |
| Figure 93  | Erection process of the prototype (h). 120  |
| Figure 94  | The experimental footbridge prototype in service. 121   |
| Figure 95  | Bending-active short footbridge made of ultra-high-performance concrete (UHPC). 128   |
| Figure 96  | Axial forces $N$ (kN) in the rod and deviators due to activation process (stage (a)). 131   |
| Figure 97  | Bending moments $M_y$ (kN.m) in the rod and deviators due to activation process (stage (a)). 131  |
| Figure 98  | Bending moments $M_z$ (kN.m) in the rod and deviators due to activation process (stage (a)). 132  |
| Figure 99  | Axial forces $N$ (kN) in cables due to activation process (stage (a)). 132  |
| Figure 100 | Axial forces $N$ (kN) in the rod and deviators due to activation process (stage (e)). 132   |
| Figure 101 | Bending moments $M_y$ (kN.m) in the rod and deviators due to activation process (stage (e)). 132  |
| Figure 102 | Bending moments $M_z$ (kN.m) in the rod and deviators due to activation process (stage (e)). 133  |

|            |  |     |
|------------|--|-----|
| Figure 103 | Axial forces $N$ (kN) in cables due to activation process (stage (e)).   | 133 |
| Figure 104 | Axial forces $N$ (kN) in midspan strut due to activation process (stage (c)).  | 133 |
| Figure 105 | Axial forces $N$ (kN) in midspan strut due to activation process (stage (d)).  | 134 |
| Figure 106 | Axial forces $N$ (kN) in quarter strut due to activation process (stage (d)).  | 134 |
| Figure 107 | Axial forces $N$ (kN) in midspan and quarter struts due to activation process (stage (e)).                           | 134 |
| Figure 108 | Axial forces $N$ (kN) in end struts due to activation process (stage (e)).   | 135 |
| Figure 109 | Loading pattern (kN) due to the installation of the pallets.   | 135 |
| Figure 110 | Axial forces $N$ (kN) in the rod and deviators due to the installation of the pallets.                               | 136 |
| Figure 111 | Bending moments $M_y$ (kN.m) in the rod and deviators due to the installation of the pallets.                        | 136 |
| Figure 112 | Bending moments $M_z$ (kN.m) in the rod and deviators due to the installation of the pallets.                        | 136 |
| Figure 113 | Axial forces $N$ (kN) in cables due to the installation of the pallets.  | 136 |
| Figure 114 | Vertical deflections (mm) due to the installation of the pallets.  | 137 |
| Figure 115 | Loading pattern (kN) due to the symmetric loading pattern for the load testing.                                      | 137 |
| Figure 116 | Axial forces $N$ (kN) in the rod and deviators due to the symmetric loading pattern for the load testing.            | 138 |
| Figure 117 | Bending moments $M_y$ (kN.m) in the rod and deviators due to the symmetric loading pattern for the load testing.     | 138 |
| Figure 118 | Bending moments $M_z$ (kN.m) in the rod and deviators due to the symmetric loading pattern for the load testing.     | 138 |
| Figure 119 | Axial forces $N$ (kN) in cables due to the symmetric loading pattern for the load testing.                           | 138 |
| Figure 120 | Vertical deflections (mm) due to the symmetric loading pattern for the load testing.                                 | 139 |
| Figure 121 | Loading pattern (kN) due to the non-symmetric loading pattern for the load testing.                                  | 139 |
| Figure 122 | Axial forces $N$ (kN) in the rod and deviators due to the non-symmetric loading pattern for the load testing.        | 140 |
| Figure 123 | Bending moments $M_y$ (kN.m) in the rod and deviators due to the non-symmetric loading pattern for the load testing. | 140 |
| Figure 124 | Bending moments $M_z$ (kN.m) in the rod and deviators due to the non-symmetric loading pattern for the load testing. | 140 |
| Figure 125 | Axial forces $N$ (kN) in cables due to the non-symmetric loading pattern for the load testing.                       | 140 |
| Figure 126 | Vertical deflections (mm) due to the non-symmetric loading pattern for the load testing.                             | 141 |
| Figure 127 | Loading pattern (kN) due to the torsional load case for the load testing.  | 141 |

|            |  |
|------------|--|
| Figure 128 | Axial forces $N$ (kN) in the rod and deviators due to the torsional load case for the load testing. 142        |
| Figure 129 | Bending moments $M_y$ (kN.m) in the rod and deviators due to torsional load case for the load testing. 142     |
| Figure 130 | Bending moments $M_z$ (kN.m) in the rod and deviators due to the torsional load case for the load testing. 142 |
| Figure 131 | Axial forces $N$ (kN) in cables due to the torsional load case for the load testing. 143                       |
| Figure 132 | Vertical deflections (mm) due to the torsional load case for the load testing. 143                             |

## LIST OF TABLES

|          |  |    |
|----------|--|----|
| Table 1  | Comparison between references using finite-difference-like discretisations.  | 15 |
| Table 2  | Section properties of the <i>elastica</i> and the circular beam.   | 30 |
| Table 3  | Material and section properties of the Bathe and Bolourchi cantilever beam.  | 32 |
| Table 4  | Section properties for the case of bending and torsion effects.  | 35 |
| Table 5  | Vertical and horizontal relative deflection for the bent and twisted beam taking into account different number of elements in both form-finding method (F.F.) and implicit method based on Simo's theory (I.M.). | 35 |
| Table 6  | Section properties of the beam used in the shear deformability test.   | 36 |
| Table 7  | Variables related to self-stressing forces.  | 47 |
| Table 8  | Variables related to the form of the elastic rod.  | 47 |
| Table 9  | Size and force scaling variables.  | 47 |
| Table 10 | Equilibrium and compatibility equations.   | 48 |
| Table 11 | Prescribed and computed variables in the direct method.  | 49 |
| Table 12 | Prescribed variables and computed unknowns for the generic case.   | 50 |
| Table 13 | Prescribed variables and computed unknowns corresponding to the generic case with perpendicular deviators.   | 51 |
| Table 14 | Prescribed and computed variables in a symmetric structure with even number of <i>elastica</i> sections (direct method).   | 52 |
| Table 15 | Equations in a symmetric structure with even number of <i>elastica</i> sections.   | 52 |
| Table 16 | Prescribed variables and computed unknowns in the symmetric example.   | 52 |
| Table 17 | Prescribed and computed variables in a symmetric structure with odd number of <i>elastica</i> sections (direct method).  | 53 |
| Table 18 | Equations in a symmetric structure with odd number of <i>elastica</i> sections.  | 53 |
| Table 19 | Prescribed variables and computed unknowns in the example 1.   | 55 |
| Table 20 | Prescribed variables and computed unknowns in the example 2.   | 56 |
| Table 21 | Prescribed variables and computed unknowns in the example 3.   | 57 |
| Table 22 | Shape factor for circular hollow cross-sections.   | 61 |
| Table 23 | Section forces and static invariants of the rod segment A-E.   | 66 |

|          |  |    |
|----------|--|----|
| Table 24 | Values of activation forces and resulting geometric ratios for the sequence of bending-active tied arches (1-6) shown in Fig. 46. The definition of the parameters can be found in Fig. 45. 67 |    |
| Table 25 | Material properties. 78  |    |
| Table 26 | Upper and lower bounds for the input variables in the multi-objective optimisation method. 79  |    |
| Table 27 | Experiments to select the population size and probability of mutation. 85  |    |
| Table 28 | Form-finding variables for different configurations. 85  |    |
| Table 29 | Utilisation ratios of the rod and cables for the solution reached. 85  | 85 |
| Table 30 | Maximum deflections (in mm) for the solution reached. 86   |    |
| Table 31 | Material properties of the prototype. 96   |    |
| Table 32 | Section forces in the rod and cables during the activation process. 103  |    |
| Table 33 | Section forces in the horizontal struts during the activation process. 103   |    |
| Table 34 | Section forces in the rod and cables due to the installation of the pallets. 105   |    |
| Table 35 | Section forces in the rod and cables due to the symmetric load case for the load testing. 106  |    |
| Table 36 | Section forces in the rod and cables due to the non-symmetric load case for the load testing. 106  |    |
| Table 37 | Section forces in the rod and cables due to the torsion load case for the load testing. 107  |    |

” *The straight line belongs to men, the curved one to God.*

– **Antonio Gaudí**  
(Architect)

In the realm of structures, efficiency is driven by the combination of adequate material properties and structural configuration. Well-designed curved shapes, as in the case of arches and shells, create effective mechanisms to transmit loads and lead to lightweight structural solutions with low material consumption. The 20<sup>th</sup> century has witnessed the introduction of two extremely efficient and successful surface structural systems for roofs and other structural applications: thin shells and tensile structures. The development of thin shells was closely related to the expansion of reinforced concrete. Large scale tensile structures were made possible thanks to the application of novel analysis techniques and materials (high-strength steel and acrylic cladding –as in Munich’s Olympia Stadium– and later, structural fabric membranes).

Paying attention to traditional building methods, there are many examples that are source of inspiration to search for lightweight as well as environment-aware constructions. In different places of the globe, dwellings are built bending and joining very flexible rods, usually made of bamboo or straw bundles. These constructions are, despite their lightness, remarkably stiff because of their shape, reached through elastic deformation. They have also a very low carbon footprint due to the use of natural materials and the low material consumption.

The idea to build using elastic deformation as a strategy to achieve a structural shape was adopted by Frei Otto who designed and built in 1975 the Multihalle in Mannheim (Germany), a temporary (but still standing) roof for an exhibition pavilion, made of timber laths that were assembled on the ground, lifted to the final position, fixed to the ground and stabilised with cables [43]. The Multihalle marked the beginning of a new type of structures called elastic gridshells [72]. This denomination refers to spatial structures composed of a grid of continuous slender members that achieve its final shape by means of elastic bending (Fig. 1a). It combines the advantage of traditional construction using very flexible elements with the use of modern techniques and materials and allows to build in larger scales. The required materials should have a high ratio between strength and Young’s modulus to reach significant curvatures while keeping enough elastic reserve. The result is a lightweight structure, rapidly assembled and with low material consumption. The structural principle is called *active bending* and it is being studied by several research groups.

After the Multihalle, several smaller gridshells have been built. A detailed account of the realisations may be found in [38]. Most of them use timber [76], but more recently GFRP tubes have also been used [36, 37]. Of this last kind, the most outstanding example is the ephemeral cathedral of Creteil in Paris (Fig. 1c), designed by the firm TESS and the Navier Laboratory of the ENPC. Other examples –e.g. Faraday Pavilion [69], ICD/ITKE Research Pavilion (Fig. 1b), Ongreening Pavilion [44], the Asymptotic Pavilion at the central campus of the TUM [86]– are of ephemeral and/or sculptural nature.



(a) Mannheim Multihalle [43].



(b) ICD/ITKE Research Pavilion [66].



(c) Ephemeral cathedral of Creteil [38].

**Figure 1:** Some iconic gridshells built in the last years.

One of the inconveniences that hampered the development gridshells in the 1980s and 1990s was the difficulty to determine the target configuration of the structure, because the activation process, from the initial stress-free configuration to the desired configuration is highly non-linear. This problem has been intensively researched in the last ten years, and today, there are efficient software tools for simulating the activation process from the unstressed configuration.

In fact, there is an increasing interest in investigating the behaviour of very flexible structures subject to large deformations, both in the investigation of buckling as a method to shape structures and devices at different scales [78], as well as in the generation of mechanical and computational models [16]. Good examples of this are recent references by the Chair of Structural Analysis at the TU Munich that apply novel beam models, isogeometric analysis and CAD tools for bending-active problems [11, 95].

As can be seen in the literature, the form-finding problem of bending-active structures has been extensively studied. However, the number of investigations focused on their structural performance and efficiency in relation to their shape and member sizing is still limited [34, 64]. Apart from the already mentioned difficulty to form-find the structure, the need to use a sufficiently flexible but at the same time strong material for the rods has limited the application to structures made of timber and more recently of GFRP and also bamboo [87]. Additionally, this fact has tra-

ditionally restricted the applicability of bending-active structures to dome shapes, since for structures that need to bear heavier loads and limit deflections, such as footbridges, the design space may be very narrow, and this explains why there are very few bending-active examples.

Therefore, there are many questions still open for research in active bending: where are the limits of applicability for bending-active structures?, is it possible to build structures with larger loads like pedestrian bridges?, which are the main parameters in the assessment of the structural response of a bending-active system? Are bending-active structures advantageous over passive (standard) ones? Despite the responses are not evident, they reflect that there is still room to generate knowledge and improve applications in the field.

## 1.1 MOTIVATION

The origin of this thesis lies in the previous work carried out by Lázaro [55]. His dissertation examines the fundamentals of the geometrically exact rod model and its connection with the non-linear theory of elasticity. The geometrically exact rod model belongs to a well-established class of mechanical models specifically formulated to reproduce the behaviour of very flexible structures. These are derived from the so-called geometrically exact (or Reissner-Simo) beam theory, and they are able to handle arbitrarily large rotations of beam cross-sections by considering their mathematical properties as elements of a non-additive and non-commutative group [60]. Reissner-Simo models are not free from implementation difficulties, mainly caused by the exact treatment of rotations. However the conceptual simplicity of the underlying theory and the subsequent powerful numerical solutions evince their potential consideration as a basis for form-finding and analysis methods for bending-active structures. In this context, his work set the stage to advance in the development of a form-finding computational method to simulate the process of deformation of bending-active elements using this mechanical model.

After few months working in the field of computational methods, the author had the opportunity to join the research project: *Sistemas estructuras flexo-activos- Concepción, desarrollo y análisis de nuevos prototipos* (FLEXACT - grant BIA2105-69330-P), aimed to: (1) conceive new structural prototypes for lightweight structures based on active bending strategies; (2) analyse the feasibility of the proposed systems; (3) develop an efficient computational procedure for shape determination and analysis of flexo-active structures. This implied a partial modification of the thesis guidelines, reducing the weight of the computational-analytical part and redirecting the works to the field of practice and application. Nonetheless, this integrated approach allowed the author further exploration of other key aspects of the design process such as: (a) conceptual design by means of small-scale models; (b) design and fabrication of custom-made pieces for bending-active systems; (c) activation and assembling process. All these topics are reflected on a 5 m long prototype of an experimental lightweight footbridge, which has been designed, fabricated and tested in the frame of this PhD thesis.

Moreover, the reduced number of realisations has further limited the knowledge about the structural response of bending-active structures. This fact motivated the studies carried out in this dissertation on efficiency and structural performance for this structural type.

Finally, the well-established knowledge about optimisation methods based on genetic algorithms inspired the development of a design tool to obtain efficient structural configurations for bending-active arches using multi-objective optimisation strategies. This work was carried out in the Department of Architecture & Civil in Engineering at the University of Bath (UK), under the supervision of Dr. Shepherd, expert in parametric modelling and optimisation methods.

## 1.2 RESEARCH OBJECTIVES

This doctoral thesis aims to evaluate the applicability of the active bending principle to the design of lightweight structures, so that they are able to meet the limitations imposed by codes for pedestrian bridges and roofing applications. This goal is achieved by: (a) understanding their structural behaviour from the determination of the initial geometry of the system to the assessment of the structure against the design loads posed by codes; (b) evaluating the influence of the form-finding parameters involved in the equilibrium configuration and (c) providing comprehensive directions towards efficient solutions with maximum elegance in shape. For that purpose and given the knowledge gaps identified, the following objectives were established:

- To conceive a new structural prototype based on the active bending principle. The possibility of applying active bending as a resistant mechanism in structural types suitable for lightweight pedestrian bridges and roofing modules is explored. The definition of structural types is supported by the development of conceptual models and prototypes.
- To advance knowledge in computational modelling and behaviour of very flexible structures. This includes the implementation and specialisation of an alternative mechanical model –the so-called geometrically exact (or Reissner-Simo) beam theory– into the well-known dynamic relaxation (explicit) method. This mechanical model has been specifically designed to reproduce the behaviour of very flexible structures and has not been used so far in form-finding of bending-active structures.
- To assess the structural performance and efficiency of the bending-active configurations identified as promising applications for the design of lightweight structures. The assessment must include the structural response due to activation forces and loading models posed by codes.
- To develop a computational procedure based on genetic algorithms to determine the best structural configuration of the selected bending-active arrangement, considering the material and geometric restrictions, as well as the limitations posed by the Eurocode for footbridges.

## 1.3 DISSERTATION OUTLINE

This dissertation is composed of eight chapters and one appendix. It is organised as described in the following:

**CHAPTER ONE** gives the motivation and research objectives of this PhD thesis. The dissertation outline is also detailed;

**CHAPTER TWO** presents a review on the state of the art on active bending, with particular regard to the strategies of shape determination and preceding works on the structural performance and efficiency of bending-active structures. A brief review on previous works about the application of the active bending principle in the design of lightweight footbridges is also provided;

**CHAPTER THREE** provides the development of a novel form-finding method based on the geometrically exact rod model (or Reissner-Simo beam theory) for bending-active structures. It outlines a brief summary of the fundamentals of Reissner-Simo theory and the description of the numerical framework. The principles of the dynamic relaxation method are also reviewed. The chapter ends with a set of numerical examples showing the ability of the method to simulate the deformation process of bending-active elements. This chapter is an adaptation of the published peer-reviewed paper: Bessini, J.; Lázaro, C.; Monleón, S. (2017) "A form-finding method based on the geometrically exact rod model for bending-active structures". *Engineering Structures*. 152:549-558. doi: 10.1016/j.engstruct.2017.09.045;

**CHAPTER FOUR** presents the *bending-active braced (or tied) arch* as a proposal of bending-active applications, with emphasis on the analytical development of the solution. This chapter also describes an analytical method based on *elastica curves* to generate shapes for bending-active braced;

**CHAPTER FIVE** goes into the part of the work related to the analysis of structural performance and efficiency of bending-active tied arches. Numerical experiments are carried out to evaluate the structural response of a finite number of arches due to activation forces and the loading models posed by the Eurocode for footbridges. This chapter is an adaptation of the published peer-reviewed paper: Bessini, J.; Lázaro, C.; Casanova, J.; Monleón, S. (2019) "Efficiency-based design of bending-active tied arches". *Engineering Structures*. Vol. 200, 1 December 2019, 109681;

**CHAPTER SIX** presents a design tool to generate efficient configurations for braced bending-active arches using multi-objective optimisation strategies. Following the structural principles used in Chapter 5, this algorithm evaluates every potential configuration to determine the best structural solution. This chapter is an adaptation of the published peer-reviewed paper: Bessini, J.; Shepherd, P.; Monleón, S.; Lázaro, C.; (2020) "Design of bending-active tied arches by using a multi-objective optimisation method". *Structures*. Vol. 27, pp. 2319-2328. doi: 10.1016/j.istruc.2020.07.045;

**CHAPTER SEVEN** shows the design, fabrication and assembling of a footbridge prototype based on the active bending principle;

**CHAPTER EIGHT** presents the conclusions of the thesis and a proposal for future works;

**APPENDIX A** gathers the numerical results in the form of diagrams used in the design of the experimental bending-active footbridge presented in Chapter [7](#).

# 2

## STATE OF THE ART

” *Read Euler, read Euler, he is the master of us all.*

– **Pierre Simon Laplace**  
(Astronomer and mathematician)

### 2.1 THE ACTIVE BENDING PRINCIPLE

The term *active-bending* refers to a category of structures in which bending is used in the process of shape configuration, obtaining structural schemes from elastic members such as beams, plates or rods of great slenderness, which are initially straight and unstressed (Fig. 2). Because of the geometrical and mechanical properties of the bent (or active) members, bending-active structures are in general lightweight structures that achieve the desired stiffness due to the curved shape acquired by active elements and to the action of stabilising additional members [16, 18].

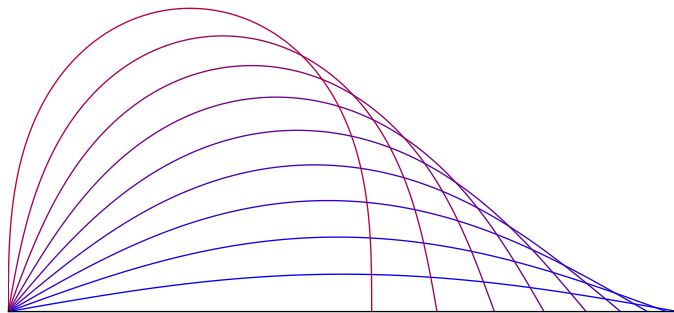


**Figure 2:** Activation process of an initially straight rod.

The first examples of bending-active structures are found in vernacular architecture, for instance in the construction of tent-like dwellings by tribal and nomadic societies (Fig. 3), where flexible slats are joined to form a lattice and bent to a dome-shaped roof [53, 56]. In spite of the ancient use of this technique, however, the number of contemporary realisations is limited.

A pioneering architectural realisation using the active bending principle is the Mannheim Multihalle (1974) designed by Frei Otto, in collaboration with Ian Liddell and Chris Williams (Fig. 4). With no computational power and simulation knowledge –computers were not powerful enough at that time– the geometry of the grid-shell was conceived as a free-form grid of bent timber members and fully form-found by using meaningful physical models [72].



(a) Oca shelter

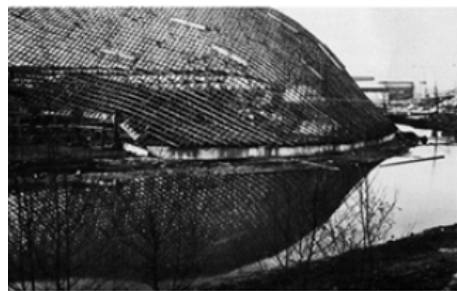


(b) Yurt tent

**Figure 3:** Examples of vernacular architecture built by means of elastically bent elements [97].



(a) Inside view



(b) Outside view

**Figure 4:** Mannheim Multihalle [43].

Otto's concept meant the birth of a specific structural type: the elastic gridshell; a surface structure in which a flat quadrangular mesh of initially straight members with rotation-free joints is lifted into the desired configuration and stabilised by means of additional structural members [18].

Since the construction of the Mannheim Multihalle, active bending has attracted considerable attention as a new paradigm to build lightweight structures. As a result, a number of dome-shape gridshells have been devised in the last years.<sup>1</sup> However, bending-active structures are not limited to gridshells and there are other examples such as pre-bent composite beams or experimental footbridges.

Baverel and Caron [12] proposed a concept of a footbridge using a beam pre-stressed by bending. The mechanism of a catapult was the basis of the structural concept to develop the project. Finally, they built a prototype to check the calculations and the technical feasibility of the system (Fig. 5a). Similarly, the *Laboratoire Navier of the École des Ponts ParisTech* –Baverel and Caron belong to this research group–, devised and built a model of prestressed composite footbridge (Fig. 5b). The bowstring bridge is obtained by bending straight glass fibre pipes and stabilising them with cables and zig-zag carbon fibre stays [26]. It can be concluded that there is a field to be explored in the applicability of the active-bending principle in the design of lightweight pedestrian bridges.

<sup>1</sup> A thorough review on realisations may be found in the PhD thesis of Du Peloux [38].



(a) Experimental footbridge using a beam prestressed by bending [12].



(b) Conceptual model of a prestressed composite footbridge [26].

**Figure 5:** Experimental prototypes for bending-active footbridges.

## 2.2 REQUIRED MATERIAL PROPERTIES

The PhD thesis of Douthe [34] included a thorough study of suitable materials for active bending based on Ashby’s methodology [6]. According to it, several performance indices are derived from the various criteria that need to be considered to assess the validity of a material. Among these indices, the ratio *strength to Young’s modulus*, as well the Young’s modulus itself play a key role, because materials with high values of both indices are strong and flexible enough to work in a curved configuration. Lienhard [64] has proposed the following ratio between the elastic limit and the modulus of elasticity for a material to be suitable for active bending:

$$\frac{\sigma_{el}}{E} \geq 2.5 \cdot 10^{-3} \quad (1)$$

The ratio is related to the curvature that a rod of a given material can achieve while remaining in the elastic range. Some metals (aluminium, titanium and high-strength steels), carbon fiber and glass fiber composites, as well as bamboo and some types of timber comply with Lienhard’s criterion. For this reason, most examples of active bending are made of glass fiber composites, bamboo or timber.

The requirement of high-slenderness for active members is opposed by the need of bearing external loads, since too slender members may be prone to local buckling and may lead to structures with low stiffness. In the design of gridshell-like structures, the most dominant actions are wind and snow, so the structural configuration is typically targeted to obtain dome shapes. However, in the case of structures that must support heavier loads, such as pedestrian footbridges, the designer must find a compromise between the strength and the shape of structural members. This key observation is analysed by the author in Chapter 5.

## 2.3 DETERMINATION OF THE CONFIGURATION<sup>2</sup>

Due to the non-linearity of the structural response of the active members, the simulation of the process of deformation of bending-active elements is one of the main difficulties during the conceptual phase. Moreover, it is often not possible to obtain beforehand the equilibrium description of the system; its shape has to be determined as a result of a tight interaction between form, forces, material properties and boundary conditions [16, 64].

As in the case of tensile structures, the design of bending-active structures requires an initial form-finding step to determine the initial geometry of the system. Comparing, for example, a gridshell with a cable net, there is additional complexity in the gridshell due to the fact that bending will also involve shear and possibly axial forces, and all these will be present in the interaction between members once the equilibrium configuration is reached. In addition to the pure form-finding problem, bending-active structures require tracking the full deformation path of the structural elements from an initial unstressed configuration in order to quantify the effect of the activation of bending on the structure. Once the target shape has been reached and stabilised, the structural behaviour is considerably influenced by the inherited stress state [18].

Nowadays, the availability of computational tools has made it possible the complete simulation of the process of deformation of active members, taking into account both the purely geometrical aspects and the mechanical problem. Among different strategies, formulations based on explicit methods as dynamic relaxation (DR) using Kirchhoff's theory as underlying mechanical model are the main trend today [3, 8, 30, 31, 35, 39, 62, 84, 88].

The first proposal to handle the form-finding problem of gridshells was introduced by Otto *et al.* in [72]; they studied the uniform mesh net with square cells, explained how to build meaningful physical models for hanging nets and proposed the so-called compass method: a geometric method to find Chebyshev meshes from a given curved shape. This method has been recently extended by other authors either developing computational tools [21, 40, 77] or adding new implementations. For instance, Lefevre [61] proposed an extension of the method that take into account the eccentricity between the rod layers. These techniques based on the use of physical models or simple geometric procedures provide admissible geometrical solutions (Fig. 6), but they are not able to simulate the induced pre-stress state. Hence, the development of computational form-finding methods with an integrated approach as explained before has been necessary to advance in this research field.

In addition to the pure form-finding problem, the need to solve the mechanical problem requires four basic features in order to obtain a reliable simulation [56].

1. The implementation of a mechanical model for flexible members capable of reproducing large displacements and rotations of cross-sections;
2. The ability of traversing critical points in the equilibrium path;

<sup>2</sup> This section is based on the articles: Bessini, J.; Lázaro, C.; Monleón, S. (2017) "A form-finding method based on the geometrically exact rod model for bending-active structures". *Engineering Structures*. 152:549-558. doi: 10.1016/j.engstruct.2017.09.045 and Lázaro, C.; Bessini, J.; Monleón, S. (2018) "Mechanical models in computational form finding of bending-active structures". *International Journal of Space Structures*. Volume 33 (2), pp. 86 – 97.

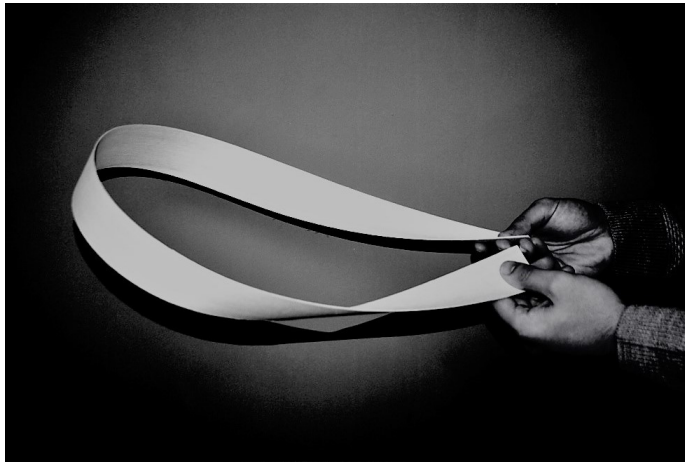


**Figure 6:** A physical model subject to bending and torsion effects. (Bending of developable surfaces has been studied in [93].)

3. The possibility to add and remove (in each design stage) auxiliary members to bring the system to the desired configuration;
4. Storing an inherited state corresponding to a previous stage.

In this context, a direct simulation –starting from an underformed configuration until the equilibrium configuration is reached– may be performed using suitable finite element software. Lienhard proposed a form-finding method based on finite element simulations where unstressed members reach their target shape by shortening non-linear virtual links [64]. This process has been recently improved by using isogeometric finite elements implemented into a CAD environment [11, 54]. Both, the direct simulation strategy and DR, must take into account the non-linear mechanics of large deformations of slender rods.

Generally, finite element models have been used for the load analysis and the simulation of the construction process of structures. The use of implicit resolution methods is also another potential alternative that is often used to find equilibrium solutions. However, in the so called 'design-oriented' problems, where the main unknown is the geometrical configuration and the determination of deformations and stresses is not the main goal, the use of explicit methods has been reported by some authors [7, 31] as more advantageous for those cases in which prescribed conditions are far from the equilibrium geometry.

Among different explicit methods, DR provides a straightforward way to obtain the static equilibrium of the structure from a given arbitrary and inaccurate initial configuration. The possibility of using fictitious values for the stiffness and mass, high damping ratios and different time steps contributes to the fast convergence of the numerical solution. This method does not require a *first shot* with an initial configuration that resembles the desired shape, but a good initial guess will be beneficial in terms of convergence [8].

DR has been specialised in different ways to find the shape of bending-active structures. The following key aspects are closely related and define the kind of specialisation:

- Type of discretisation;
- Underlying beam theory.

There are two types of discretisations in DR formulations reported in the literature: finite-difference-like discretisations and finite-element-like discretisations. In both cases, a key question is how force-configuration relationships between nodes are established. Those relationships are determined in each case by the underlying beam theory, defined by the kinematic assumptions of the model, the selected elastic energy terms and the constitutive relations [56]. Three groups of discretisations can be found in the literature in the context of form-finding of bending-active structures: (a) models based in discrete mechanics using 3 or 4 DoFs per node; (b) finite-difference-like discretisations, that shares the same principles as models based in discrete mechanics and also use 3 or 4 DoFs per node and (c) finite-element-like methods with 4 and 6 DoFs per node. The main distinction between the first two groups and the finite-element-like method is found in the way strain measures and internal forces are evaluated. The following sections go into these details in more detail.

### 2.3.1 Models based on discrete mechanics

They stem from developments in the field of computer animation: the underlying mathematics is based on discrete differential geometry (DDG) and they allow for very fast explicit simulation of the dynamics of highly flexible rods. For example, Bergou *et al.* [14] presented a discrete treatment based on the study of adapted framed curves and the topological concepts of parallel transport and holonomy. In contrast to typical simulation techniques relying on a kinematic description, they treat the centreline as dynamic and the material frame as quasi-static. Torsion is quantified by the angular deviation between material frames and natural Bishop frames. Thereby, solutions are formulated with a minimal number of degrees of freedom: the explicit description of the centreline of the rod (three DoFs) and the orientation of material frame using a scalar variable (one additional DoF). The authors claim that using this procedure, numerical instabilities are avoided in the dynamic relaxation algorithm. CAD tools based on this approach are commercially available [75], but unfortunately, as Cuvilliers *et al.* report in [29], their implementation details are not entirely available to the public. In most cases, the documentation is limited to explanations or simple examples provided by the developers. The most widely used CAD tools and libraries for the design of actively-bent structures are:

**KANGAROO 1** is probably the most representative tool for contemporary implementations of the DR method in the design of bending-active structures. It consists of a solver library and a set of Grasshopper (Rhinoceros3D) components [74]. To quote the developer, Daniel Piker: *Kangaroo 1 works by minimising total energy* [73]. In other words, Kangaroo moves iteratively the points (or particles) that form the system, by small steps, until the sum of the energies acting on all the points is as low as possible (equilibrium state). This approach can be seen as a modified form of DR. Because of the lack of accuracy in the explanation of the methodology, Kangaroo has often been classified as a *particle spring system*: an efficient approach to simulating the movement of soft bodies in computer animation, but with a too simple mechanical background to make it reliable for engineering applications.

**SHAPE-UP** is a library for static and dynamic geometry processing, using a unified optimisation framework based on shape constraints [20]. This solver uses projection operators and proximity functions to relocate a set of points by minimising the potential energy subject to physical and geometrical constraints. It has been developed by the Computer Graphics and Geometry Laboratory of EPFL.

**KANGAROO 2** has also been developed by Daniel Piker, with the aim of improving Kangaroo 1. However, it does not actually use the classical form of DR implemented in the previous version, but an approach based on projective constraint-based solving, as Shape-Up library does [29]. Indeed, the solving process used by Kangaroo 2 can be defined as a specialised version of the Shape-Up formulation, since it accelerates the system by means of virtual velocities attached to each point. It is one of the most successful tools among designers and architects.

**K2ENGINEERING** has been developed by Cecilie Brandt-Olsen [24]. It is a plugin that contains a set of customised Kangaroo 2 Grasshopper components with the scope of calibrating a number of goals concerning structural properties. Among others, this tool is particularly useful for the analysis of gridshells, typically characterised by large deformations when external loads are applied.

### 2.3.2 Models based on finite-difference discretisations

They share many features in common with the discrete mechanics models: discrete strain measures at nodes are deduced from difference schemes between nodal degrees of freedom, and internal forces or nodes are calculated by ad-hoc equilibrium relations or from energy derivations. Several approaches for this method have been suggested over the years, being reduced models with only three translational DoFs the most used.

In chronological order, Adriaenssens and Barnes [3], presented a method based on the Bernoulli-Euler theory with the extensibility assumption. They propose to calculate axial strains from nodal coordinate differences and the magnitude of bending moments  $M_j$  through estimates of curvatures  $\kappa_j$  obtained from the positions of groups of three consecutive nodes ( $i, j, k$ ) and the constitutive equation  $M_j = EI\kappa_j$  (see Eq. 2). Bending moments  $M_j$  are transformed into equivalent forces ( $S_{ij}, S_{jk}$ ), acting on the actual geometry of the beam (see Fig. 7). In this way, only 3 DoFs per node are needed. This model is valid for initially straight beams with square or circular shaped cross-sections [2].

$$\kappa_j = \frac{2 \sin \alpha_j}{d_{ik}} \quad (2)$$

Douthe *et al.* [35], focusing on the previous work by Adriaenssens and Barnes, proposed a similar methodology, in this case it is suitable for modelling initially straight beams with axisymmetric cross-section for the design of gridshells.

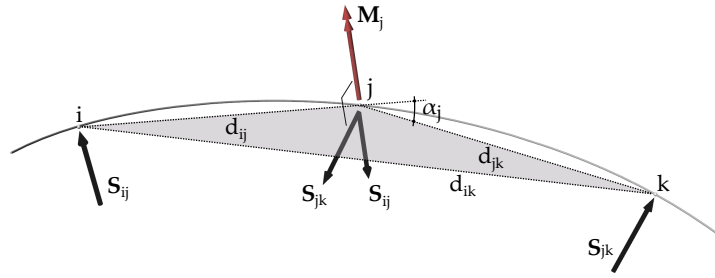


**Figure 7:** Discretisation in Adriaenssens and Barnes [3].

The problem of torsion and bending for dynamic relaxation modelling of spatial curved beams with non-uniform cross-sections was approached by Barnes *et al.* [8] few years later, extending Douthe's work; their assumption accounts for both torsion and transverse (out of plane) bending effects. As in the previous reference, the out-of-plane shear forces are calculated using the constitutive equation for torsion  $M_{jkl} = GJ\kappa_{jkl}$ . The discrete measure of the torsional strain  $\kappa_{jkl}$  is obtained as follows:

$$\kappa_{jkl} = \frac{\phi - \phi_0}{d_{jkl}} \quad (3)$$

where  $\phi_0$  is the angle made up of planes  $ijk$  and  $jkl$  at the start of the process (Fig. 8). This model is valid in cases where cross-sections are isotropic.

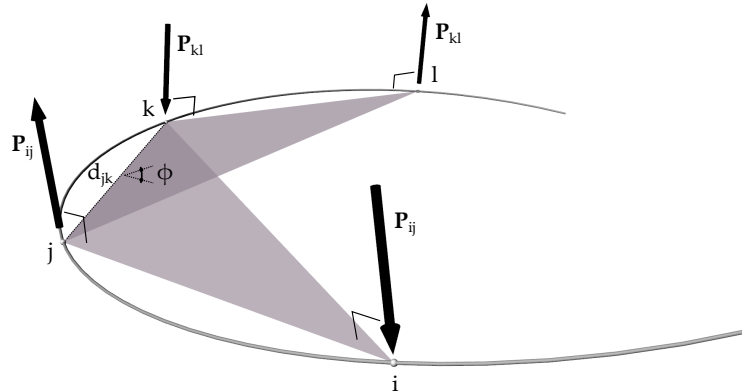


**Figure 8:** Discretisation in Barnes *et al.* [8].

Du Peloux *et al.* [39] and Lefevre *et al.* [62] have recently presented alternative approaches to model elastic rods with 4-DoFs: three DoFs for nodal positions and one additional DoF  $-\phi-$  to keep track of torsion (see Fig. 9). As mentioned before, these formulations are close to recent developments in the field of computer animation [14, 15]. The use of Bishop frames [19] allows to deal with general cases of structures with anisotropic cross-sections and torsional stiffness effects. Similarly, D'Amico *et al.* [31] proposed an approach to 3D curved rods as Du Peloux *et al.* It computes the angular difference between material frames and Bishop frames in case that torsional constraints are fixed at rod ends. Bishop frames at nodes are found by using Catmull-Rom interpolation and parallel transport.

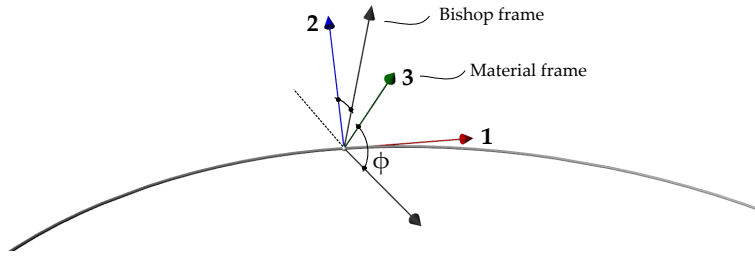


**Figure 9:** Discretisation in Du Peloux *et al.* [39].

In all these cases, discretisations were developed to formulate DR algorithms for form-finding. But again, the connection with FEM software for the subsequent analysis and checking of the structure is not direct. Table 1 summarises the main features of finite difference-like parametrisations presented in this section.

| Reference                      | No. of DoFs | Beam theory             | Stiffness parameters                      |
|--------------------------------|-------------|-------------------------|---|
| Adriaenssens <i>et al.</i> [3] | 3           | Extensible B-E          | EA, EI                                    |
| Barnes <i>et al.</i> [8]       | 3           | Modified extensible K-L | EA, EI, GJ                                |
| Du Peloux <i>et al.</i> [39]   | 4           | Inextensible K-L        | GJ, EI <sub>2</sub> , EI <sub>3</sub>     |
| D'Amico <i>et al.</i> [31]     | 3           | Extensible K-L          | EA, GJ, EI <sub>2</sub> , EI <sub>3</sub> |

**Table 1:** Comparison between references using finite-difference-like discretisations.

### 2.3.3 Models based on finite element discretisations

Three categories may be identified here:

**CO-ROTATIONAL MODELS** were introduced in the 1970s by Wempner and Belytschko [13] and have been widely used as basis for dynamic relaxation algorithms for shape finding. This technique splits the rod into two-node elements and the configuration is defined by nodal positions and nodal frames at a given instant. Thereby, the mechanical problem is divided into two sub-problems [56]:

1. Modelling the mechanical response of finite elements in terms of local displacements and rotations. This requires to keep track of element frames to assess angular differences with nodal frames (Fig. 10). In order to avoid the implementation of full element frames, the use of simplified co-rotational setups is a common procedure in the references presented in this section. Figure 11 shows this strategy, that consists in computing the vector  $\mathbf{e}_1$  as the normalised difference of updated nodal positions.
2. Tracking the changes in nodal positions and nodal frames with no limitation in their magnitude. This means updating large rotations of nodal and element frames between iterations. The reader is referred to the work of Argyris [4] and Crisfield [27] for a detailed treatment of large rotations in this sort of problems.

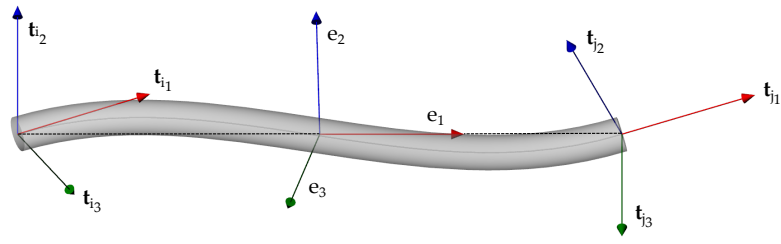


Figure 10: Co-rotational setup.

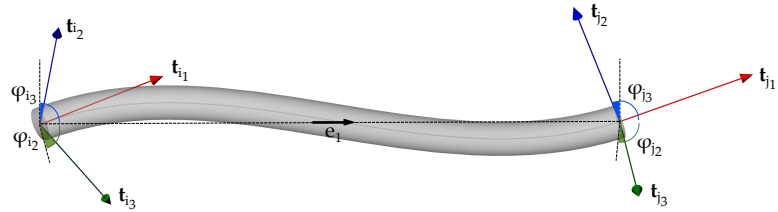


Figure 11: Simplified co-rotational setup.

The first approach to handle the problem of slender beams in large displacements using DR was introduced by Wakefield in 1980 [96]; he implemented a formulation taking into account 6 DoFs. As reported by Adriaenssens [1], Williams developed a more precise resolution scheme, assuming local reference frames at nodes and cubic shape functions to simulate the stiffness of the rod. Few years later and based on Williams's work, D'Amico *et al.* [30, 32] built a numerical framework aimed to the design of gridshells. Li and Knippers [63], as well as Senatore and Piker [88] used a co-rotational approach to compute the resultant field of displacements and the effect of large deformations in the beam elements. The use of 6 DoFs per node has the advantage of providing a complete description of the mechanical response. However, Adriaenssens and Barnes mention in reference [3] that the coupling between translational and rotational DoFs can cause conditioning problems in explicit methods. Latest advances in this field are related to the implementation of optimisation methods into the DR formulations. For example, Sakai *et al.* [85] and Rombouts *et al.* [81] have developed shape optimisation approaches for the design of gridshells using co-rotational beam elements and DR.

**GEOMETRICALLY EXACT MODELS** have been specifically designed to reproduce the behaviour of very flexible structures. The formulation is termed *geometrically exact* in the literature, because of the mathematically exact handling of rotations. Reissner [79] and Simo [89] developed a non-linear theory for the deformation of flexible rods that can be considered as a special case of Cosserat's theory, in which the director vectors attached to material fibres in a cross-section are constrained to remain inextensible and orthogonal, but not necessarily normal to the deformed centreline tangents. This theory can be also interpreted as a non-linear version of Timoshenko's theory for shear deformable beams and offers the conceptual simplicity of the kinematic assumption together with the power of a direct theory for solving non-linear problems. The assumptions of the geometrically exact model can be summarised as follows: cross-sections remain plane without changes of shape or size, although they may experience finite rotations as a rigid-body; warping effects

are not modelled; the centreline can undergo extension, and shear deformations are allowed. Simo in 1991 [90], extended his previous work incorporating shear and torsion-warping deformation into the geometrically exact rod model. Furthermore, different authors (Cardona and Geradin [25]; Ibrahimbegovic [46]; Sonnevile *et al.* [92]) have proposed later versions of the geometrically exact rod model over the years, but without adding significant changes in the approach. The specialisation of the geometrically exact rod model to the DR procedure has been developed by the author and his PhD supervisors in [16] and constitutes a substantial part of this dissertation (see Chapter 3).

**NON-LINEAR KIRCHHOFF ROD MODELS** have been recently developed by Armero *et al.* [5] and Meier *et al.* [68]. It is interesting to note that despite Kirchhoff's theory for rods dates back to the 19<sup>th</sup> c., the formulation of shear-indeformable, non-linear finite elements with arbitrarily large rotations has not achieved success until recent years. Especially interesting are isogeometric (IGA) implementations (Bauer [10]), because they are capable of simulating the activation process of a bending-active structure in a CAD environment, even in combination with membranes, and doing the subsequent structural analysis [94].

## 2.4 PREVIOUS WORKS ON STRUCTURAL PERFORMANCE OF BENDING-ACTIVE STRUCTURES<sup>3</sup>

The number of investigations focused on the assessment of the structural performance and efficiency of bending-active structures is limited. In order to extend the realm of applicability of this structural principle, further research is needed in relation to material properties, member sizing and geometry.

Lienhard in [64] studied the efficiency of several canonical cases of bending-active structures subject to simple loading patterns over a limited number of cases. A differentiation is drawn between (a) pure bending systems, (b) bending-compression systems, (c) bending-tension systems and (d) bending-torsion systems. A first test considers elastica-shaped arches with several rise-to-span ratios subject to a vertical point load at midspan, and concludes that: *once the beam forms the post-buckling elastica curve, there is no significant change in normal force, leading to constant geometric stiffness* [64]. As a following step, Lienhard carried out numerical dynamic tests comparing eigenfrequencies of actively bent arches, and *passive* arches with the same geometry to evaluate the effect of the geometric stiffness regardless of the applied load pattern. Pure bending systems give the same frequencies in both cases, active and passive arches. Therefore, the stiffness of this kind of systems is independent of the bending activation process. Bending-compression systems, as elastica arches, provide lower values of stiffness than the passive case, due to compressive axial forces. In contrast, bending-tension systems, as bow-string type structures, show higher values of stiffness comparing again with their passive counterparts.

In the field of materials, Douthe considered in [34] strength and stiffness criteria to assess the applicability of different materials for active grid-shell members. In 2010, Douthe *et al.* [37] showed that composite materials in glass fibre reinforced

<sup>3</sup> This section is based on the article: Bessini, J.; Lázaro, C.; Casanova, J.; Monleón, S. (2019) "Efficiency-based design of bending-active tied arches". *Engineering Structures*. Vol. 200, 1 December 2019, 109681.

polymers are good options to build elastic gridshells. Few years later, Kotelnikova-Weiler *et al.* [51] extended their previous work to provide some directions for the choice of materials for actively-bent elements, with emphasis on the long-term behaviour of pultruded GFRP elements under the effect of bending and torsion stresses.

Other aspects such as the durability (creep, relaxation or fatigue) or the dynamic behaviour cannot be neglected in the design of bending-active structures, especially in those made of composite materials [37]. In GFRP footbridges it has been observed that the low weight and high flexibility of the structure have a large influence in the dynamic response of the structure, since natural frequencies are expected to be low and may be activated by pedestrians walking [26].

In the framework of the research project FLEXACT, Lázaro *et al.* [58] analysed the response of circular and elastica-shaped active arches subject to a point load, and quantified the relation between geometric stiffness, tangent stiffness and the angle at arch ends for different values of the slenderness. Results show that in slender arches, starting from a straight geometry and increasing the angle at both ends, the stiffness increases rapidly until it reaches a maximum (Fig. 12). Passive and bending-active arches show similar behaviour. In the case of elastica arches, the activation produces a reduction in maximum stiffness ranging from 6% to 9.5%, depending of the slenderness of the rod and comparing it with the stiffness of a circular arch with the same geometry. In the case of circular arches, activation does not influence the stiffness because it does not involve compression forces.

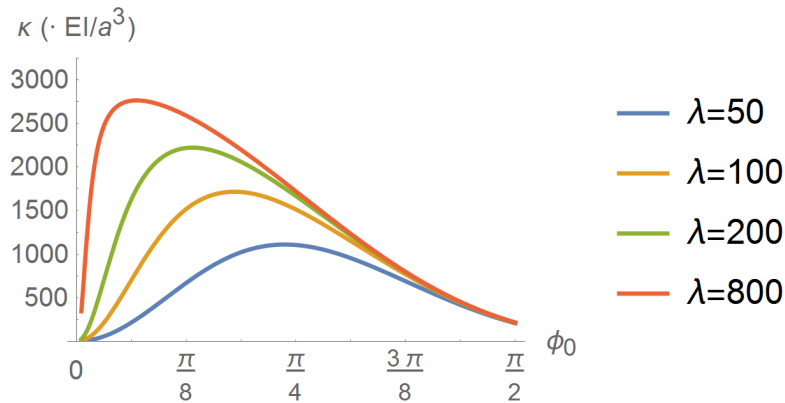


**Figure 12:** Total stiffness of elastica arches with angle at the inflexion equal to  $\phi_0$  for different values of rod slenderness  $\lambda$  [58].

More recently, the research group presented a preliminary study of the relationship between structural shape, activation forces and activation stress levels for bending-active structures considering different structural configurations and loading conditions [57]. This important part in the design of bending-active structures is deeply explored in this PhD thesis.

# 3

## A FORM-FINDING METHOD BASED ON THE GEOMETRICALLY EXACT ROD MODEL FOR BENDING-ACTIVE STRUCTURES

” *One should not calculate a structure he cannot draw. Formulae should not be used if their physical meaning is not understood. A structure should not be designed by computer if we do not know how to calculate it by hand.*

— **Javier Rui-Wamba**  
(Civil engineer)

This chapter is an adaptation of the published peer-reviewed paper: Bessini, J.; Lázaro, C.; Monleón, S. (2017) "A form-finding method based on the geometrically exact rod model for bending-active structures". *Engineering Structures*. 152:549-558. doi: 10.1016/j.engstruct.2017.09.045.

### 3.1 INTRODUCTION

In the field of bending-active structures, the complexity of finding beforehand the equilibrium configuration and the non-linearity of the structural response are main issues during the conceptual phase. As explained in the previous chapter, the use of tools based on classical form-finding procedures as DR is the main trend today; different mechanical models with 3, 4 or 6 degrees of freedom have been implemented for modelling the bending effect [3, 8, 16, 30, 31, 35, 39, 62, 84, 88]. As previously seen, there is a well-established class of mechanical models which has been specifically designed to reproduce the behaviour of very flexible structures and however, they have not been explored so far in the framework of the form-finding of bending-active structures. These are derived from the so-called geometrically exact (or Reissner-Simo) beam theory, and they are able to treat arbitrarily large rotations and displacements. The objective of this chapter is to develop a form-finding tool based on Reissner-Simo's theory and the DR method. The reader can refer to section 2.3.3 of the Chapter 2 for a brief review about the model.

One of the keys of this method is the choice of the form-finding parameters: the target centreline length and the kinematic constraints at beam ends will determine the shape of the final structure in the 'design-oriented' process. In addition, the proposed form-finding method is based on the following considerations:

- Explicit solution search using DR.
- The geometrically exact rod model as underlying mechanical model.
- Translations and rotations are updated by means of 6 DoFs per node.

- Anisotropic cross-sections can be modelled. Thin-walled open cross-sections are precluded, since warping and local buckling phenomena are not considered in the formulation.
- Initial specifications of the geometry do not need to be close to the equilibrium solution.
- Boundary conditions are defined by nodal positions and cross-section orientations (optionally) of the beam ends. Additional numerical constraints or nodes are unnecessary.

### 3.1.1 Outline of the chapter

The outline of the chapter is as follows: In sections 3.2 and 3.3, the geometrically exact model formulation and the principles of the DR method are reviewed. The fundamentals and description of the numerical framework are detailed in sections 3.4 and 3.5. Numerical examples showing the ability of the form-finding method to reproduce the behaviour of active members are included in section 3.6.

## 3.2 THE GEOMETRICALLY EXACT ROD MODEL

The geometrically exact rod model was formulated by Simo [89] starting from the work of Reissner [79]. It allows to reproduce arbitrarily large displacements and rotations of rods using an exact kinematic description of finite rotations of cross-sections. In this section, a brief summary of the fundamentals of Reissner-Simo theory is given. The notation used is based, although not the same, as the one introduced by Simo. It follows more closely the one used by Ritto-Corrêa and Camotim in their summarising reference [80]. The full development of this theory can be found in the PhD thesis of Lázaro [55].

### 3.2.1 Basic kinematics

A fixed reference system  $\{x,y,z\}$  in space is chosen. Three configurations are considered (Fig. 13): a) The reference (ideal) configuration, in which the rod is straight, the line of centroids is aligned with the  $x$ -axis, and cross-sections are oriented in such way that principal axes of inertia are parallel to  $y$  and  $z$ -axes. Unit vectors  $\mathbf{A}_2$  and  $\mathbf{A}_3$  are attached to the principal axes and  $\mathbf{A}_1$  is normal to the cross-sections; they form an orthogonal system.  $S$  is the (arc-)length coordinate along the centreline in the reference configuration.  $X^2$  and  $X^3$  are coordinates in each cross-section. b) The initial (undeformed) configuration: the rod centreline can be a spatial curve. Cross-sections are normal to the curve and are defined by  $\mathbf{a}_{01}$ ,  $\mathbf{a}_{02}$ ,  $\mathbf{a}_{03}$ , the unit directors in the undeformed configuration, being  $\mathbf{a}_{01}$  tangent to the curve. These directors are the result of a rigid-body rotation of  $\mathbf{A}_1$ ,  $\mathbf{A}_2$ ,  $\mathbf{A}_3$ . c) The actual (deformed) configuration at an instant  $t$ : during the deformation every cross-section is assumed to undergo a rigid-body motion. Directors  $\mathbf{a}_1$ ,  $\mathbf{a}_2$ ,  $\mathbf{a}_3$  remain unitary and orthogonal, but  $\mathbf{a}_1$  is not necessarily tangent to the centreline. If the components with respect to the fixed space frame of  $\mathbf{a}_1$ ,  $\mathbf{a}_2$  and  $\mathbf{a}_3$  are written in columns, they form an orthogonal matrix  $\mathbf{\Lambda}$  of determinant 1, which is only a function of  $S$  and the time  $t$ . The position vector of a material point can be expressed in terms of its

relative location into the section  $\mathbf{r}^*$ , the position of the centroid of the section  $\mathbf{x}$  and the rotation of the cross-section  $\mathbf{\Lambda}$  as follows:

$$\mathbf{x}^*(S, X^2, X^3, t) = \mathbf{x}(S, t) + \mathbf{r}^*(S, X^2, X^3, t) \quad (4a)$$

$$\mathbf{r}^*(S, X^2, X^3, t) = \mathbf{\Lambda}(S, t) \mathbf{R}^*(X^2, X^3) \quad (4b)$$

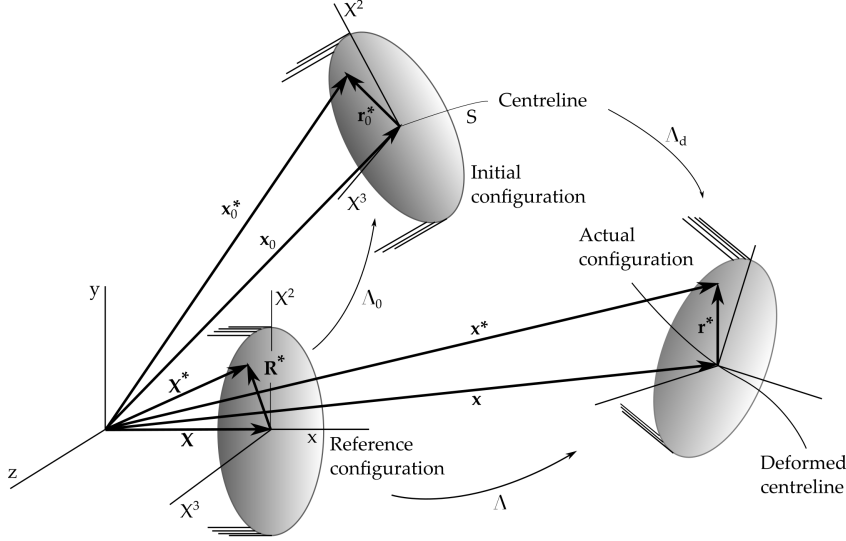


Figure 13: Kinematics of Reissner-Simo's model [60].

Section points rotate from an ideal reference configuration (described by  $\mathbf{R}^*$ ) to the deformed (actual) configuration.  $\mathbf{x}(S, t)$  and  $\mathbf{\Lambda}(S, t)$  are the configuration functions of the geometrically exact model. The 1D deformation gradient can be written as [60]:

$$\partial \mathbf{x}^* / \partial S = \mathbf{x}' + \mathbf{\Lambda}' \mathbf{\Lambda}^T \mathbf{r}^* = \boldsymbol{\gamma} + \hat{\boldsymbol{\kappa}} \mathbf{r}^* \quad (5)$$

The hat over a variable denotes a skew-symmetric matrix. The same variable with no hat refers to its axial vector. Capital letters refer to material variables (variables expressed in the system of reference attached to the cross-sections). Lowercase letters refer to spatial variables (variables expressed in the fixed reference system  $\{x, y, z\}$ ). Transformations between spatial and material forms is performed through the action of  $\mathbf{\Lambda}$ . Given a vector  $\mathbf{v}$ , the operation  $\mathbf{v} = \mathbf{\Lambda} \mathbf{V}$  is called push-forward, and the operation  $\mathbf{V} = \mathbf{\Lambda}^T \mathbf{v}$  is called pull-back.

$\boldsymbol{\gamma}$  and  $\boldsymbol{\kappa}$  are the generalised strain measures expressed in spatial form. Their counterparts in material form,  $\boldsymbol{\Gamma}$  and  $\mathbf{K}$ , allow to define the physical strain measures  $\boldsymbol{\Gamma}_d$  and  $\mathbf{K}_d$  as:

$$\boldsymbol{\Gamma}_d = \boldsymbol{\Gamma} - \boldsymbol{\Gamma}_0 \quad (6a)$$

$$\mathbf{K}_d = \mathbf{K} - \mathbf{K}_0 \quad (6b)$$

$\hat{\mathbf{K}}_0 = \mathbf{\Lambda}_0^T \mathbf{\Lambda}'_0$  represents the rotation and twist rate of the initial centreline, and  $\boldsymbol{\Gamma}_0$  is the material form of the tangent vector to the initial centreline.  $\boldsymbol{\Gamma}_0$  is precisely the vector  $\mathbf{A}_1$  of the section frame in the reference configuration, with components  $\{1, 0, 0\}$ . Therefore:

$$\boldsymbol{\Gamma}_d = \boldsymbol{\Gamma} - \mathbf{A}_1 = \{\Gamma_1 - 1, \Gamma_2, \Gamma_3\} \quad (7)$$

The first component of  $\Gamma_d$  is a measure of the *elongation* of the centreline and the other two components are the distortions along the axes of the cross-section. It is worth remarking that  $\mathbf{K}_0 = \mathbf{0}$  when the rod is initially straight, something usual in the initial definition of geometries in form-finding problems.

### 3.2.2 Variation of the generalised strain measures

The variation of the configuration can be computed as:

$$\delta \mathbf{x}^* = \delta \mathbf{x} + \delta \mathbf{\Lambda} \mathbf{\Lambda}^T \mathbf{r}^* = \delta \mathbf{x} + \delta \hat{\boldsymbol{\omega}} \mathbf{r}^* \quad (8)$$

$\delta \boldsymbol{\omega}$ , the axial vector of  $\delta \hat{\boldsymbol{\omega}}$ , is referred to as the incremental rotation or *spin*. Because  $\boldsymbol{\gamma}$  and  $\boldsymbol{\kappa}$  are mathematical objects related to the deformed cross-section, their variation requires a special definition: given a vector  $\mathbf{v}$ , the corotational variation  $\nabla \delta \mathbf{v}$  is defined as the variation from the point of view of an observer located at the section reference system as:

$$\nabla \delta \mathbf{v} = \mathbf{\Lambda} \delta (\mathbf{\Lambda}^T \mathbf{v}) = \delta \mathbf{v} - \delta \boldsymbol{\omega} \times \mathbf{v} \quad (9)$$

The result is composed of two summands: the first is the variation of  $\mathbf{v}$  from the point of view of an observer located in the fixed reference system. The second is the correction due to the movement of the actual configuration as the observer moves along the centreline of the deformed curve. Further details can be found in the comprehensive work by Lázaro [55]. The co-rotational variations of the generalised deformations are:

$$\nabla \delta \boldsymbol{\gamma} = \delta \mathbf{x}' + \boldsymbol{\gamma} \times \delta \boldsymbol{\omega} \quad \text{and} \quad \nabla \delta \boldsymbol{\kappa} = (\delta \boldsymbol{\omega})' \quad (10)$$

### 3.2.3 Equations of static equilibrium

First, the expression of the internal virtual work is manipulated. Introducing the Eqs. (10) in the term corresponding to the internal forces  $\mathbf{n}$  and moments  $\mathbf{m}$  in the spatial description, the expression reads:

$$\delta W_{\text{int}} = \int_{S_i}^{S_j} \left( \mathbf{n} \cdot \nabla \delta \boldsymbol{\gamma} + \mathbf{m} \cdot \nabla \delta \boldsymbol{\kappa} \right) dS \quad (11)$$

and integrating by parts:

$$\begin{aligned} \int_{S_i}^{S_j} (-\mathbf{n}) \cdot \delta \mathbf{x} dS + \int_{S_i}^{S_j} (-\mathbf{m}' + \mathbf{n} \times \boldsymbol{\gamma}) \cdot \delta \boldsymbol{\omega} dS \\ + [\mathbf{n} \cdot \delta \mathbf{x}]_{S_i}^{S_j} + [\mathbf{m} \cdot \delta \boldsymbol{\omega}]_{S_i}^{S_j} \end{aligned} \quad (12)$$

The virtual work of the external forces  $\mathbf{q}_n$  and  $\mathbf{q}_m$  is:

$$\delta W_{\text{ext}} = \int_{S_i}^{S_j} (\mathbf{q}_n \cdot \delta \mathbf{x} + \mathbf{q}_m \cdot \delta \boldsymbol{\omega}) dS \quad (13)$$

Static equilibrium is equivalent to the equality of internal and external virtual work  $\delta W_{\text{int}} = \delta W_{\text{ext}}$  for any compatible set of virtual movements of the system. Therefore, the spatial form of the equations of static equilibrium are:

$$\mathbf{n}' + \mathbf{q}_n = \mathbf{0} \quad (14a)$$

$$\mathbf{m}' + \boldsymbol{\gamma} \times \mathbf{n} + \mathbf{q}_m = \mathbf{0} \quad (14b)$$

with the boundary conditions at the start:

$$[\mathbf{n}(S_i) + \mathbf{n}_i] \cdot \delta \mathbf{x}(S_i) = 0 \quad (15a)$$

$$[\mathbf{m}(S_i) + \mathbf{m}_i] \cdot \delta \boldsymbol{\omega}(S_i) = 0 \quad (15b)$$

and the boundary conditions at the end:

$$[\mathbf{n}(S_j) + \mathbf{n}_j] \cdot \delta \mathbf{x}(S_j) = 0 \quad (16a)$$

$$[\mathbf{m}(S_j) + \mathbf{m}_j] \cdot \delta \boldsymbol{\omega}(S_j) = 0 \quad (16b)$$

On the other hand, the internal virtual work in the spatial configuration can be expressed in matrix form as:

$$\begin{aligned} \delta W_{\text{int}} &= \int_{S_i}^{S_j} \nabla \delta \boldsymbol{\epsilon} \cdot \mathbf{f} \, dS = \int_{S_i}^{S_j} \left( \nabla \delta \boldsymbol{\gamma} \cdot \mathbf{n} + \nabla \delta \boldsymbol{\kappa} \cdot \mathbf{m} \right) \, dS \\ &= \int_{S_i}^{S_j} \{ \delta \mathbf{x}^T \quad \delta \boldsymbol{\omega}^T \quad \delta \mathbf{x}'^T \quad \delta \boldsymbol{\omega}'^T \} \begin{bmatrix} \mathbf{0} & \mathbf{0} \\ -\hat{\boldsymbol{\gamma}} & \mathbf{0} \\ \mathbf{1} & \mathbf{0} \\ \mathbf{0} & \mathbf{1} \end{bmatrix} \begin{Bmatrix} \mathbf{n} \\ \mathbf{m} \end{Bmatrix} \, dS \end{aligned} \quad (17)$$

### 3.2.4 Equations of dynamic equilibrium

To account for dynamic effects, Simo [89] introduced the equations of motion expressed in terms of forces and moments:

$$\mathbf{n}' + \mathbf{q}_n = \mathfrak{m} \mathbf{a} \quad (18a)$$

$$\mathbf{m}' + \boldsymbol{\gamma} \times \mathbf{n} + \mathbf{q}_m = \mathfrak{i} \dot{\boldsymbol{\omega}} + \boldsymbol{\omega} \times \mathfrak{i} \boldsymbol{\omega} \quad (18b)$$

where  $\mathfrak{m}$  is the mass matrix,  $\mathfrak{i}$  the inertia tensor,  $\mathbf{a}$  is the translational acceleration vector,  $\boldsymbol{\omega}$  is the angular velocity vector and  $\dot{\boldsymbol{\omega}}$  the angular acceleration vector, all of them expressed in spatial form.

### 3.2.5 Constitutive equations

The material form of the constitutive equations relates the static variables  $\mathbf{N}$  and  $\mathbf{M}$  with the physical deformations of the model  $\boldsymbol{\Gamma}_d$  and  $\mathbf{K}_d$  as follows:

$$\begin{Bmatrix} \mathbf{N} \\ \mathbf{M} \end{Bmatrix} = \begin{bmatrix} \mathbf{C}_\Gamma & \mathbf{0} \\ \mathbf{0} & \mathbf{C}_K \end{bmatrix} \begin{Bmatrix} \boldsymbol{\Gamma}_d \\ \mathbf{K}_d \end{Bmatrix} \quad (19)$$

Assuming that the centroid and the centre of torsion of the cross-section coincide,  $\mathbf{C}_\Gamma$  and  $\mathbf{C}_K$  are:

$$\mathbf{C}_\Gamma = \begin{bmatrix} EA & 0 & 0 \\ 0 & GA_{Q2} & 0 \\ 0 & 0 & GA_{Q3} \end{bmatrix} \quad (20a)$$

$$\mathbf{C}_K = \begin{bmatrix} GJ & 0 & 0 \\ 0 & EI_2 & 0 \\ 0 & 0 & EI_3 \end{bmatrix} \quad (20b)$$

The spatial description of the internal forces is obtained pushing-forward the corresponding material variables:

$$\begin{Bmatrix} \mathbf{n} \\ \mathbf{m} \end{Bmatrix} = \begin{bmatrix} \boldsymbol{\Lambda} & \mathbf{0} \\ \mathbf{0} & \boldsymbol{\Lambda} \end{bmatrix} \begin{Bmatrix} \mathbf{N} \\ \mathbf{M} \end{Bmatrix} \quad (21)$$

### 3.3 THE DYNAMIC RELAXATION METHOD

The dynamic relaxation method was introduced in the 60s by Day [33] and Otter [71]. It was developed to determine the equilibrium configuration of a system considering it as a fictitious dynamic system; the initial specification of the geometry can be far from the equilibrium solution. The equilibrium configuration is obtained tracing step-by-step the motion of each node of the structure for small time increments  $\Delta t$  using Newton's second law, until the equilibrium state is reached [7]. In order to achieve rapid convergence, several approaches can be considered, for example the use of viscous damping. When the structure has large motions, additional damping strategies (as kinetic damping) must be implemented. Being an explicit method, DR does not require assembling any stiffness matrix and it is quick to build the system, providing powerful and reliable results for non-linear structural problems.

### 3.4 FUNDAMENTALS OF THE METHOD

This section shows the fundamentals of the implementation of the geometrical exact rod model into the DR method.

An elastic rod is modelled by a discrete set of nodes  $\mathbf{x}_i$ , which are referred to the fixed Cartesian coordinate system (global reference system  $\{x, y, z\}$ ) These nodes are linked in pairs, being at the same time, the ends of beam elements that constitute the whole rod.

A local reference frame is associated to each node. The unit vectors of the frame define the orientation of corresponding material axes of the cross-section. At the start of the process, the orientation of the nodal frames at free nodes can be arbitrarily chosen.

In addition to kinematic constraints, the parameter  $L_0$ , the target length of the curve in the equilibrium state, must be prescribed. The sum of distances between nodes is near the prescribed target length of the elements when the state of equilibrium is reached.

#### 3.4.1 Application of D'Alembert's principle

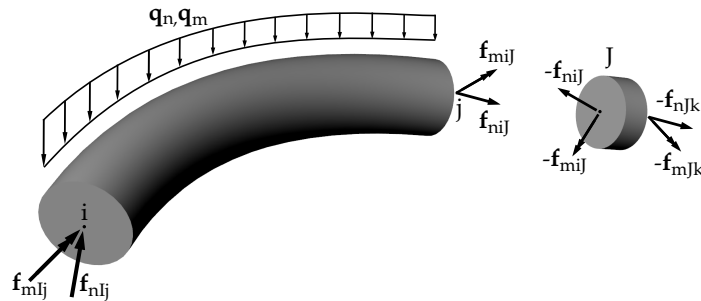


**Figure 14:** Scheme of forces and moments acting on the element  $ij$  and the node  $j$

The fundamental of the method is based on D'Alembert's principle. Dynamic equilibrium is expressed using Eqs. (18a) and (18b), where out of balance forces  $\tilde{f}_{n_j}$  and out of balance moments  $\tilde{f}_{m_j}$  at node  $j$  are equal to the derivative of the linear

momentum  $\dot{\mathbf{p}}_J$  and the derivative of the angular momentum  $\dot{\mathbf{h}}_J$  acting on this node:

$$\tilde{\mathbf{f}}_{n_j} = \dot{\mathbf{p}}_J = m_J \mathbf{a}_J \quad (22a)$$

$$\tilde{\mathbf{f}}_{m_j} = \dot{\mathbf{h}}_J = \dot{\mathbf{i}}_J \dot{\boldsymbol{\omega}}_J + \boldsymbol{\omega}_J \times \dot{\mathbf{i}}_J \boldsymbol{\omega}_J \quad (22b)$$

On the other hand, the out of balance forces/moments are the resultant of the external loads and the internal forces/moments caused by elements attached to node  $J$ :

$$\tilde{\mathbf{f}}_{n_J} = -\mathbf{f}_{n_iJ} - \mathbf{f}_{n_jk} \quad (23a)$$

$$\tilde{\mathbf{f}}_{m_J} = -\mathbf{f}_{m_iJ} - \mathbf{f}_{m_jk} \quad (23b)$$

Evaluating iteratively the equations of the dynamic equilibrium at nodes, the update of the geometry is provided by the motion associated to each set of out of balance forces/moments. The state of equilibrium is reached when the structure comes to rest; the sum of all forces/moments is zero at each node.

Internal forces/moments at element ends are computed according to D'Alembert's principle: using the notation of Fig. 14, the following equation holds for any consistent set of virtual displacements  $\delta\mathbf{x}$  and spins  $\delta\boldsymbol{\omega}$ :

$$\begin{aligned} & \int_{S_i}^{S_j} (-\mathbf{n} - \mathbf{q}_n + m \mathbf{a}) \cdot \delta\mathbf{x} \, dS \\ & + \int_{S_i}^{S_j} (-\mathbf{m}' + \mathbf{n} \times \boldsymbol{\gamma} - \mathbf{q}_m + \dot{\mathbf{i}} \dot{\boldsymbol{\omega}} + \boldsymbol{\omega} \times \dot{\mathbf{i}} \boldsymbol{\omega}) \cdot \delta\boldsymbol{\omega} \, dS \\ & \quad + [\mathbf{n}_{Ij} - \mathbf{f}_{n_{ij}}] \delta\mathbf{x}_i + [\mathbf{m}_{Ij} - \mathbf{f}_{m_{ij}}] \delta\boldsymbol{\omega}_i \\ & \quad + [\mathbf{n}_{iJ} - \mathbf{f}_{n_{ij}}] \delta\mathbf{x}_j + [\mathbf{m}_{iJ} - \mathbf{f}_{m_{ij}}] \delta\boldsymbol{\omega}_j = 0 \end{aligned} \quad (24)$$

Assuming that masses and inertias are lumped at the nodes, angular velocity and acceleration terms vanish from the integrals. Rewriting the boundary conditions in matrix form, we have:

$$\begin{aligned} & \int_{S_i}^{S_j} (-\mathbf{n}) \cdot \delta\mathbf{x} \, dS + \int_{S_i}^{S_j} (-\mathbf{m}' + \mathbf{n} \times \boldsymbol{\gamma}) \cdot \delta\boldsymbol{\omega} \, dS \\ & \quad - \int_{S_i}^{S_j} (\mathbf{q}_n \cdot \delta\mathbf{x} + \mathbf{q}_m \cdot \delta\boldsymbol{\omega}) \, dS \\ & = \{ \delta\mathbf{x}_i \quad \delta\boldsymbol{\omega}_i \quad \delta\mathbf{x}_j \quad \delta\boldsymbol{\omega}_j \} \begin{Bmatrix} \mathbf{f}_{nIj} \\ \mathbf{f}_{mIj} \\ \mathbf{f}_{n_iJ} \\ \mathbf{f}_{m_iJ} \end{Bmatrix} \end{aligned} \quad (25)$$

### 3.4.2 Determination of element end forces

In Eq. (25), the first line is coincident with the expression of the internal virtual work in static equilibrium. Introducing a *Lagrangian* linear interpolation in Eq. (17), the contribution of each element to the internal virtual work can be discretised. Considering two-node beam elements and using an intrinsic coordinate  $\xi$ , which takes

$\xi = -1$  when  $S = S_i$  and  $\xi = 1$  when  $S = S_j$ , internal forces and moments can be evaluated at their ends as follows:

$$\delta W_{\text{int}} = \delta \phi^T \int_{-1}^1 \begin{bmatrix} N_0 \mathbf{1} & \mathbf{0} & \frac{1}{j} N'_0 \mathbf{1} & \mathbf{0} \\ \mathbf{0} & N_0 \mathbf{1} & \mathbf{0} & \frac{1}{j} N'_0 \mathbf{1} \\ N_1 \mathbf{1} & \mathbf{0} & \frac{1}{j} N'_1 \mathbf{1} & \mathbf{0} \\ \mathbf{0} & N_1 \mathbf{1} & \mathbf{0} & \frac{1}{j} N'_1 \mathbf{1} \end{bmatrix} \begin{bmatrix} \mathbf{0} & \mathbf{0} \\ -\hat{\gamma} & \mathbf{0} \\ \mathbf{1} & \mathbf{0} \\ \mathbf{0} & \mathbf{1} \end{bmatrix} \begin{Bmatrix} \mathbf{n} \\ \mathbf{m} \end{Bmatrix} j d\xi \quad (26)$$

where  $N_0$  and  $N_1$  are the shape-functions for two-node beam elements based on Lagrange polynomials and  $N'_0$  and  $N'_1$  their derivatives:

$$N_0 = \frac{1}{2} (1 - \xi) \quad \text{and} \quad N_1 = \frac{1}{2} (1 + \xi) \quad (27)$$

$\delta \phi^T$  is  $\{\delta x_i \delta \omega_i \delta x_j \delta \omega_j\}$  and  $j$  is the Jacobian of the transformation that relates  $S$  and  $\xi$ , where  $S \in [0, L_e]$ :

$$j(\xi) = \frac{dS}{d\xi} = [N'_0(\xi) \quad N'_1(\xi)] \begin{Bmatrix} S_i \\ S_j \end{Bmatrix} = \frac{L_e}{2} \quad (28)$$

Finally, the out of balance forces/moments (disregarding external forces) are obtained computing the previous equation in the elements connected to node  $J$ :

$$\begin{aligned} \begin{Bmatrix} \tilde{\mathbf{f}}_{n_j} \\ \tilde{\mathbf{f}}_{m_j} \end{Bmatrix} &= - \begin{Bmatrix} \mathbf{f}_{n_{ij}} \\ \mathbf{f}_{m_{ij}} \end{Bmatrix} - \begin{Bmatrix} \mathbf{f}_{n_{jk}} \\ \mathbf{f}_{m_{jk}} \end{Bmatrix} \\ &= - \int_{-1}^1 \begin{bmatrix} N_1 \mathbf{1} & \mathbf{0} & \frac{1}{j} N'_1 \mathbf{1} & \mathbf{0} \\ \mathbf{0} & N_1 \mathbf{1} & \mathbf{0} & \frac{1}{j} N'_1 \mathbf{1} \end{bmatrix} \begin{bmatrix} \mathbf{0} & \mathbf{0} \\ -\hat{\gamma}_{ij} & \mathbf{0} \\ \mathbf{1} & \mathbf{0} \\ \mathbf{0} & \mathbf{1} \end{bmatrix} \begin{Bmatrix} \mathbf{n}_{ij} \\ \mathbf{m}_{ij} \end{Bmatrix} j d\xi \\ &\quad - \int_{-1}^1 \begin{bmatrix} N_0 \mathbf{1} & \mathbf{0} & \frac{1}{j} N'_0 \mathbf{1} & \mathbf{0} \\ \mathbf{0} & N_0 \mathbf{1} & \mathbf{0} & \frac{1}{j} N'_0 \mathbf{1} \end{bmatrix} \begin{bmatrix} \mathbf{0} & \mathbf{0} \\ -\hat{\gamma}_{jk} & \mathbf{0} \\ \mathbf{1} & \mathbf{0} \\ \mathbf{0} & \mathbf{1} \end{bmatrix} \begin{Bmatrix} \mathbf{n}_{jk} \\ \mathbf{m}_{jk} \end{Bmatrix} j d\xi \quad (29) \end{aligned}$$

### 3.4.3 Strains associated to rotations

The next step is to calculate the rotation and twist rate in each element. Following Crisfield and Jelenic [28, 49], a spherical interpolation of rotations throughout the element will be used for that purpose. For a 2-node element with nodes  $i, j$  and actual length  $L_e$ , the local rotation  $\hat{\Theta}_{ij}$ , between  $i$  and  $j$  is computed as follows:

$$\exp \hat{\Theta}_{ij} = \Lambda_i^T \Lambda_j \quad (30)$$

The rotation  $\Lambda_r$  at the midpoint of each element is used as element's reference rotation (Fig. 15); it is defined as:

$$\Lambda_r = \Lambda|_{\xi=0} = \Lambda_i \exp \left( \frac{1}{2} \hat{\Theta}_{ij} \right) \quad (31)$$

Spherical interpolation is defined through the local rotation  $\hat{\Psi}_e = \frac{1}{2} \hat{\Theta}_{ij}$  and the reference rotation, for  $\xi \in [-1, 1]$  as follows:

$$\Lambda(\xi) = \Lambda_r \exp \left( \xi \hat{\Psi}_e \right) \quad (32)$$

Making use of the definition of the rate of rotation  $\mathbf{K}$ :

$$\begin{aligned}\hat{\mathbf{K}}(\xi) &= \mathbf{\Lambda}^\top \frac{d}{dS} \mathbf{\Lambda} = \mathbf{\Lambda}^\top \frac{d}{d\xi} \mathbf{\Lambda} \frac{d\xi}{dS} \\ &= \exp(-\xi \hat{\Psi}_e) \mathbf{\Lambda}_r^\top \mathbf{\Lambda}_r \frac{d}{d\xi} \exp(\xi \hat{\Psi}_e) \frac{2}{L_e} \\ &= \mathbf{T}(\xi \hat{\Psi}_e)^\top \hat{\Psi}_e \frac{2}{L_e}\end{aligned}\quad (33)$$

Where  $\mathbf{T}$  is an operator that acts on a skew symmetric matrix  $\hat{\theta}$  as follows [80]:

$$\mathbf{T}(\hat{\theta}) = \mathbf{1} + \frac{1 - \cos \theta}{\theta^2} \hat{\theta} + \frac{\theta - \sin \theta}{\theta^3} \hat{\theta}^2 \quad (34)$$

In this expression,  $\theta$  is the modulus of the associated axial vector. Assuming that the strain is constant in each element and evaluating it at  $\xi = 0$ , the rate of rotation  $\mathbf{K}$ ,  $\hat{\Psi}_e$  results:

$$\mathbf{K} = \frac{2}{L_0} \Psi_e \quad (35)$$

and the deformational part is:

$$\mathbf{K}_d = \frac{2}{L_0} \Psi_e - \mathbf{K}_0 \quad (36)$$

where  $L_0$  is the prescribed target centreline length for each element.

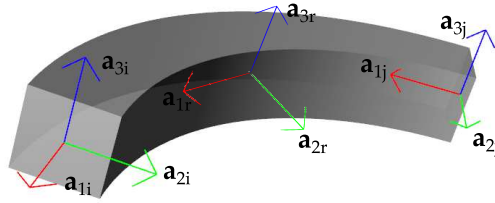


**Figure 15:** A typical element showing the nodal frames and the reference frame.  $\mathbf{\Lambda}_r$  is computed through spherical interpolation between  $\mathbf{\Lambda}_i$  and  $\mathbf{\Lambda}_j$ .

#### 3.4.4 Strains associated to translations

In contrast to the change of orientation, the strain associated to the translations is computed in a straightforward way, only taking into account the spatial position of the nodes  $i,j$ :

$$\gamma = \frac{1}{L_0} (\mathbf{x}_j - \mathbf{x}_i) \quad (37)$$

where  $\mathbf{x}_i, \mathbf{x}_j$  are the position vectors of the nodes  $i,j$  in spatial form. For rewriting it in material form,  $\gamma$  will be pre-multiplied by the transpose of the reference rotation matrix of the element. Finally, the deformational part is:

$$\Gamma_d = \mathbf{\Lambda}_r^\top \frac{1}{L_0} (\mathbf{x}_j - \mathbf{x}_i) - \{1, 0, 0\}^\top \quad (38)$$

### 3.5 NUMERICAL IMPLEMENTATION

The numerical solution of the dynamic equations is carried out via a one-step explicit algorithm based on Newmark's algorithm [98]. According to the laws of motion Eqs. (22a) and (22b), the dynamic equations in spatial configuration for node J at time  $t$  are:

$$\tilde{\mathbf{f}}_{n_j}^t = m_J \mathbf{a}_j^t + c_J \left( \dot{\mathbf{x}}_j^t + \mathbf{a}_j^t \frac{1}{2} \Delta t \right) \quad (39a)$$

$$\tilde{\mathbf{f}}_{m_j}^t = i_J \dot{\boldsymbol{\omega}}_j^t + \boldsymbol{\omega}_j^t \times i_J \boldsymbol{\omega}_j^t + c_J \boldsymbol{\omega}_j^t \quad (39b)$$

Matrices  $m_J$  and  $i_J$  represent the fictitious nodal masses and inertias. Matrix  $c_J$  represents damping. The obtention of  $m_J$  and  $i_J$  is based on the relation between the mechanical properties of the rod and the timescale  $\Delta t$  of the dynamic process; it ensures fast stability and avoids slow simulations. Based on reference [7], the following expressions in the material form are given:

$$\mathbb{M}_J = \frac{\Delta t^2}{2} \begin{bmatrix} \sum_{ne=1}^k \left( \frac{EA}{L_0} \right) & 0 & 0 \\ 0 & \sum_{ne=1}^k \left( \frac{GA_{Q2}}{L_0} \right) & 0 \\ 0 & 0 & \sum_{ne=1}^k \left( \frac{GA_{Q3}}{L_0} \right) \end{bmatrix} \quad (40a)$$

$$\mathbb{I}_J = \beta \frac{\Delta t^2}{2} \begin{bmatrix} \sum_{ne=1}^k \left( \frac{GJ}{L_0} \right) & 0 & 0 \\ 0 & \sum_{ne=1}^k \left( \frac{EI_2}{L_0} \right) & 0 \\ 0 & 0 & \sum_{ne=1}^k \left( \frac{EI_3}{L_0} \right) \end{bmatrix} \quad (40b)$$

Moreover, an additional coefficient  $\beta$  can be introduced to increase the damping and prevent non-convergence. Pulling back material variables, the spatial description of the fictitious nodal properties is:

$$m_J = \boldsymbol{\Lambda}_J \mathbb{M}_J \boldsymbol{\Lambda}_J^T \quad (41a)$$

$$i_J = \boldsymbol{\Lambda}_J \mathbb{I}_J \boldsymbol{\Lambda}_J^T \quad (41b)$$

Manipulating equations (39a) and (39b), it is possible to assess the translational  $\mathbf{a}_j^t$  and rotational  $\dot{\boldsymbol{\omega}}_j^t$  accelerations of the nodes  $\mathbf{x}_j$  at time  $t$ :

$$\mathbf{a}_j^t = \left( m_J + c_J \frac{1}{2} \Delta t \right)^{-1} \left( \tilde{\mathbf{f}}_{n_j}^t - c_J \dot{\mathbf{x}}_j^t \right) \quad (42a)$$

$$\dot{\boldsymbol{\omega}}_j^t = i_J^{-1} \left( \tilde{\mathbf{f}}_{m_j}^t - \boldsymbol{\omega}_j^t \times i_J \boldsymbol{\omega}_j^t - c_J \boldsymbol{\omega}_j^t \right) \quad (42b)$$

With the obtained translational accelerations, positions  $\mathbf{x}_j^{t+\Delta t}$  and translational velocities  $\dot{\mathbf{x}}_j^{t+\Delta t}$  are updated as:

$$\mathbf{x}_j^{t+\Delta t} = \mathbf{x}_j^t + \dot{\mathbf{x}}_j^t \Delta t + \frac{1}{2} \mathbf{a}_j^t \Delta t^2 \quad (43a)$$

$$\dot{\mathbf{x}}_j^{t+\Delta t} = C_1 \dot{\mathbf{x}}_j^t + C_2 \mathbf{a}_j^t \Delta t \quad (43b)$$

where  $C_1$  and  $C_2 \in [0, 1]$  are the terms of viscous damping used to avoid large oscillations in the free nodes, which can produce numerical instabilities [30]. Angular velocities  $\boldsymbol{\omega}_j^t$  and  $\boldsymbol{\omega}_j^{t+\Delta t}$  are not additive because they belong to different frames.

To overcome this problem, a strategy based on the one proposed by Ibrahimbegovic [46] to represent the change of orientation of sections is used:

$$\boldsymbol{\omega}_j^{t+\Delta t} = \mathbf{T}(\Delta\hat{\boldsymbol{\omega}}_j^t) \Delta\boldsymbol{\omega}_j^t + \exp(\Delta\hat{\boldsymbol{\omega}}_j^t) \boldsymbol{\omega}_j^t \quad (44)$$

with:

$$\Delta\boldsymbol{\omega}_j^t = \boldsymbol{\omega}_j^t \Delta t \quad (45a)$$

$$\Delta\hat{\boldsymbol{\omega}}_j^t = \hat{\boldsymbol{\omega}}_j^t \Delta t \quad (45b)$$

The operator  $\mathbf{T}$  has been defined in Eq. (34) and  $\exp(\Delta\hat{\boldsymbol{\omega}})$  can be calculated using Rodrigues's formula:

$$\exp(\Delta\hat{\boldsymbol{\omega}}) = \mathbf{1} + \frac{\sin \Delta\omega}{\Delta\omega} \Delta\hat{\boldsymbol{\omega}} + \frac{1 - \cos \Delta\omega}{\Delta\omega^2} \Delta\hat{\boldsymbol{\omega}}^2 \quad (46)$$

where  $\Delta\boldsymbol{\omega}$  is the incremental nodal rotation vector,  $\Delta\omega$  is its modulus and  $\Delta\hat{\boldsymbol{\omega}}$  is the antisymmetric matrix associated to  $\Delta\boldsymbol{\omega}$ . The update of the nodal rotation is therefore:

$$\boldsymbol{\Lambda}_j^{t+\Delta t} = \exp(\Delta\hat{\boldsymbol{\omega}}_j^t) \boldsymbol{\Lambda}_j^t \quad (47)$$

### 3.5.1 Criterium for convergency

The DR algorithm must iterate up to reach the criterium for convergency, based on the evaluation of translational and rotational kinetic energies:

$$\mathcal{K}_{t_j} = \frac{1}{2} \dot{\mathbf{x}}_j^T \mathbf{J} \dot{\mathbf{x}}_j \quad (48a)$$

$$\mathcal{K}_{r_j} = \frac{1}{2} \boldsymbol{\omega}_j^T \mathbf{J} \boldsymbol{\omega}_j \quad (48b)$$

$\mathcal{K}_{t_j}$  and  $\mathcal{K}_{r_j}$  are the kinetic energies corresponding to node J. When all energies reach a prescribed limit value, the solution is regarded as a static equilibrium configuration and the algorithm stops.

### 3.5.2 Boundary conditions

The choice of the geometrically exact rod model allows to introduce kinematic constraints in a straightforward way by the definition of the cross-section orientation. Moreover, neither fictitious extensions of the rod nor additional constraints are required, as in other models with 3 or 4 degrees of freedom [31]. In this work, the concept of form-finding is understood as a 'design-oriented' procedure [31], in which equilibrium is found after defining a target centreline length and the corresponding kinematic constraints. In other words, the proposed form-finding method is based on geometrical restrictions. The algorithm has been designed to deal with two possibilities: either positions and rotations at the beam ends are fixed, or positions are fixed and rotations are free.

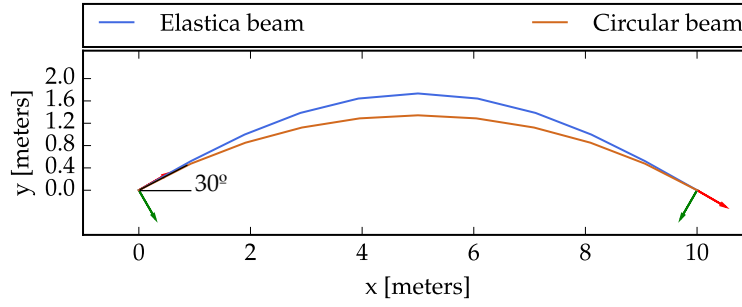


**Figure 16:** Form-finding of the elastica and the circular beam defined by the same local reference frames at the beam ends.

### 3.6 NUMERICAL TESTS

#### 3.6.1 The elastica and the circular beam

The first example is a beam clamped at both ends; the distance between them is 10 m. The mechanical properties of the beam are shown in Table 2 and correspond to a rectangular cross-section with 2 cm width and 0.5 cm depth; only  $I_2$  and  $A_{Q3}$  are relevant because the weak axis is assumed to be the bending axis. The modulus of elasticity is  $E = 10^4$  MPa, the relation  $E/G$  is 2.5 and the time increment is  $\Delta t = 0.0001$  s. The additional imposed kinematic boundary condition is the cross-section orientation at beam ends where the centreline of the curve forms an angle of  $30^\circ$  with the  $x$ -axis. Non-fixed nodal frames are initially defined by spherical interpolation.

Among the wide range of possible curves with different prescribed target lengths  $L_0$  that fulfil the established constraints, the *elastica* is defined by  $L_0 = 10.725$  m and the circular beam with radius  $R = 10$  m is defined by  $L_0 = 10.47$  m. Fig. 16 shows the equilibrium geometries in both cases using 10 elements. The errors registered for the  $y$ -coordinate at the midspan of the *elastica* and the circular beam are 0.05 % and 0.04 % respectively. Another straightforward way of validating these models is to assess curvatures  $\kappa$  of the beams. Fig. 17 shows an excellent correlation between numerical and analytical curvatures in both tests. The circular beam has a constant curvature of value  $\kappa = -0.1 \text{ m}^{-1}$  defined by the relation  $1/R$  whereas the curvature of the *elastica* can be calculated analytically [59, 67]. It is worth remarking that curvatures are computed at the Gauss's point of each element (at the middle of the element), not at nodes, as outlined above. For this reason, in the *elastica*, curvature values at elements 1 and 10 are very low but non-zero, since they do not correspond with the beam end nodes. Fig. 18 shows how the curve lengths grow to the target value  $L_0$  during the form-finding process.

| A<br>(cm <sup>2</sup> ) | $A_{Q2}$<br>(cm <sup>2</sup> ) | $A_{Q3}$<br>(cm <sup>2</sup> ) | J<br>(cm <sup>4</sup> ) | $I_2$<br>(cm <sup>4</sup> ) | $I_3$<br>(cm <sup>4</sup> ) |
|-------------------------|--------------------------------|--------------------------------|-------------------------|-----------------------------|-----------------------------|
| 1                       | 0.8333                         | 0.8333                         | 0.4621                  | 0.0208                      | 0.3333                      |

**Table 2:** Section properties of the *elastica* and the circular beam.

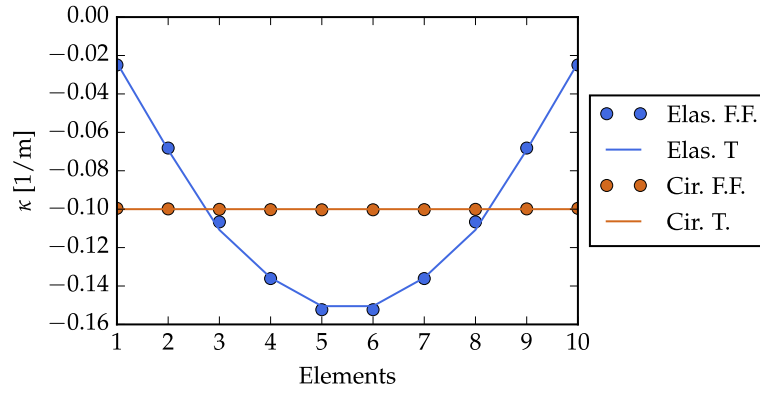


**Figure 17:** Curvatures for the *elastica* (Elas.) in blue and curvatures for the circular beam (Cir.) in brown. Form-finding (F.F.) and theoretical solutions (T.).

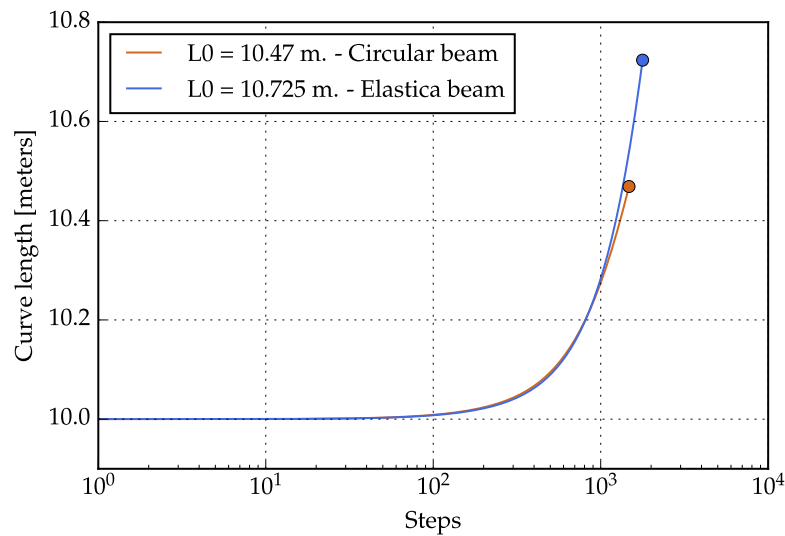


**Figure 18:** Evolution of the curve lengths for the *elastica* and the circular beam during the form-finding process.

| A<br>(in <sup>2</sup> ) | A <sub>Q2</sub><br>(in <sup>2</sup> ) | A <sub>Q3</sub><br>(in <sup>2</sup> ) | J<br>(in <sup>4</sup> ) | I <sub>2</sub><br>(in <sup>4</sup> ) | I <sub>3</sub><br>(in <sup>4</sup> ) | E<br>(lb/in <sup>2</sup> ) | E/G |
|-------------------------|---------------------------------------|---------------------------------------|-------------------------|--------------------------------------|--------------------------------------|----------------------------|-----|
| 1                       | 1                                     | 1                                     | 1/6                     | 1/12                                 | 1/12                                 | 10 <sup>7</sup>            | 2   |

**Table 3:** Material and section properties of the Bathe and Bolourchi cantilever beam.

In parallel, Fig. (19) shows the form-finding process at different stages, indicating both the number of the step and the actual curve length. Finally, this example allows to show that the method also works when the orientations of the beam ends are not restricted: allowing free rotations at both ends and establishing  $L_0 = 10.725$  m (length of the *elastica*), the start/final angle of the curve in the equilibrium state is 30.05°, practically the exact solution. In other words, allowing free rotations at both ends of the rod, the obtained curve is the *elastica* associated to the prescribed target length  $L_0$ .

### 3.6.2 Bathe and Bolourchi cantilever beam

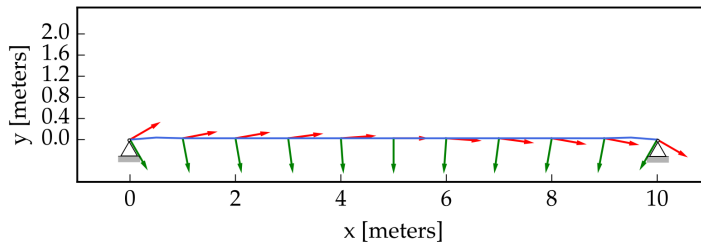
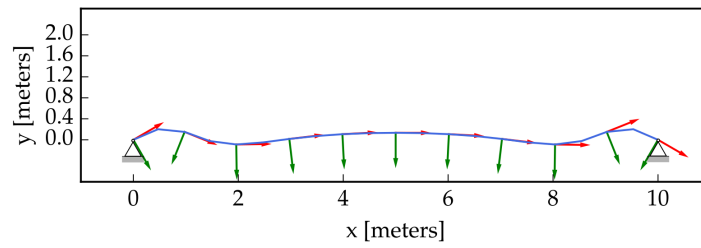
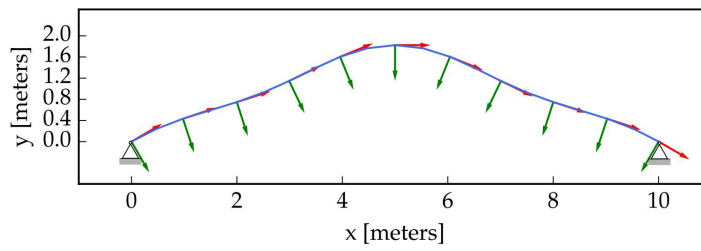
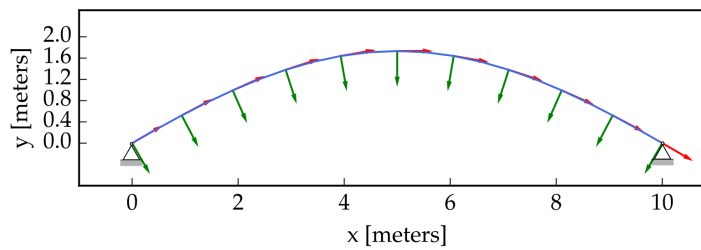
The second example is well-known in the finite-element literature [9]. The original problem is a circular cantilever beam clamped at the origin and subject to a force at its free node (Fig. 20). The units of the original problem have been kept for consistency. Initially, the curved beam is contained within the plane  $z = 0$ , the curve has a radius of 100 in comprising an angle of 45° and the material and section properties are shown in the Table 3. Bathe and Simo solved this problem taking into account a transverse force of 600 lb at the free end of the beam using 8 two-node elements in their models.

Knowing the solution by means of a implicit numerical tool based on Simo's model [89], it is possible to transform a load analysis example into a 'design oriented' form-finding problem by imposing the target kinematic constraints at both beam ends. Fig. (21) shows the evolution of the translational and rotational kinetic energies in the form-finding process. Moreover, three captures of the geometry at different stages show how initially the beam is practically straight (a) whereas and at the end of the process, when the kinetic energies are close to zero, the equilibrium geometry is reached according to the imposed orientations at both beam ends (c).

Fig. (22) shows the high correspondency between the nodal coordinates of the obtained solution by the implicit and the form-finding method using 8 two-node elements.

### 3.6.3 Combined bending and torsion

This example simulates the behaviour of a 10 m bent beam when its ends are clamped at a distance of 4.56 m and twisted 30°. For that purpose, the kinematic constraints at both ends are specified by setting the orientation of each cross-section through the definition of the corresponding reference frames (see Fig.23). By means of two elemental rotations, firstly, the tangent vectors are rotated an angle of 90° for simulating bending effects. When convergence is reached, a second form-finding step is carried out rotating the end frames about the tangent vectors an angle of 30° to evaluate twisting effects. Cross-section properties are shown in the Table 4. The modulus of elasticity is  $E = 10^4$  MPa, the relation  $E/G$  is 2.5 and the selected time

(a) Step 0;  $L = 10$  m.(b) Step 100;  $L = 10.17$  m.(c) Step 890;  $L = 10.69$  m.(d) Step 1780;  $L = 10.725$  m.

**Figure 19:** Evolution of the form-finding process of an *elastica* curve and its length ( $L$ ) at different stages.

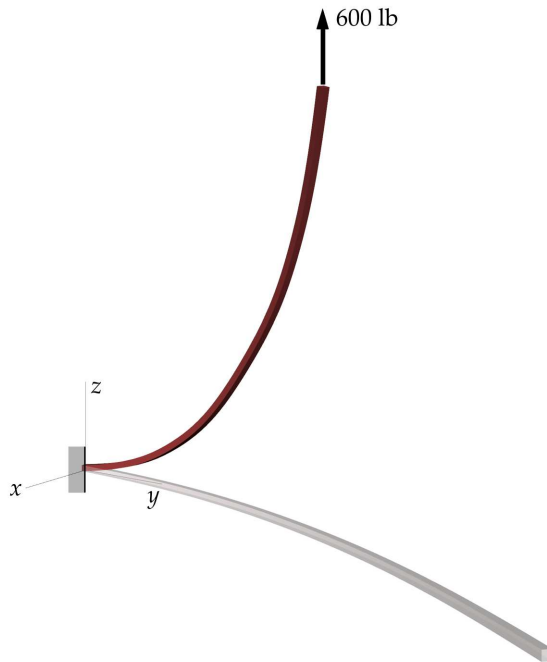


**Figure 20:** Original problem of the Bathe and Bolourchi cantilever beam.

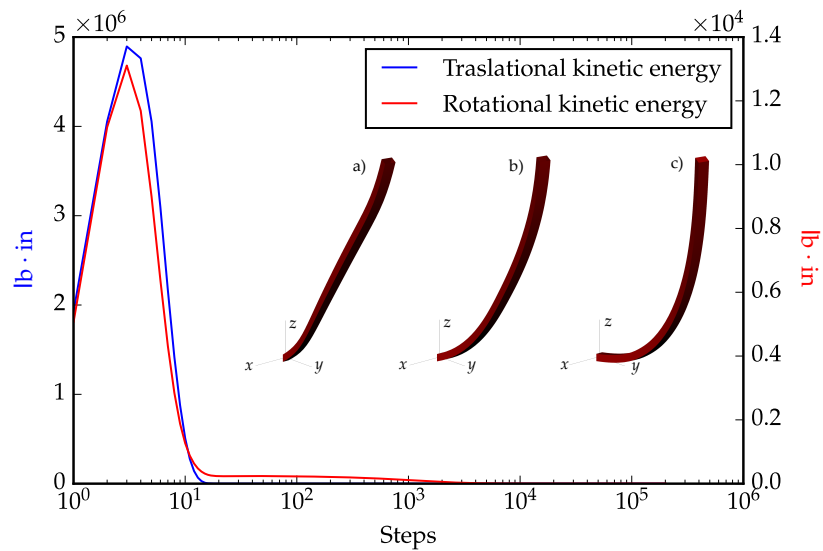


**Figure 21:** Evolution of the kinetic energies for the Bathe and Bolourchi cantilever beam. Figure a) shows the initial geometry. Figure b) corresponds to the geometry at step 100. Figure c) shows the final equilibrium geometry.

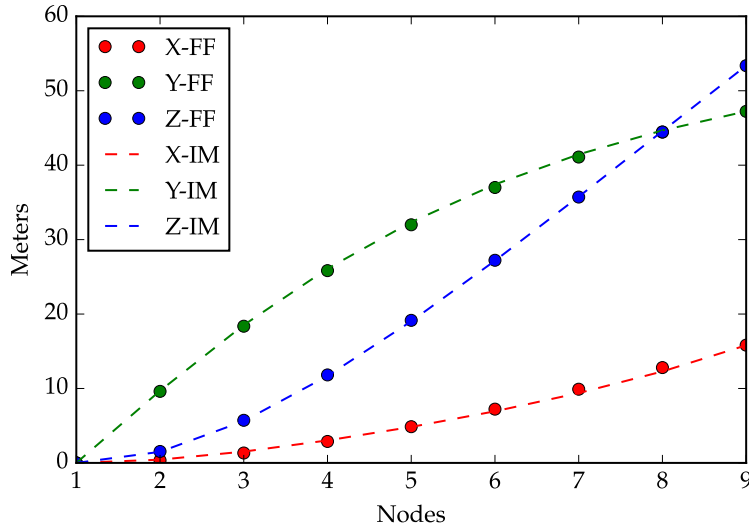


**Figure 22:** Coordinates X-Y-Z using the form-finding method (F.F.) and the implicit numerical solution based on Simo's theory (I.M.) for the Bathe and Bolourchi cantilever beam.

| A                  | A <sub>Q2</sub>    | A <sub>Q3</sub>    | J                  | I <sub>2</sub>     | I <sub>3</sub>     |
|--------------------|--------------------|--------------------|--------------------|--------------------|--------------------|
| (cm <sup>2</sup> ) | (cm <sup>2</sup> ) | (cm <sup>2</sup> ) | (cm <sup>4</sup> ) | (cm <sup>4</sup> ) | (cm <sup>4</sup> ) |
| 2400               | 2000               | 2000               | 91.147             | 32                 | 72                 |

**Table 4:** Section properties for the case of bending and torsion effects.

interval is  $\Delta t = 0.0001$  s. To assess the reliability of the method, the form-finding solution is compared with the obtained results by the same numerical implicit tool used in the example 2, based on Simo's procedure. Both models are discretised into an increasing number of elements (from 8 to 20) and ratios between coordinates corresponding to the node 'P' and the beam length are shown in Table 5.

The algorithm stops when both translational and rotational kinetic energies are under  $10^{-7}$  kN·m, after approximately 100.000 steps. As it can be seen in Table 4, the form-finding method provides reliable results; the error diminishes as the number of elements increases.

| Num. of elements | $\Delta y_p/L$ |        | $\Delta z_p/L$ |         |
|------------------|----------------|--------|----------------|---------|
|                  | I.M.           | F.F.   | I.M.           | F.F.    |
| 8                | 0.3796         | 0.3876 | -0.0357        | -0.0390 |
| 16               | 0.3795         | 0.3862 | -0.0343        | -0.0365 |
| 20               | 0.3795         | 0.3861 | -0.0341        | -0.0355 |

**Table 5:** Vertical and horizontal relative deflection for the bent and twisted beam taking into account different number of elements in both form-finding method (F.F.) and implicit method based on Simo's theory (I.M.).

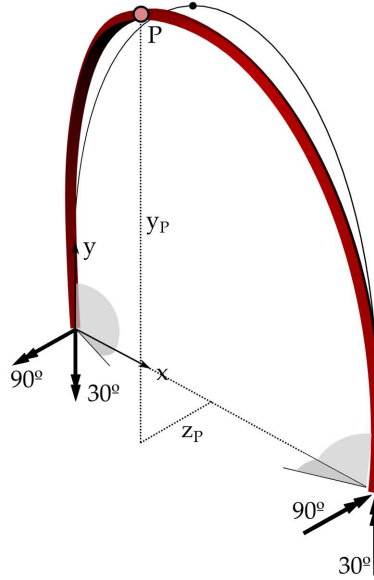


**Figure 23:** An initially straight rod is bent up to reach vertical tangents at supports and then twisted by rotating  $30^\circ$  its ends.

| $A$<br>( $\text{cm}^2$ ) | $A_{Q2}$<br>( $\text{cm}^2$ ) | $A_{Q3}$<br>( $\text{cm}^2$ ) | $J$<br>( $\text{cm}^4$ ) | $I_2$<br>( $\text{cm}^4$ ) | $I_3$<br>( $\text{cm}^4$ ) |
|--------------------------|-------------------------------|-------------------------------|--------------------------|----------------------------|----------------------------|
| 1                        | 0.5                           | 0.5                           | 0.0137                   | 2.0416                     | 0.0416                     |

**Table 6:** Section properties of the beam used in the shear deformability test.

### 3.6.4 Shear deformability test

This example is intended to study a case where shear effects are not negligible and can be simulated by the form-finding method presented in this work. The benchmark for this shear deformability test is the *elastica* of the first example with the same prescribed target length ( $L_0 = 10.725$  m) and distance between beam ends (10 m). The modulus of elasticity is  $E = 10^4$  MPa, the relation  $E/G$  is 2.5 and the selected time interval is  $\Delta t = 0.0001$  s. The mechanical properties of the beam under study are shown in Table 6. Such properties have been chosen to get a lower ratio between the shear stiffness and the bending stiffness than in the case of the *elastica*, being both cross-sectional areas equivalent. The relation between shear factors  $\alpha = 12EI_2/(GA_{Q3}L_0^2)$  in both cases is:

$$\alpha_{\text{shear test}} / \alpha_{\text{elastica}} = 163.5 \quad (49)$$

Fig. 24 shows the transverse shear deformations corresponding to both, the *elastica* case (blue) and the shear deformable case (brown). As expected, shear deformations are much larger than in the *elastica* case. Therefore, this example highlights the ability of the proposed form-finding method to reproduce shear deformable cases.

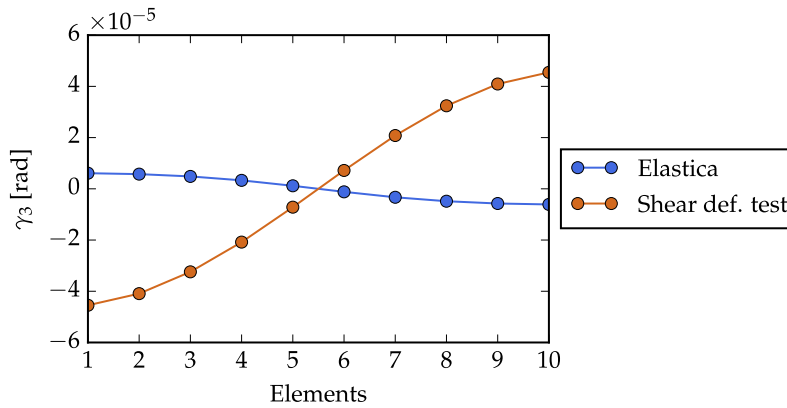


**Figure 24:** Shear deformations for the *elastica* and a beam where transverse shear is not negligible.

### 3.7 SUMMARY

A form-finding method for bending-active structures implementing the so-called geometrically exact rod model into a DR procedure has been developed. The geometrically exact beam model was designed by Reissner, Simo and other authors to handle mechanical problems of slender rods undergoing large displacements and rotations, therefore it has been selected as underlying mechanical model in our implementation. The use of 6 DoFs per node to update translations and rotations provides a complete description of the kinematics and allows for a straightforward definition of rotational boundary conditions. Key points in the specialisation of Reissner-Simo’s model to the DR procedure have been: the derivation of element end forces from the internal virtual work equation (sect. 3.4.2); the derivation of the expression of the change of orientation in the element (sect. 3.4.3); the definition of the numerical step using Newmark’s algorithm and the full expression of the inertial torques (Eq. 39b); and the update of angular velocities considering that nodal frames are changing (Eq. 44).

The DR algorithm developed in this thesis provides reliable results in terms of accuracy and computation time, as well as the possibility of monitoring the numerical process through different parameters: curve length, kinetic energies, number of steps or residual forces. In contrast to the work of other authors, in the studied examples the form-finding process is driven by kinematic constraints, defining restrictions at end nodes and using the beam length as a design parameter. It has been shown that the use of different lengths or end restrictions lead to meaningful solutions of the form-finding problem. The numerical examples also illustrated the ability and accuracy of the method to reproduce the configuration of active members starting from an initial geometry far from the equilibrium solution.

Despite the fact this method offers very promising results, the redirection of the PhD guidelines to the field of practise and application (as mentioned in Chapter 1), has fostered a shift to other more direct form-finding strategies. They will be presented in the following chapters.



# 4

## THE BENDING-ACTIVE TIED ARCH

” *The form is a system which organises itself in the presences of both internal and external forces and these organizations can shape patterns traced through mathematical rules.*

– **D’Arcy Wentworth Thompson**  
(Biologist)

### 4.1 INTRODUCTION

The development of computational form-finding tools has been of crucial importance to advance knowledge in modelling and behaviour of very flexible structures. As previously introduced in Chapters 2 and 3, numerical tools based on explicit methods as DR are the main trend today. Alternatively, the availability of FEM packages has also led to form-finding procedures based on finite element models [65]. Latest trends rely on the use of isogeometric finite elements implemented into a CAD environment [10, 11, 54].

Since the construction of the Mannheim Multihalle, these tools have served to design and built a number of dome-shaped grid-shells; many of them as temporary or experimental structures. However, the literature on their structural performance and efficiency in relation to their shape and member sizing is still limited. As it can be seen in the literature, most attention has been directed to solve the pure geometric problem.

Apart from the difficulty to find the equilibrium configuration of the structure, during the conceptual phase, the designer needs to find a compromise between member strength and flexibility. Curved members must be slender enough to keep activation stresses low. However, too slender members may be prone to local buckling and may render a too flexible structure. Indeed, many bending-active gridshells take advantage of double curvature to limit their deformability. For structures that need to support heavier loads and serviceability conditions are more strict, such as footbridges, the design space may be very limited, and this explains why there are very few bending-active examples among them.

The largest elastic gridshell realisations (Multihalle and Creteil) were built following Otto’s original idea: to assemble a grid of continuous members with rotation-free connections on the ground, and then to lift it (hoisting or pushing up) until the members’ ends can be fixed to the ground supports. The result is a lightweight shell-like structure which is stiff enough due to its shape, but whose members are light and easy to manipulate during the construction process. This design strategy has been often used in the design of smaller gridshells built in recent years. Nonetheless,

building with long continuous members is not free from drawbacks: a) the full assembly on the ground and subsequent lifting is limited to small and medium scales; the interferences between members and supports during the lifting process may cause difficulties; b) the applicability in the case of structures with larger loads is limited, like bridges or footbridges, mainly because of stiffness requirements. Recent contributions and methods are being proposed in this research field. Brancart *et al.* [23] have experimented an alternative type of reciprocal dome-shaped construction that makes use of the bending active principle, but is conceived as an assembly of individual elements that are sequentially put together to form the structure. Every element is made of two timber laths of slightly different lengths that are pre-bent and fixed together at their ends. This is a first approach to build three-dimensional bending active structures as kit-of-parts systems to avoid the need of a complete pre-assembly of a grid.

In this PhD thesis a new perspective for a well-established structural type which has been used at various scales is explored: the *beam string* [83]. It consists of a beam with an attached lower tie in tension and bracing struts (deviators) balancing the forces between them. The idea goes back to the gutter beams of the Crystal Palace (1851) and has been widely used to the present for large-scale structures. If a slender beam is used, the tension in the tie induces curvature in the beam and increases the structural depth of the system; this opens new formal possibilities and results in lightweight structures at the expense of increasing their overall flexibility. Systems of this type fall within the realm of active bending. The author will refer to them as *bending-active braced* (or *tied*) *arches*: a simple planar structure composed of a continuous flexible member that is activated by the action of main cables pulling at both ends of the rod, and secondary struts or cables that deviate the main cable and act at certain cross-section of the rod (Fig. 25). Secondary members will be referred to as deviators, no matter if they work under compression or under tension. The structure is activated by tensioning the cables and is stable under a certain state of self-stress. The geometry of the activated system cannot be fully prescribed in advance, as it depends on the length of the rod, its bending stiffness and the forces that are in equilibrium with the bent rod. The interest of simple tied arch systems lies in their applicability as individual structural modules to design lightweight footbridges [26] or roofing applications [70], these ones favored by moderate loads and less strict serviceability conditions.

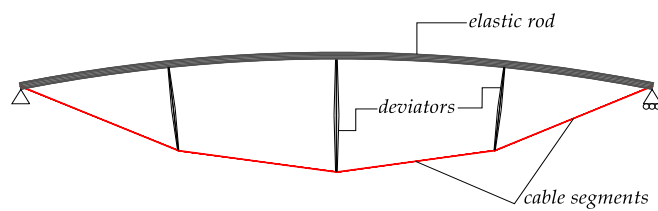


**Figure 25:** Bending-active tied arch.

In this structural system, assuming that the rod is slender and neglecting self-weight, a key observation is that each segment of the activated rod between deviators behaves as a segment of an inflexional *elastica*, whose scale is determined by the ratio between bending stiffness and compressive force [59]. A second key observation is that to each elastica segment corresponds a cable segment, and the axis of the cable segment joins the ideal inflexions of the corresponding elastica segment (Fig.

26). This enables the use of the closed-form expressions of the elastica to evaluate the shape and induced stress level in the active member.

Taking advantage of this idea, it is possible to devise an analytical method to generate shapes for bending-active braced arches by adequately choosing the design parameters in a sequential way. In other words, the process does not require to solve any system of equations since the solution is fully defined by compatibility and equilibrium conditions.

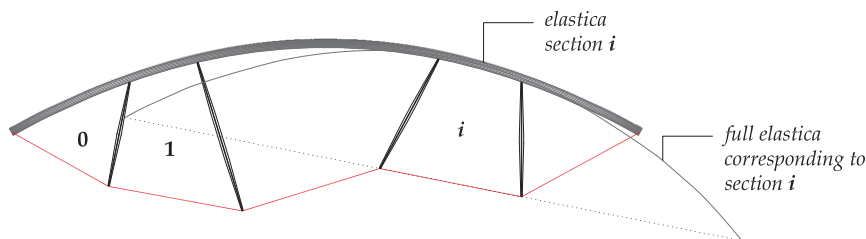


**Figure 26:** Full (notional) elastica corresponding to segment  $i$ .

#### 4.1.1 Outline of the chapter

The main purposes of this chapter are: (a) to present the bending-active tied arch as a proposal of application for the design of lightweight structures; (b) to devise an analytical method to determine activated shapes for such kind of structures. For a better comprehension of the core topic, the problem will be approached starting with a brief review of the inflexional elastica. The necessary equilibrium and compatibility conditions to obtain the self-stress states of the elastica are shown in section 4.2. The proposed methodology is presented in sections 4.4 and 4.5. At the end of each section, some examples demonstrate the capacities of the method.

## 4.2 A BRIEF REVIEW OF THE INFLEXIONAL ELASTICA<sup>1</sup>

The problem of planar bending of an initially straight rod subject to compressive forces at its ends, assuming non-extensibility and non-shear deformability, and neglecting self-weight is known as the elastica problem. It was first studied by Euler, based on Bernoulli's assumption of proportionality between flexural moments  $M$  and centreline curvatures  $\kappa$  at each cross-section. In order to simplify the description, the analysis is restricted to the fundamental aspects of the elastica problem. The full development of this theory can be found in the classical work by Love [67].

<sup>1</sup> This section is based on the article: Bessini, J.; Lázaro, C.; Casanova, J.; Monleón, S. (2019) "Efficiency-based design of bending-active tied arches". *Engineering Structures*. Vol. 200, 1 December 2019, 109681.

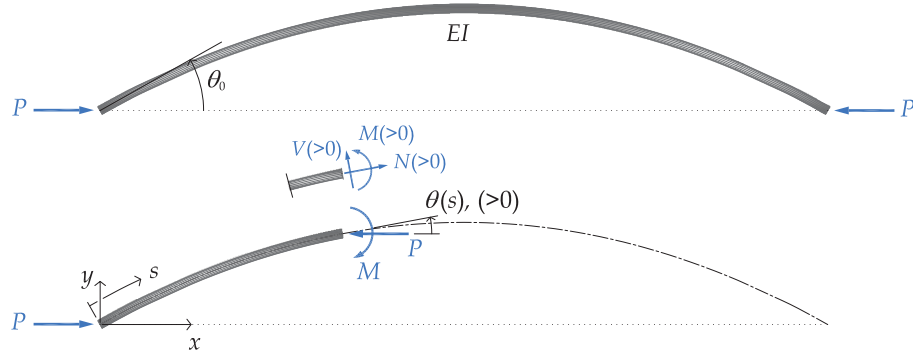


**Figure 27:** Inflexional elastica.

The constitutive equation for the elastica is  $M = EI \kappa$  where the curvature is expressed as  $\kappa = d\theta/ds$ ,  $ds$  is an arc-length parameter,  $\theta$  is the cross-section rotation and  $EI$  the flexural stiffness. The analytical solution for the arc-length is:

$$s = \frac{1}{2} \sqrt{\frac{EI}{P}} \int_{-\theta_0}^{\theta} \frac{1}{\sqrt{\sin^2 \frac{\theta_0}{2} - \sin^2 \frac{\theta}{2}}} d\theta \quad (50)$$

The applicability of this expression is bounded into the interval  $-\theta_0 \leq \theta \leq \theta_0$ , where  $\theta_0$  is the cross-section rotation at the inflexion. In order to handle this issue, Love [67] introduced the variable  $\omega$ , defined by:

$$\omega = \frac{\sin \frac{\theta}{2}}{\sin \frac{\theta_0}{2}} \quad (51)$$

substituting in 50, the expression for the arc-length reads as follows:

$$s = \sqrt{\frac{EI}{P}} \int_{-\pi/2}^{\omega} \frac{1}{\sqrt{1 - k^2 \sin^2 \omega}} d\omega \quad (52)$$

where  $k = \sin \frac{\theta_0}{2}$  is the reference parameter of the dimensionless solution of the elastica. The integral can reproduce arbitrarily long elasticas, because the new variable  $\omega$  is not bounded. The solution can be expressed in terms of the *incomplete* and the *complete elliptic integrals of the first kind*

$$F(\omega, k) = \int_0^{\omega} \frac{d\omega}{\sqrt{1 - k^2 \sin^2 \omega}} \quad K(k) = \int_{-\pi/2}^0 \frac{d\omega}{\sqrt{1 - k^2 \sin^2 \omega}} \quad (53)$$

as:

$$s(\omega, k) = \sqrt{\frac{EI}{P}} (F(\omega, k) + K(k)) \quad (54)$$

#### 4.2.1 Configuration of the elastica

Using the *incomplete and complete elliptic integrals of the second kind*

$$E(\omega, k) = \int_0^{\omega} \sqrt{1 - k^2 \sin^2 \omega} d\omega \quad E(k) = \int_0^{\pi/2} \sqrt{1 - k^2 \sin^2 \omega} d\omega \quad (55)$$

the coordinates of the elastica are expressed as follows (note the difference in nomenclature between  $E$  and  $E$ ):

$$x(\omega, k) = 2 \sqrt{\frac{EI}{P}} (E(\omega, k) + E(k)) - s(\omega, k) \quad (56a)$$

$$y(\omega, k) = 2 \sqrt{\frac{EI}{P}} k \cos \omega \quad (56b)$$

#### 4.2.2 Section forces

Normal forces and shear forces are obtained as projections of the compressive force, and bending moments as the product of the compressive force times the elastica ordinate:

$$N = -P \cos \theta \quad (57a)$$

$$V = P \sin \theta \quad (57b)$$

$$M = -Py \quad (57c)$$

They can be expressed in terms of the elastica parameters as:

$$N(\omega, k) = -P(1 - 2k^2 \sin^2 \omega) \quad (58a)$$

$$V(\omega, k) = -2Pk \sin \omega \sqrt{1 - k^2 \sin^2 \omega} \quad (58b)$$

$$M(\omega, k) = -2\sqrt{P}\sqrt{EI}k \cos \omega \quad (58c)$$

#### 4.2.3 Scalability of the solution

The parameter *critical length* is introduced:

$$l_c = \pi \sqrt{\frac{EI}{P}} \quad (59)$$

defined as the length of a rod with bending stiffness  $EI$  for which  $P$  is Euler's critical load —this definition was previously introduced by Lázaro *et al.* in [59]. Using this definition, the arc-length and the coordinates of the elastica can be expressed as dimensionless quantities:

$$\zeta = s/l_c \quad \xi = x/l_c \quad \eta = y/l_c \quad (60)$$

Therefore, the non-dimensional arc-length parameter is:

$$\zeta(\omega, k) = \frac{1}{\pi} (F(\omega, k) + K(k)) \quad (61)$$

and the non-dimensional coordinates are:

$$\xi(\omega, k) = \frac{2}{\pi} (E(\omega, k) + E(k)) - \zeta(\omega, k) \quad (62a)$$

$$\eta(\omega, k) = \frac{2}{\pi} k \cos \omega \quad (62b)$$

These equations show that *the shape* of an elastica is fully determined by the parameter  $k$  —or in other words, by the angle at the inflexion (Fig. 28).

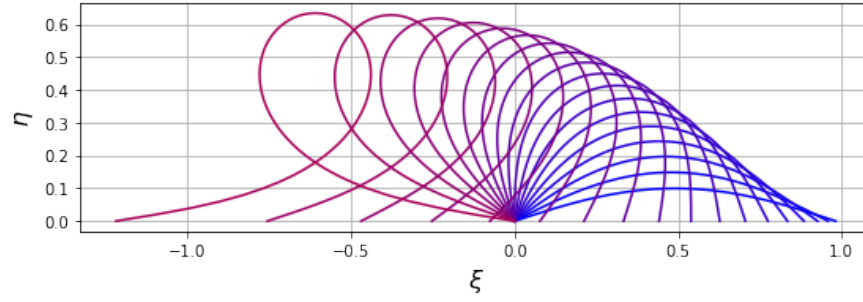


**Figure 28:** Elasticas (non-dimensional coordinates) for  $\theta_0 = n\pi/20$  and  $n \in \{2, 3, \dots, 17, 18\}$ .

On the other hand, *the size* of the elastica is determined by the critical length  $l_c$ , which acts as a scaling parameter.

Finally, from equation (58) can be noted that section forces  $N, V$  are directly scaled by the compressive force  $P$ , and bending moments  $M$  are scaled by the product of  $P$  and the critical length.

To sum up, the shape of the elastica –defined by the parameter  $k$ – is fully determined by the angle at the inflexion  $\theta_0$ , and is totally independent from the value of the compressive force  $P$  or the bending stiffness  $EI$ . Once the shape is obtained, the size of the elastica can be scaled by means of the critical length  $l_c$  (Eq. 59). It involves the relation between the bending stiffness  $EI$  and the compressive force  $P$ .

For example, once  $l_c$  has been fixed, the magnitude of the internal forces can be chosen by selecting  $P$ , and the bending stiffness  $EI$  should then be adjusted to be consistent with  $l_c$ :

$$EI = P \left( \frac{l_c}{\pi} \right)^2 \quad (63)$$

Alternatively,  $EI$  may be prescribed and the magnitude of the forces will be given by:

$$P = \pi^2 \frac{EI}{l_c^2} \quad (64)$$

### 4.3 SELF-STRESS STATES IN BENDING-ACTIVE TIED ARCHES

The simulation of the activation process of bending-active structures is of crucial importance for their design. Due to the non-linearity of the structural response, it is often not possible to predefine in advance the equilibrium configuration and computational form-finding methods are required for modelling the bending effect. However, in the case of bending-active tied arches, the fact that the rod segments between deviators behave as elastica segments, enables the use of closed-form expressions to evaluate the stress level due to activation forces. The purpose of this section is to determine the sufficient and necessary conditions for obtaining the self-stress state of the arch using the equations of the exact solution of the elastica.

#### 4.3.1 Notation

An intermediate node  $i$  on the rod separates two sections of the rod that will be referred to as section  $i - 1$ , and section  $i$ . Variables associated to the section  $i$  will

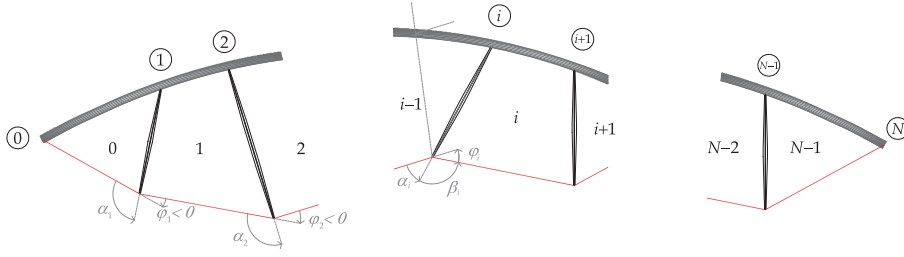


Figure 29: Notation.

be denoted by the superscript  $i$  (Fig. 29). Every section is part of an elastica defined by the parameter  $k^i$ , the magnitude of the compressive force  $P^i$  and the flexural stiffness  $EI^i$ .

As each cable segment and the corresponding elastica section are in equilibrium, the compressive force acting on the elastica and the traction in the cable must have the same value:  $P^i = T^i$ .

Angles between cable segments  $i-1$ ,  $i$  and elastica tangents at each side of node  $i$  will be referred to as  $\theta_i^{i-1}$  and  $\theta_i^i$ . Therefore a given elastica section  $i$  starts with an angle  $\theta_i^i$  and ends with  $\theta_i^{i+1}$ , both angles referred to the orientation of cable  $i$ . The corresponding elastica parameters are  $\omega_i^i$  and  $\omega_{i+1}^i$ , in agreement with Eq. (51).

The angles formed by each cable segment  $i-1$ ,  $i$  and the prolongation of the axis of the deviator are denoted  $\alpha_i$ ,  $\beta_i$ . The angular difference between cable segments is denoted as  $\varphi_i$ . Then, the relation between angles at node  $i$  is:

$$\alpha_i + \beta_i + \varphi_i = \pi \quad (65)$$

#### 4.3.2 Equilibrium and compatibility conditions at joints

Figure 30 shows the various equilibrium conditions at nodes. Equilibrium of moments at joints requires that  $M_i^{i-1} = M_i^i$ . Substituting the expression for moments:

$$\sqrt{T^{i-1}} \sqrt{EI^{i-1}} k^{i-1} \cos \omega_i^{i-1} = \sqrt{T^i} \sqrt{EI^i} k^i \cos \omega_i^i \quad (66)$$

equivalently:

$$T^{i-1} EI^{i-1} (k^{i-1})^2 (1 - \sin^2 \omega_i^{i-1}) = T^i EI^i (k^i)^2 (1 - \sin^2 \omega_i^i) \quad (67)$$

Introducing the definition of  $\omega$  and rearranging, the equilibrium condition can be expressed in terms of the rotations:

$$T^{i-1} EI^{i-1} \left( (k^{i-1})^2 - \sin^2 \frac{\theta_i^{i-1}}{2} \right) = T^i EI^i \left( (k^i)^2 - \sin^2 \frac{\theta_i^i}{2} \right) \quad (68)$$

An alternative expression using critical lengths is:

$$\frac{1}{\pi^2} (T^{i-1})^2 (l_c^{i-1})^2 \left( (k^{i-1})^2 - \sin^2 \frac{\theta_i^{i-1}}{2} \right) = \frac{1}{\pi^2} (T^i)^2 (l_c^i)^2 \left( (k^i)^2 - \sin^2 \frac{\theta_i^i}{2} \right) \quad (69)$$

The equilibrium of forces at each node on the elastica is defined by the compressive forces acting on each segment  $P^{i-1}$ ,  $P^i$  and the force in the deviator  $Q_i$ . The

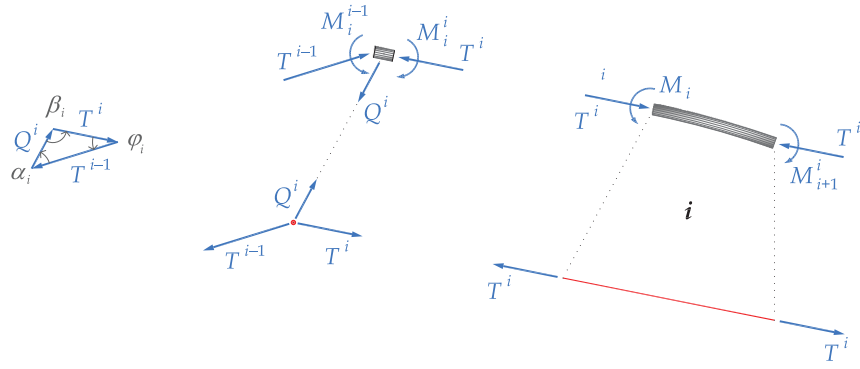


**Figure 30:** Equilibrium of nodes and elastica sections.

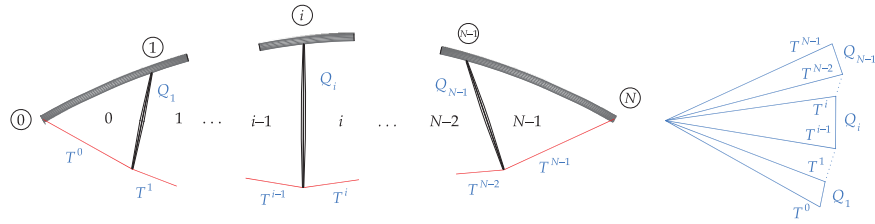


**Figure 31:** Cables, deviators and force polygon.

triangle of forces at this node is the same as the triangle of forces at the corresponding node joining cable segments and deviator, acted by forces  $T^{i-1}$ ,  $T^i$ ,  $Q_i$ . The law of sines

$$\frac{T^{i-1}}{\sin \beta_i} = \frac{T^i}{\sin \alpha_i} = \frac{Q_i}{\sin \varphi_i} \quad (70)$$

leads to the following equilibrium equations:

$$T^{i-1} \sin \alpha_i = T^i \sin \beta_i \quad (71a)$$

$$T^{i-1} \sin \varphi_i = Q_i \sin \beta_i \quad (71b)$$

Compatibility of tangents to the elastica at both sides of a joint requires:

$$\theta_i^i = \theta_i^{i-1} + \varphi_i \quad (72)$$

A problem with  $n$  elastica sections, and therefore  $N - 1$  intermediate nodes in the rod, is considered. Following the previous discussion, the intervening variables are classified into three groups. The first group is reflected in Table 7 and gathers variables which are directly related to the self-stressing state: angles between cables and between deviators and cables, cable forces relative to the force in the first cable and deviator forces relative to the same magnitude. They can be visualised by means of a force polygon composed by cable forces and deviator forces (Fig. 31). Note that the choice of the magnitude of the force  $T^0$  determines the scale of the force polygon.

The second group (Table 8) comprises the variables that define the geometry (shape and relative size) of the sequence of elasticas: elastica parameters, critical lengths relative to the critical length of the first elastica section and angles at both sides of a node.

| Type  | Notation    |                         | Number of variables |
|-------|-------------|-------------------------|---------------------|
| Angle | $\varphi_i$ | $i \in \{1 \dots n-1\}$ | $n-1$               |
| Angle | $\alpha_i$  | $i \in \{1 \dots n-1\}$ | $n-1$               |
| Force | $T^i/T^0$   | $i \in \{1 \dots n-1\}$ | $n-1$               |
| Force | $Q_i/T^0$   | $i \in \{1 \dots n-1\}$ | $n-1$               |
| Total |             |                         | $4(n-1)$            |

**Table 7:** Variables related to self-stressing forces.

| Type          | Notation                     |                         | Number of variables |
|---------------|------------------------------|-------------------------|---------------------|
| Angle         | $\theta_i^{i-1}, \theta_i^i$ | $i \in \{1 \dots n-1\}$ | $2(n-1)$            |
| Angle-related | $k_i$                        | $i \in \{0 \dots n-1\}$ | $n$                 |
| Length        | $l_c^i/l_c^0$                | $i \in \{1 \dots n-1\}$ | $n-1$               |
| Total         |                              |                         | $4(n-1) + 1$        |

**Table 8:** Variables related to the form of the elastic rod.

The third group (Table 9) is formed by the size and force scaling parameters: the critical length of the first elastica section and the force in the first cable.

Altogether, there are  $8n - 5$  variables defining the configuration:  $4(n - 1)$  self-stress related variables;  $4(n - 1) + 1$  rod form related variables; one parameter  $l_c^0$  to define the size of the structure, and one parameter  $F^0$  to define the magnitude of internal forces and stiffness of the structure.

As far as equations are concerned, there are three equilibrium equations and one compatibility condition at each intermediate node of the rod (Table 10). This makes a total of  $4(n - 1)$  equations. Therefore, a given configuration is defined by choosing  $4(n - 1) + 3$  parameters:  $4(n - 1) + 1$  for determining the shape, one for setting the size and one for selecting the magnitude of forces and flexural stiffness of cross-sections.

#### 4.4 DIRECT DETERMINATION OF SELF-STRESS CONFIGURATIONS

In this section a direct method to obtain self-stress configurations of bending-active tied arches is presented. This method is direct in the sense that a solution for the  $4(n - 1)$  unknowns is obtained in a sequential manner, after selecting  $4(n - 1) + 3 = 4n - 1$  parameters, and does not require to solve any system of equations.

Observing that the  $2(n - 1)$  force equilibrium equations (71) at intermediate nodes only involve the  $4(n - 1)$  self-stress related variables of Table 7, the following procedure solves the problem:

| Type   | Notation | Number of variables |
|--------|----------|---------------------|
| Length | $l_c^0$  | 1                   |
| Force  | $T^0$    | 1                   |
| Total  | 2        |                     |

**Table 9:** Size and force scaling variables.

| Type          | Notation   | Number of equations |
|---------------|--|---------------------|
| Equilibrium   | $T^{i-1} \sin \alpha_i = T^i \sin \beta_i$   | $n - 1$             |
| Equilibrium   | $T^{i-1} \sin \varphi_i = Q_i \sin \beta_i$  | $n - 1$             |
| Equilibrium   | $(T^{i-1})^2 (l_c^{i-1})^2 \left( (k^{i-1})^2 - \sin^2 \frac{\theta_i^{i-1}}{2} \right)$<br>$= (T^i)^2 (l_c^i)^2 \left( (k^i)^2 - \sin^2 \frac{\theta_i^i}{2} \right)$ | $n - 1$             |
| Compatibility | $\theta_i^i = \theta_i^{i-1} + \varphi_i$  | $n - 1$             |
| Total         |  | $4(n - 1)$          |

**Table 10:** Equilibrium and compatibility equations.

1. Define a value for  $T^0$
2. Define values for  $\alpha_i, \varphi_i, i \in \{1 \dots n-1\}$ . In this step,  $2(n - 1)$  parameters are set.
3. Compute  $T^i$  and  $Q_i$  for,  $i \in \{1 \dots n-1\}$  using force equilibrium equations (71). This is a direct computation considering that  $\beta_i = \pi - \alpha_i - \varphi_i$ .
4. Define values for  $\theta_i^{i-1}, i \in \{1 \dots n-1\}$ . With this step  $n - 1$  parameters are additionally set.
5. Compute  $\theta_i^i$  using compatibility equations (72).
6. Define values for  $k_0$  and  $EI^i$  for  $i \in \{0 \dots n-1\}$ . This step sets  $n + 1$  additional parameters.
7. Compute  $k_i$  for  $i \in \{1 \dots n-1\}$  using moment equilibrium equations (68).
8. Compute local coordinates of elastica  $i$  using equations (56).
9. Place each elastica segment by translating it to the end of the previous one and rotating it to preserve tangents at intermediate nodes.

It is worth noting that steps 1 to 3 are equivalent to the definition of the force polygon that corresponds to the system of cables and deviators. This graphical approach has been already used by other authors. In Boulic *et al.* [22] proposed a graphical method for the design of hybrid bending-active structures composed of active elements with non-constant stiffness and tensile cable nets. Particularly, their method makes use of a force diagram to obtain the non-constant distribution of bending stiffness along the active members for a certain target bent geometry under given loads.

Step 4 requires to check that angle  $\theta_i^i$  is larger than  $\theta_{i-1}^i$  to avoid sense reversal at elastica  $i$ . If this happens,  $2\pi$  has to be added to  $\theta_i^i$ .

In step 6,  $k_0$  is related to the angle between cable and elastica tangent at the start of the structure. In addition, setting the  $n$  values of flexural stiffness  $EI^i$  is equivalent to setting the  $n$  values of critical length  $l_c^i$  because forces  $T^i$  are already known.

| Prescribed       |        | Computed     |        |
|------------------|--------|--------------|--------|
| Variable         | Number | Variable     | Number |
| $T^0$            | 1      | $T^i$        | $n-1$  |
| $\varphi_i$      | $n-1$  | $Q_i$        | $n-1$  |
| $\alpha_i$       | $n-1$  |              |        |
| $\theta_i^{i-1}$ | $n-1$  | $\theta_i^i$ | $n-1$  |
| $k^0$            | 1      |              |        |
| $EI^i$           | $n$    | $k^i$        | $n-1$  |
| Total            | $4n-1$ | Total        | $4n-4$ |

**Table 11:** Prescribed and computed variables in the direct method.

Once a configuration is found, its size and the magnitude of the forces can be adjusted to the desired values by changing  $EI^0$  and  $T^0$ . A convenient procedure is to initially set  $T^0 = 1$  and  $EI^0 = 1/\pi^2$ , so that  $l_c^0 = 1$ . After computing the solution and the coordinates of the structure, the size of the structure can be scaled to the desired value. If the scale factor is assumed as  $l$ ; then the first critical length shall be  $l_c^0 = l$ . If  $EI^0 = EI$  is chosen as a desired value, then all forces shall be scaled by  $T^0 = \pi^2 EI/l^2$ . Another possibility is to choose the magnitude of forces by setting  $T^0 = T$  and then obtain the required flexural stiffness scale factor as  $EI^0 = Tl^2/\pi^2$ .

Table 11 summarises the prescribed variables and the computed variables for this direct method.

#### 4.4.1 Examples

**GENERIC CASE** A generic case with  $n = 5$  elastica sections with the following data (Table 12) is shown here. Adopting  $T^0 = 1$ ,  $EI^i = 1/\pi^2 \forall i$

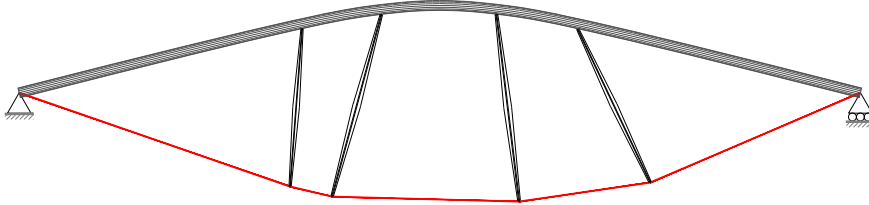


**Figure 32:** Generic bending-active tied arch with  $n = 5$  elastica sections.

**PERPENDICULAR DEVIATORS** Perpendicularity between deviators and rod can be prescribed adding the following condition:

$$\theta_i^{i-1} = \pi/2 + \alpha_i \quad (73)$$

| Variable    | Prescribed    | Computed | Variable     | Prescribed                            | Computed |
|-------------|---------------|----------|--------------|---------------------------------------|----------|
| $T^0$       | 1             |          | $\theta_1^0$ | $30\pi/180$                           |          |
| $T^1$       |               | 0.9430   | $\theta_2^1$ | $10\pi/180$                           |          |
| $T^2$       |               | 0.9623   | $\theta_3^2$ | $-5\pi/180$                           |          |
| $T^3$       |               | 0.9595   | $\theta_4^3$ | $-15\pi/180$                          |          |
| $T^4$       |               | 0.8601   | $\theta_1^1$ |                                       | 0.2616   |
| $Q_1$       |               | 0.2600   | $\theta_2^2$ |                                       | 0.0435   |
| $Q_2$       |               | 0.1261   | $\theta_3^3$ |                                       | -0.1742  |
| $Q_3$       |               | 0.1258   | $\theta_4^4$ |                                       | -0.5229  |
| $Q_4$       |               | 0.2572   | $k^0$        | $\sin(\frac{1}{2} \frac{40\pi}{180})$ |          |
| $\varphi_1$ | $-15\pi/180$  |          | $k^1$        |                                       | 0.2645   |
| $\varphi_2$ | $-7.5\pi/180$ |          | $k^2$        |                                       | 0.2482   |
| $\varphi_3$ | $-7.5\pi/180$ |          | $k^3$        |                                       | 0.2625   |
| $\varphi_4$ | $-15\pi/180$  |          | $k^4$        |                                       | 0.3532   |
| $\alpha_1$  | $-70\pi/180$  |          | $EI^0$       | $1/\pi^2$                             |          |
| $\alpha_2$  | $-95\pi/180$  |          | $EI^1$       | $1/\pi^2$                             |          |
| $\alpha_3$  | $275\pi/180$  |          | $EI^2$       | $1/\pi^2$                             |          |
| $\alpha_4$  | $-60\pi/180$  |          | $EI^3$       | $1/\pi^2$                             |          |
|             |               |          | $EI^4$       | $1/\pi^2$                             |          |

**Table 12:** Prescribed variables and computed unknowns for the generic case.

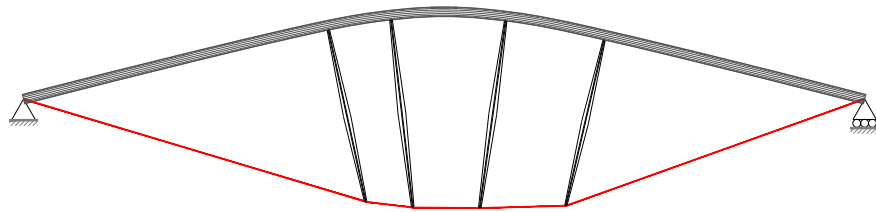


**Figure 33:** Bending-active tied arch with  $n = 5$  elastica sections and perpendicular deviators.

| Variable    | Prescribed    | Computed | Variable     | Prescribed                            | Computed |
|-------------|---------------|----------|--------------|---------------------------------------|----------|
| $T^0$       | 1             |          | $\theta_1^0$ | $30\pi/180$                           |          |
| $T^1$       |               | 0.8964   | $\theta_2^1$ | $10\pi/180$                           |          |
| $T^2$       |               | 0.8836   | $\theta_3^2$ | $-5\pi/180$                           |          |
| $T^3$       |               | 0.9016   | $\theta_4^3$ | $-15\pi/180$                          |          |
| $T^4$       |               | 1.0056   | $\theta_1^4$ |                                       | 0.2616   |
| $Q_1$       |               | 0.2681   | $\theta_2^4$ |                                       | 0.0435   |
| $Q_2$       |               | 0.1172   | $\theta_3^4$ |                                       | -0.2182  |
| $Q_3$       |               | 0.1182   | $\theta_4^4$ |                                       | -0.5229  |
| $Q_4$       |               | 0.2696   | $k^0$        | $\sin(\frac{1}{2} \frac{40\pi}{180})$ |          |
| $\varphi_1$ | $-15\pi/180$  |          | $k^1$        |                                       | 0.2697   |
| $\varphi_2$ | $-7.5\pi/180$ |          | $k^2$        |                                       | 0.2580   |
| $\varphi_3$ | $-7.5\pi/180$ |          | $k^3$        |                                       | 0.2743   |
| $\varphi_4$ | $-15\pi/180$  |          | $k^4$        |                                       | 0.3451   |
| $\alpha_1$  |               | -1.0471  | $EI^0$       | $1/\pi^2$                             |          |
| $\alpha_2$  |               | -1.3962  | $EI^1$       | $1/\pi^2$                             |          |
| $\alpha_3$  |               | -1.6579  | $EI^2$       | $1/\pi^2$                             |          |
| $\alpha_4$  |               | -1.8316  | $EI^3$       | $1/\pi^2$                             |          |
|             |               |          | $EI^4$       | $1/\pi^2$                             |          |

**Table 13:** Prescribed variables and computed unknowns corresponding to the generic case with perpendicular deviators.

**SYMMETRIC STRUCTURE WITH EVEN NUMBER OF ELASTICA SECTIONS** The following additional conditions lead to a symmetric solution for a  $n$  even number of elastica sections:

- Conditions on the polygon of forces:

$$\varphi_{n-i} = \varphi_i \quad \text{for } i \in \{1 \dots n/2 - 1\} \quad (74a)$$

$$\alpha_{n-i} = \pi - \varphi_i - \alpha_i \quad \text{for } i \in \{1 \dots n/2 - 1\} \quad (74b)$$

$$\alpha_{n/2} = (\pi - \varphi_{n/2})/2 \quad (74c)$$

- Conditions on the geometry of the rod:

$$\theta_{n-i}^{n-i-1} = -\theta_i^i \quad \text{for } i \in \{1 \dots n/2 - 1\} \quad (75a)$$

$$\theta_{n/2}^{n/2-1} = -\varphi_{n/2}/2 \quad (75b)$$

$$EI^{n-i-1} = EI^i \quad \text{for } i \in \{0 \dots n/2 - 1\} \quad (75c)$$

Therefore, symmetry adds  $n - 1$  conditions to the force polygon and  $n$  conditions to the form of the rod. This leaves  $(4n - 1) - (2n - 1) = 2n$  free variables to determine a configuration. A different approach to symmetry is to reduce the number of unknowns and equations from scratch. In the symmetric case with even number of elastica sections there are  $4n - 2$  variables.

Table 14 shows the splitting between prescribed and computed variables with the direct method. The equations and their number are shown in Table 15.

Let's consider a structure with  $n = 4$  rod sections. Table 16 includes the  $2n = 8$  prescribed parameters and the  $2n - 1 = 7$  computed unknowns following the procedure described in the preceding section. The resulting geometry is represented in Figure 34.

| Prescribed       |           | Computed               |           |
|------------------|-----------|------------------------|-----------|
| Variable         | Number    | Variable               | Number    |
| $T^0$            | 1         | $T^i$                  | $n/2 - 1$ |
| $\varphi_i$      | $n/2$     | $Q_i$                  | $n/2$     |
| $\alpha_i$       | $n/2 - 1$ | $\alpha_{n/2}$         | 1         |
| $\theta_i^{i-1}$ | $n/2 - 1$ | $\theta_{n/2}^{n/2-1}$ | 1         |
| $k^0$            | 1         | $\theta_i^i$           | $n/2 - 1$ |
| $EI^i$           | $n/2$     | $k^i$                  | $n/2 - 1$ |
| Total            | $2n$      | Total                  | $2n - 1$  |

**Table 14:** Prescribed and computed variables in a symmetric structure with even number of elastica sections (direct method).

| Type          | Notation   | Number of equations |
|---------------|--|---------------------|
| Equilibrium   | $T^{i-1} \sin \alpha_i = T^i \sin \beta_i$   | $n/2 - 1$           |
| Equilibrium   | $T^{i-1} \sin \varphi_i = Q_i \sin \beta_i$  | $n/2 - 1$           |
| Symmetry      | $\alpha_{n/2} = (\pi - \varphi_{n/2})/2$   | 1                   |
| Equilibrium   | $T^{n/2-1} \sin \varphi_{n/2} = Q_{n/2} \sin \beta_{n/2}$  | 1                   |
| Equilibrium   | $(T^{i-1})^2 (l_c^{i-1})^2 \left( (k^{i-1})^2 - \sin^2 \frac{\theta_i^{i-1}}{2} \right)$<br>$= (T^i)^2 (l_c^i)^2 \left( (k^i)^2 - \sin^2 \frac{\theta_i^i}{2} \right)$ | $n/2 - 1$           |
| Compatibility | $\theta_i^i = \theta_i^{i-1} + \varphi_i$  | $n/2 - 1$           |
| Symmetry      | $\theta_{n/2}^{n/2-1} = \varphi_{n/2}/2$   | 1                   |
| Total         |  | $2n - 1$            |

**Table 15:** Equations in a symmetric structure with even number of elastica sections.

| Variable    | Prescribed    | Computed | Variable     | Prescribed                            | Computed |
|-------------|---------------|----------|--------------|---------------------------------------|----------|
| $T^0$       | 1             |          | $\theta^0$   | $30\pi/180$                           |          |
| $T^1$       |               | 0.9659   | $\theta_1^1$ |                                       | 0.2617   |
| $Q_1$       |               | -0.2588  | $\theta_2^1$ |                                       | 0.0654   |
| $Q_2$       |               | -0.1263  | $k^0$        | $\sin(\frac{1}{2} \frac{40\pi}{180})$ |          |
| $\varphi_1$ | $-15\pi/180$  |          | $k^1$        |                                       | 0.2622   |
| $\varphi_2$ | $-7.5\pi/180$ |          | $EI^1$       | $1/\pi^2$                             |          |
| $\alpha_1$  | $105\pi/180$  |          | $EI^0$       | $1/\pi^2$                             |          |
| $\alpha_2$  |               | 1.6362   |              |                                       |          |

**Table 16:** Prescribed variables and computed unknowns in the symmetric example.

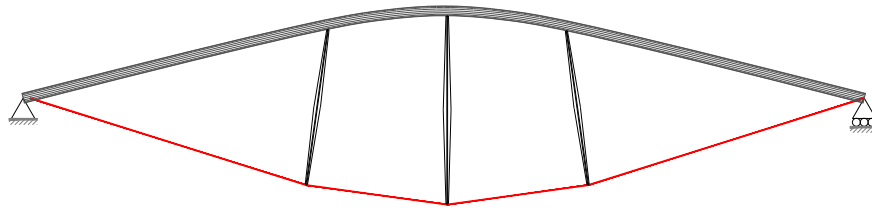


**Figure 34:** Symmetric bending-active tied arch with  $n = 4$  elastica sections.

| Prescribed       |           | Computed     |           |
|------------------|-----------|--------------|-----------|
| Variable         | Number    | Variable     | Number    |
| $T^0$            | 1         | $T^i$        | $(n-1)/2$ |
| $\varphi_i$      | $(n-1)/2$ | $Q_i$        | $(n-1)/2$ |
| $\alpha_i$       | $(n-1)/2$ |              |           |
| $\theta_i^{i-1}$ | $(n-1)/2$ |              |           |
| $k^0$            | 1         | $\theta_i^i$ | $(n-1)/2$ |
| $EI^i$           | $(n+1)/2$ | $k^i$        | $(n-1)/2$ |
| Total            | $2n+1$    | Total        | $2n-2$    |

**Table 17:** Prescribed and computed variables in a symmetric structure with odd number of elastica sections (direct method).

| Type          | Notation   | Number of equations |
|---------------|--|---------------------|
| Equilibrium   | $T^{i-1} \sin \alpha_i = T^i \sin \beta_i$   | $(n-1)/2$           |
| Equilibrium   | $T^{i-1} \sin \varphi_i = Q_i \sin \beta_i$  | $(n-1)/2$           |
| Equilibrium   | $(T^{i-1})^2 (l_c^{i-1})^2 \left( (k^{i-1})^2 - \sin^2 \frac{\theta_i^{i-1}}{2} \right)$<br>$= (T^i)^2 (l_c^i)^2 \left( (k^i)^2 - \sin^2 \frac{\theta_i^i}{2} \right)$ | $(n-1)/2$           |
| Compatibility | $\theta_i^i = \theta_i^{i-1} + \varphi_i$  | $(n-1)/2$           |
| Total         |  | $2n-2$              |

**Table 18:** Equations in a symmetric structure with odd number of elastica sections.

**SYMMETRIC STRUCTURE WITH ODD NUMBER OF ELASTICA SECTIONS** This case can be solved using the following additional constraints:

$$\varphi_{n-i} = \varphi_i \quad \text{for } i \in \{1 \dots (n-1)/2\} \quad (76a)$$

$$\alpha_{n-i} = \pi - \varphi_i - \alpha_i \quad \text{for } i \in \{1 \dots (n-1)/2\} \quad (76b)$$

$$\theta_{n-i}^{n-i-1} = -\theta_i^i \quad \text{for } i \in \{1 \dots (n-1)/2\} \quad (76c)$$

$$EI^{n-i-1} = EI^i \quad \text{for } i \in \{0 \dots (n-3)/2\} \quad (76d)$$

Alternatively, a reduced number of variables and equations can be used. Variables and equations can be found in Tables 17 and 18.

#### 4.5 COMPUTATION OF SELF-STRESS CONFIGURATIONS UNDER ADDITIONAL CONSTRAINTS

In section 4.4 it was shown that  $4(n-1) + 3 = 4n - 1$  variables can be independently selected in a pure form-finding problem. The remaining  $4(n-1) = 4n - 4$  unknown variables that define a configuration can be calculated using the same number of equations:  $3(n-1)$  equilibrium and  $n-1$  compatibility equations.

In the event that additional constraints are imposed, the number of independent parameters to determine the equilibrium configuration is reduced. For instance, when searching symmetric configurations or solutions with perpendicularity between rod and deviators. However, when alternative choices for the parameters are selected, the problem becomes non-linear and can be solved using suitable techniques.

Among the set of search strategies, heuristic algorithms are well known for providing good approximate solutions to problems that cannot be solved easily using other techniques. Within heuristics, evolutionary algorithms have been deeply developed in the last decade. They mimic the theory of evolution using the same trial-and-error procedures that nature uses in order to arrive at an optimised outcome. Using this idea, Rutten [82] created a tool called *Galapagos*, which facilitates this process within *Grasshopper* (a graphical algorithm editor). By the definition of the form-finding variables and constraints, this evolutionary solver finds in an iterative manner, the exact solution of the problem (or at least, a near-optimal solution).

**EXAMPLE 1** In this first example, the target is to find the shape of a symmetric bending active arch with four rod sections ( $n = 4$ ) of equal flexural stiffness and length. Cable and rod forces are prescribed, as well as the angle between first cable and first tangent to the rod.

Firstly, it will be checked that the number of prescribed variables and conditions allows to find a solution. As shown in the previous section, a symmetric bending active arch with even number of rod sections leaves  $2n = 8$  parameters to be chosen.  $T^0 = 1$  and  $EI^0 = 1/\pi^2$  are chosen as starting values, and will be modified at the end of the process to achieve the desired size of the structure. This leaves freedom to define *six* additional parameters and/or conditions. Once  $T^0$  has been chosen, the other forces  $T^1$ ,  $Q_0$  and  $Q_1$  and the angle  $\alpha_2$  are determined if the angles  $\varphi_1$ ,  $\varphi_2$  and  $\alpha_1$  are selected, as shown in the example of the previous section. Table 16 shows the values of angles and forces.

Three conditions remain to be set in order to find the solution:

- The angle between the first cable and the first tangent:

$$\theta_0^0 = -40\pi/180 \quad (77)$$

Therefore:

$$k^0 = \sin\left(\frac{1}{2} \frac{40\pi}{180}\right) \quad (78)$$

- Equal stiffness values in all rod sections:  $n/2 - 1 = 1$  condition.

$$EI^1 = EI^0 (= 1) \quad (79)$$

- Equal length in all rod sections:  $n/2 - 1 = 1$  condition.

$$s^1 = s^0 \quad (80)$$

From equation (50), the lengths of each elastica segment can be expressed as follows:

$$s^0 = \sqrt{\frac{EI^0}{T^0}} \left( F(\omega_1^0, k^0) + K(k^0) \right) \quad (81a)$$

$$s^1 = \sqrt{\frac{EI^1}{T^1}} \left( F(\omega_2^1, k^1) - F(\omega_1^1, k^1) \right) \quad (81b)$$

Therefore, equations (79) and (80) result in:

$$T^1 \left( F(\omega_1^0, k^0) + K(k^0) \right) - T^0 \left( F(\omega_2^1, k^1) - F(\omega_1^1, k^1) \right) = 0 \quad (82)$$

with:

$$\sin \omega_1^0 = \frac{1}{k^0} \sin \frac{\theta_1^0}{2} \quad (83a)$$

$$\sin \omega_1^1 = \frac{1}{k^1} \sin \frac{\theta_1^1}{2} \quad (83b)$$

$$\sin \omega_2^1 = \frac{1}{k^1} \sin \frac{\theta_2^1}{2} \quad (83c)$$

The previous equations together with: (a) the moment equilibrium equation; (b) the compatibility condition in node 1 and (c) the symmetry condition in node 2:

$$T^0(k^0)^2(1 - \sin^2 \omega_1^0) - T^1(k^1)^2(1 - \sin^2 \omega_1^1) = 0 \quad (84a)$$

$$\theta_1^1 = \theta_1^0 - \varphi_1 \quad (84b)$$

$$\theta_2^1 = \varphi_2/2 \quad (84c)$$

allow to calculate the four unknowns  $\theta_1^0$ ,  $\theta_1^1$ ,  $\theta_2^1$  and  $k^1$ . In this case, the solution has been found iterating over  $\theta_1^0$  using the plug-in *Galapagos* until:

$$s^1 - s^0 = 0 \quad (85)$$

The result is shown in the Fig. 35 and Table 19.

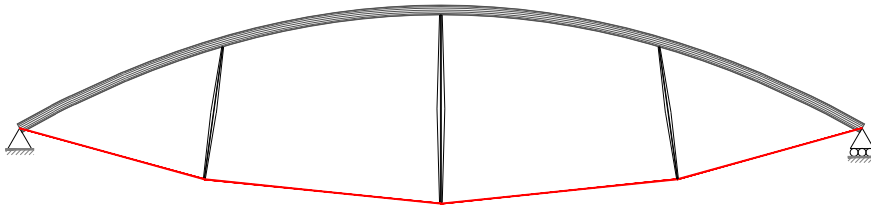


**Figure 35:** Symmetric bending-active arch with  $n = 4$  elastica sections of equal length (example 1).

| Variable    | Prescribed    | Computed | Variable     | Prescribed                            | Computed |
|-------------|---------------|----------|--------------|---------------------------------------|----------|
| $T^0$       | 1             |          | $\theta_1^1$ |                                       | 0.3202   |
| $T^1$       |               | 0.9659   | $\theta_2^1$ |                                       | 0.0654   |
| $Q_1$       |               | -0.2645  | $k^0$        | $\sin(\frac{1}{2} \frac{40\pi}{180})$ |          |
| $Q_2$       |               | -0.1262  | $k^1$        |                                       | 0.2440   |
| $\varphi_1$ | $-15\pi/180$  |          | $EI^0$       | $1/\pi^2$                             |          |
| $\varphi_2$ | $-7.5\pi/180$ |          | $EI^1$       | $1/\pi^2$                             |          |
| $\alpha_1$  | $105\pi/180$  |          | $\theta_1^0$ |                                       | 0.5880   |
| $\alpha_2$  |               | 1.6361   |              |                                       |          |

**Table 19:** Prescribed variables and computed unknowns in the example 1.

**EXAMPLE 2** Here, the objective is to reproduce the first example adding the condition of perpendicularity between deviators and rod. Due to this condition, the solution can be found iterating over  $\alpha_1$  instead of  $\theta_1^0$ . The solution is shown in the Fig. 36 and Table 20.

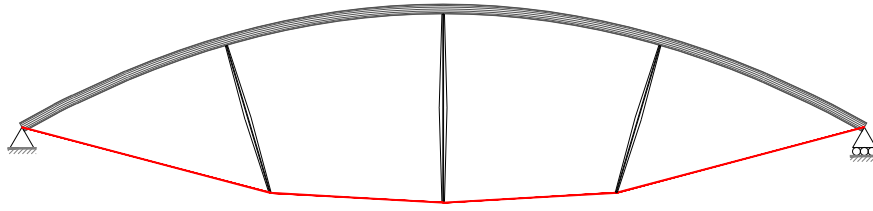


**Figure 36:** Symmetric bending-active tied arch corresponding to the example 2.

| Variable    | Prescribed    | Computed | Variable     | Prescribed                            | Computed |
|-------------|---------------|----------|--------------|---------------------------------------|----------|
| $\Gamma^0$  | 1             |          | $\theta_1^0$ |                                       | 0.5868   |
| $\Gamma^1$  |               | 0.8769   | $\theta_1^1$ |                                       | 0.3191   |
| $Q_1$       |               | 0.2785   | $\theta_2^1$ |                                       | 0.0654   |
| $Q_2$       |               | -0.1460  | $k^0$        | $\sin(\frac{1}{2} \frac{40\pi}{180})$ |          |
| $\varphi_1$ | $-15\pi/180$  |          | $k^1$        |                                       | 0.2513   |
| $\varphi_2$ | $-7.5\pi/180$ |          | $EI^0$       | $1/\pi^2$                             |          |
| $\alpha_2$  |               | 1.6361   | $EI^1$       | $1/\pi^2$                             |          |
|             |               |          | $\alpha_1$   |                                       | -0.9839  |

**Table 20:** Prescribed variables and computed unknowns in the example 2.

**EXAMPLE 3** In the last example, the purpose is to form-find the shape of a symmetric bending active arch with  $n = 5$  rod sections, with perpendicular deviators and same distance between deviator-rod joints projected over the  $x$ -axis. The cable and rod forces as well as the angle between first cable and first tangent to the rod are prescribed. Relations  $EI^0/EI^1$  and  $EI^0/EI^2$  are iteratively searched in two steps through *Galapagos* until achieving:

$$\frac{d_x^1}{d_x^0} = \frac{x^2 - x^1}{x^1 - x^0} = 1 \quad (86a)$$

$$d_x^2 = d_x^0/2 \quad (86b)$$

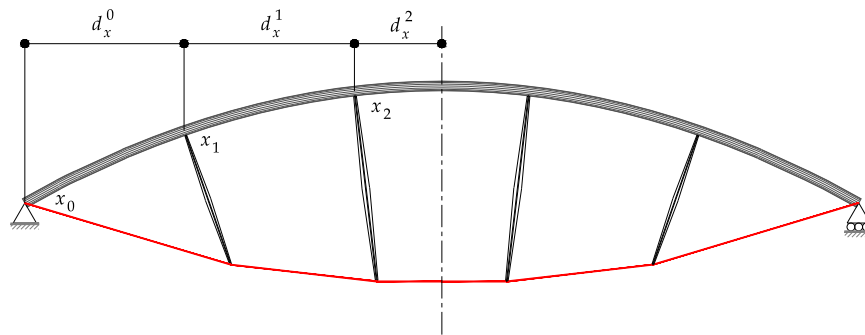


**Figure 37:** Symmetric bending-active tied arch corresponding to the example 3.

| Variable    | Prescribed    | Computed | Variable     | Prescribed                            | Computed |
|-------------|---------------|----------|--------------|---------------------------------------|----------|
| $T^0$       | 1             |          | $\theta_1^0$ |                                       | 0.5236   |
| $T^1$       |               | 0.8963   | $\theta_1^1$ |                                       | 0.2609   |
| $T^2$       |               | 0.8835   | $\theta_2^1$ |                                       | 0.1745   |
| $Q_1$       |               | 0.2688   | $\theta_2^2$ |                                       | 0.0432   |
| $Q_2$       |               | 0.1174   | $k^0$        | $\sin(\frac{1}{2} \frac{40\pi}{180})$ |          |
| $\varphi_1$ | $-15\pi/180$  |          | $k^1$        |                                       | 0.1719   |
| $\varphi_2$ | $-7.5\pi/180$ |          | $k^2$        |                                       | 0.1423   |
| $\alpha_1$  | $-\pi/3$      |          | $EI^0$       | $1/\pi^2$                             |          |
| $\alpha_2$  | $-80\pi/180$  |          | $EI^1$       |                                       | 0.4466   |
|             |               |          | $EI^2$       |                                       | 0.5029   |

**Table 21:** Prescribed variables and computed unknowns in the example 3.

## 4.6 SUMMARY

The bending-active braced (or tied) arch has been presented. The system is a hybrid between a tied arch and a cable-strut beam: a simple planar structure composed of a continuous flexible member that is activated by the action of main cables pulling at both ends of the rod, and secondary struts or cables that deviate the main cable and act at certain cross-section of the rod. The target shape of the system is achieved as a result of the tensioning process and needs to be pre-determined by means of a specific analysis, typically involving dynamic relaxation or optimisation-based methods. In this chapter, a specific design procedure for this structural type has been proposed. The method is based on the observation that each segment of the activated rod between deviators behaves as a segment of elastica; this makes possible the use of closed-form expressions to evaluate the shape and induced stress level in the active member.

First of all, a brief review of the inflexional elastica has been presented. In this study the relationship between the shape, the activation forces and the scalability of the solution has been stated. Taking advantage of this idea, the self-stress states in bending-active tied arches can be evaluated in terms of non-dimensional parameters, which make the results applicable to a wide variety of scales and cross-sectional sizes.

In section 4.4, a direct method to obtain self-stress configurations of bending-active tied arches has been presented. The shaping process is carried out in a sequential way by adequately choosing the design parameters, and does not require to solve any system of equations since the solution is fully defined by compatibility and equilibrium conditions. When alternative choices for the parameters are selected, the number of independent parameters is reduced and the problem becomes non-linear. In that case, the use of heuristic algorithms has been proposed as a suitable technique to find an optimised solution. Finally, some examples with different design constraints have been reproduced to illustrate the possibilities of the method.



# 5

## EFFICIENCY-BASED DESIGN OF BENDING-ACTIVE TIED ARCHES

” *Form follows function.*

– **Louis Henry Sullivan**

(Architect)

This chapter is an adaptation of the published peer-reviewed paper: Bessini, J.; Lázaro, C.; Casanova, J.; Monleón, S. (2019) "Efficiency-based design of bending-active tied arches". *Engineering Structures*. Vol. 200, 1 December 2019, 109681.

### 5.1 INTRODUCTION

Traditionally, the design of a bending-active structures has been oriented to the determination of the initial geometry of the system, and in some cases, to the evaluation of the effects due to the self-weight and activation forces. However, once the target shape has been reached and stabilised, the structural response to external loads is considerably influenced by the inherited stress state. Therefore, the assessment of the structural performance is crucial to ensure the appropriateness of the solution as resistant scheme as well as its structural efficiency. In the analysis stage, when external loads are applied, the structure generally has a quasi-linear behaviour, but the stress state inherited from the activation stage, in addition to influencing the structural behaviour, has a direct impact in the structural capacity of the bending-active rods. In spite of that, there is a large number of references dealing with form-finding methods for bending-active structures, whereas the literature on their performance in relation to their shape and member proportioning is scarce.

The observation that each segment of the rod behaves as an elastica segment was presented in Chapter 4. It allows to make use of the exact solution of the elastica to evaluate the shape and influence of the choice of the cross-section and bending stiffness on the initial stress level. One of the main conclusions of this study is the established relationship between shape, activation forces and scalability. Taking advantage of this, it is possible to find the equilibrium configuration of the system in terms of non-dimensional magnitudes and to generalise the results for flexible members of any length and stiffness. However, this analytical methodology does not allow evaluating the structural response of the system when external loads are applied. Therefore, non-linear finite element models are needed to assess the applicability and efficiency of braced arches as structural modules to design lightweight structures.

This chapter addresses the relationship between configuration finding and structural performance in bending-active braced arches. Starting from a fixed length and given cross-sections, and introducing prestressing forces in cables, different structural configurations for a three-strut tied arch with perpendicular deviators are simulated. From these results, stress levels after the activation of the structure as functions of the rise-to-span ratio and the slenderness of the active member are obtained. Finally, further numerical analysis has led to establish relationships between shape, length and slenderness associated to the serviceability limit state and the ultimate limit state limitations imposed by the Eurocode for footbridges.

### 5.1.1 Outline of the chapter

The chapter is structured as follows: In section 5.2, an analytical expression to evaluate the self-stress after activation in elastica semi-waves is detailed. The correspondence between the structural behaviour of a rod segment between deviators in tied arches and the exact solution of the elastica curve is numerically exemplified in section 5.3. In section 5.4 numerical experiments are carried out to evaluate the structural performance due to activation forces and loading models. Section 5.5 shows an example of how to design a particular bending-active tied arch using the developed methodology. Finally, a procedure to extend the previous results to tied arches with an arbitrary number  $n$  of deviators is described in section 5.6.

## 5.2 STRESS LEVELS AFTER ACTIVATION IN ELASTICA SEMI-WAVES

In this section, an analytical expression based on the equations of the elastica to quantify the utilisation of the material due to the activation process is proposed. Moreover, the influence of the interverning variables, such as the slenderness of the rod, the shape of the cross-section or the selected material is examined.

### 5.2.1 Evaluation of the utilisation ratio

According to the EN 1993-1-1 (Eurocode 3) and as a conservative approximation, the linear summation of the utilisation ratio for each stress resultant may be used to verify the ultimate strength of the cross-section (see equation (6.2) in [42]). This criterion can be written as:

$$\frac{N}{N_u} + \frac{M}{M_u} \leq 1 \quad (87)$$

where  $N$  and  $M$  are the section forces produced by bending of a initial straight rod;  $N_u$  and  $M_u$  are the design values of the ultimate axial forces and bending moments respectively, without considering buckling reduction factors. Substituting (58) in (87) leads to the expression of the utilisation ratio in terms of elastica parameters:

$$\frac{P}{f_u A} g(\omega, k) + \frac{P l_c}{f_u W} h(\omega, k) \quad (88)$$

where  $f_u$  is the ultimate strength of the selected material,  $A$  is the cross-sectional area and  $W$  is the elastic section modulus. The functions  $g(\omega, k)$  and  $h(\omega, k)$  read as follows:

|   |   |   |   |
|---|---|---|---|
|  |  |  |  |
| $\Psi = 0.25$   | $\Psi = 0.31$   | $\Psi = 0.55$   | $\Psi = 0.71$   |

**Table 22:** Shape factor for circular hollow cross-sections.

$$g(\omega, k) = 1 - 2k^2 \sin^2 \omega \quad (89a)$$

$$h(\omega, k) = \frac{2}{\pi} k \cos \omega \quad (89b)$$

We introduce the parameter  $\Psi$  as the shape factor of the cross-section: a dimensionless value that characterises the cross-sectional shape and points out the relationship between the moment of inertia and the cross-sectional area of the active member:

$$\Psi = \frac{I}{A r^2} \quad (90)$$

where  $r$  is the distance from the neutral axis to the outermost fibre. Table 22 provides shape factors for typical cross-sections used in the design of bending-active structures. The shape factor for rectangular cross-sections is equal to  $\Psi = 0.33$  regardless of the proportion between height and width. For circular solid cross-sections, the shape factor is equal to  $\Psi = 0.25$ . Shape factors for circular hollow cross-sections depend on the thickness of the cross-section; the thinner the thickness, the higher the shape factor. Lienhard [64] points out an optimal ratio  $D_e/D_i = 2$  (which is equivalent to a shape factor  $\Psi$  of 0.31) for circular hollow cross-sections, where the stiffness is close to the maximum value and the cross-sectional area is minimised, getting light members easy to manipulate during construction. In addition, the use of a very thin wall increases the risk of local buckling under the effect of external point-loads. Therefore, the most appropriate cross-sectional shape will be the one that avoids local phenomena as crushing or local buckling.

The parameter  $\bar{\lambda}$  is used to characterise the slenderness of the rod. It takes into account: the length of a semi-wave of elastica; the shape of the cross-section and the mechanical properties of the material

$$\bar{\lambda} = \frac{l}{\pi} \sqrt{\frac{A}{I}} \sqrt{\frac{f_u}{E}} \quad (91)$$

This interpretation is inherited from the definition of mechanical slenderness stated in the Eurocode 3 (see equation (6.5) in [42]). Using this definition of slenderness, the utilisation ratio (88) can be rearranged as follows:

$$\left(\frac{l}{l_c}\right)^2 \frac{1}{\bar{\lambda}^2} g(\omega, k) + \frac{l}{l_c} \sqrt{\frac{E}{f_u}} \frac{\pi}{\sqrt{\Psi}} \frac{1}{\bar{\lambda}} h(\omega, k) \quad (92)$$

As introduced in the previous chapter (section 4.2), the quotient  $l/l_c$  can be stated in terms of the parameter  $k$  by means of the non-dimensional arc-length parameter

$\zeta(\omega, k)$ . Concerning the problem of the inflexional elastica, the length between inflexions is obtained when  $\omega = \frac{\pi}{2}$ , thereby  $\zeta(\frac{\pi}{2}, k) = \frac{2}{\pi}K(k)$

$$\frac{4}{\pi^2} K(k)^2 \frac{1}{\bar{\lambda}^2} g(\omega, k) + 2K(k) \sqrt{\frac{E}{f_u}} \frac{1}{\sqrt{\Psi}} \frac{1}{\bar{\lambda}} h(\omega, k) \quad (93)$$

This expression provides the utilisation ratio of any desired cross-section (defined by  $\omega$ ) in terms of the slenderness, the material properties and the shape of the cross-section. The non-dimensional expression of the utilisation ratio of the cross-section located at midspan –where higher stresses are expected– is obtained by setting  $\omega = 0$ :

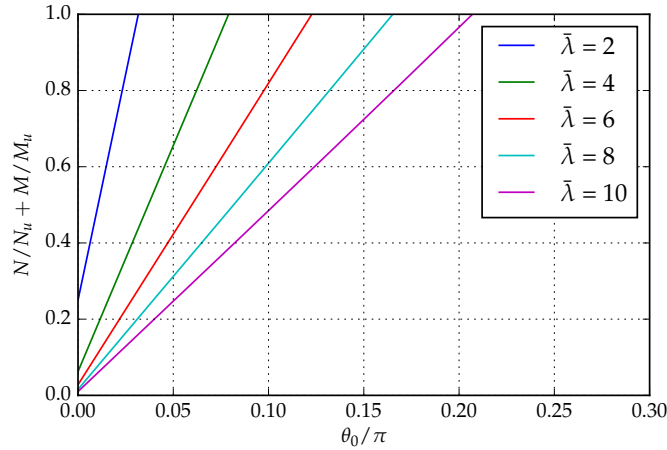
$$\frac{4}{\pi^2} K(k)^2 \frac{1}{\bar{\lambda}^2} + \frac{4k}{\pi} K(k) \sqrt{\frac{E}{f_u}} \frac{1}{\sqrt{\Psi}} \frac{1}{\bar{\lambda}} \quad (94)$$

Additionally, a maximum allowable stress can be introduced to limit normal stresses under the form-finding stage. It is estimated that limiting the utilisation ratio after activation to 30 % avoids further problems caused by long-term dynamic loading

$$\frac{4}{\pi^2} K(k)^2 \frac{1}{\bar{\lambda}^2} + \frac{4k}{\pi} K(k) \sqrt{\frac{E}{f_u}} \frac{1}{\sqrt{\Psi}} \frac{1}{\bar{\lambda}} \leq 0.3 \quad (95)$$

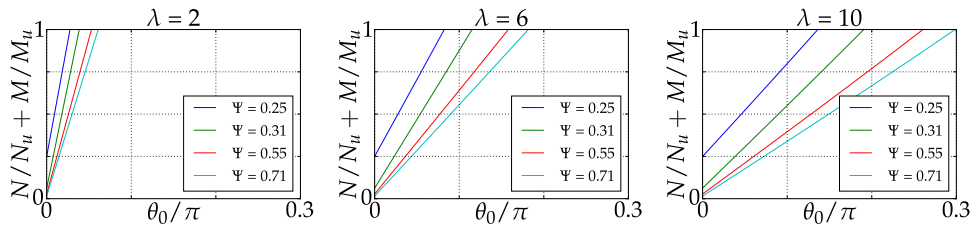
For example, equation (95) allows to select the minimum slenderness of the flexural member compatible with a prescribed stress level of 30 % by choosing: the material ( $E, f_u$ ), the cross-sectional shape factor ( $\Psi$ ) and the elastica shape ( $k$ ).

Figure 38 depicts the utilisation ratio for the particular case of a elastica semi-wave with rectangular cross-section with a shape factor  $\Psi = 0.33$ ;  $E = 30$  GPa and  $f_u = 400$  MPa, in terms of the angle of the tangent to the elastica at the inflexion  $\theta_0$  and the rod slenderness. It can be seen that low values of the rod slenderness lead to higher utilisation ratios.



**Figure 38:** Utilisation ratio of elastica semi-waves with rectangular cross-section  $\Psi = 0.33$ , angle at the inflexion  $\theta_0$ , material properties  $E = 30$  GPa and  $f_u = 400$  MPa, and different values of rod slenderness  $\bar{\lambda}$ .

Figure 39 shows how the cross-sectional shape  $\Psi$  influences on the utilisation ratio of elastica semi-waves, for the same material properties chosen before and for different values of the rod slenderness. According to the diagrams, high shape factors are more advantageous for keeping self-stresses low, however and, as mentioned before, very thin-walled cross-sections may be crushed when applying external loads.



**Figure 39:** Influence of the shape factor  $\Psi$  on the utilisation ratio of elastica semi-waves with rectangular cross-section, angle at the inflexion  $\theta_0$  and different values of rod slenderness  $\bar{\lambda}$ .

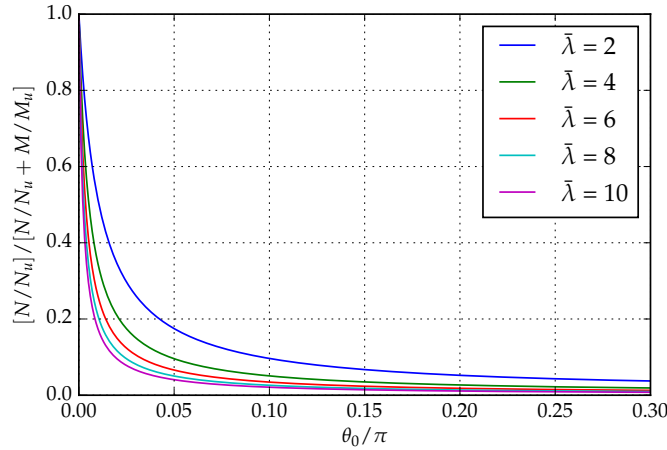


**Figure 40:** Influence of the term relative to axial forces on the utilisation ratio of elastica semi-waves with rectangular cross-section, angle at the inflexion  $\theta_0$  and different values of rod slenderness  $\bar{\lambda}$ .

Figure 40 shows the relative weight of the effect of axial forces on the utilisation ratio for different rod slenderness. For low values of the cross-section rotation at the inflexion, the effect of axial forces is the most limiting. However, as the curvature of the rod increases, stresses produced by bending moments play a more prominent part. As expected, low values of rod slenderness lead to higher utilisation ratios due to axial forces.

Assuming that the bent rod supports the deck of a footbridge, the maximum gradient of the deck is restricted to 10% due to functional requirements, which approximately matches with an angle at the inflexion  $\theta_0 = 0.1$ . Therefore, the effect of axial forces is low but cannot be fully neglected in the analysis.

The relationship between the ultimate strength  $f_u$  and the Young's modulus  $E$  has been widely used to measure how adequate a material is for bending-active structures.

Figure 41 shows the influence of different ratios  $f_u/E$  on the utilisation ratio of elastica semi-waves, with rectangular cross-section and for different values of rod slenderness.

Ashby [6] represented in form of a diagram this relationship for different materials; he gathered them by material classes and introduced guidelines to define design regions for certain applications. According to previous works by Lienhard [64] and La Magna [53], suitable materials for bending-active structures have a ratio  $f_u/E > 2.5$  (with  $f_u$  in MPa and  $E$  in GPa). This requirement is fulfilled by certain types of timber and GFRPs, having the latter ones a ratio  $f_u/E > 10$ . As reflected in the diagrams, the use of materials with a high ratio  $f_u/E$  allows to keep activation stresses low.

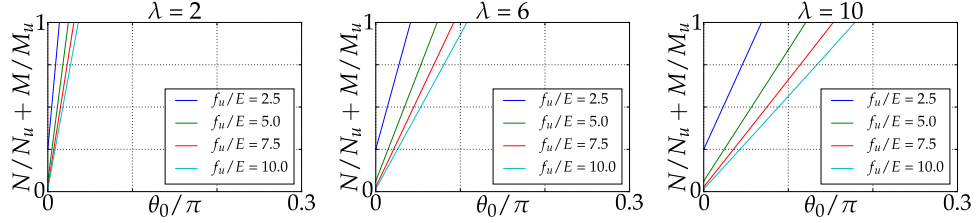


**Figure 41:** Influence of the ratio  $f_u/E$  on the utilisation ratio of elastica semi-waves with rectangular cross-section, angle at the inflexion  $\theta_0$  and different values of rod slenderness  $\bar{\lambda}$ .

### 5.3 SHAPE OF THE ROD BETWEEN DEVIATORS AFTER ACTIVATION

The observation that a rod segment between deviators can be modelled as a segment of elastica is one of the keys of this PhD thesis. It enables the use of closed-form expressions (see equations from 92 to 95) to evaluate the stress level at the tensioning stage, and allows to measure how the form-finding parameters influence on the structural configuration. This observation has been already applied in Chapter 4, where suitable solutions for bending-active braced arches have been form-found by means of an analytical procedure based on the exact solution of the elastica and whose assumptions are: non-extensibility, non-shear deformability and the self-weight is neglected. The first restriction may be adopted without loss of generality for the form-finding problem since the extensional deformations can be neglected compared to the deformations produced by the bending moment. The non-deformability under shear is a physical consequence of the high slenderness of the rod required for this kind of elements. This section aims to show by means of an example that the observation that a rod segment behaves as an elastica segment is sufficiently accurate also when considering these deformations (neglecting the self-weight). For this purpose, the concept of static invariants of a non-linear bent rod will be used: Kirchhoff and Love noted that the equations of in-plane equilibrium of an initially straight, non-extensible and non-shear-deformable rod subject only to forces and/or moments at the end sections are analogue to the equation of movement of a planar pendulum with no restriction on the amplitude of the oscillation. This fact is known as Kirchhoff's kinetic analogy [67]. The corresponding analogues for the inflexional elastica expressed in terms of section forces are:

$$\frac{M^2}{2EI} + N = \mathcal{H} \text{ (constant)} \quad N^2 + V^2 = P^2 \text{ (constant)} \quad (96)$$

where  $\mathcal{H}$  is related with the potential energy density,  $P$  is the compressive force and  $M$ ,  $N$  and  $V$  are the section forces in the rod.

On the basis of the Kirchhoff's kinetic analogy and using a self-stressed configuration, it is possible to show that the invariants predicted by the Kirchhoff's kinetic analogy are kept for a segment of rod between deviators. In the following example, the static invariants along the bent rod of a tied arch are calculated, using the internal forces resulting from a finite element simulation of the activation process. (Note that the FE beam model considers shearing and extensional deformations.) Then, it is shown that the magnitudes  $\mathcal{H}$  and  $P$  are practically equal to the invariants predicted by Kirchhoff-Love's theory.

Figures 42, 43 and 44 show the section forces ( $N$ ,  $M$ ,  $V$ ) obtained with FE model. Bending stiffness of the rod equals  $EI = 23.72$  kN m and the force in cables is equal to  $T = 50$  kN. Table 23 shows the values corresponding to the section forces and invariants at different nodes of the rod segment A-E. As can be seen, static invariants remain practically constant along the rod segment (percent errors are below 0.5%). This error can be attributed to the fact that the software calculation model takes into account axial and shearing deformation as opposed to the elastica theory. Furthermore, this example demonstrates that for the form-finding of this type of structures it is feasible to consider that the rod segments between deviators are shaped like segments of elasticas.

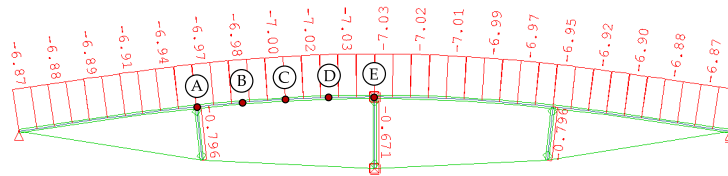


Figure 42: Axial forces  $N$  due to activation process.

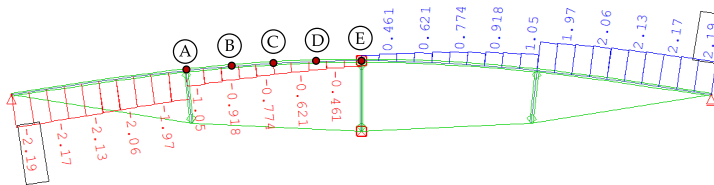


Figure 43: Shear forces  $V$  due to activation process.

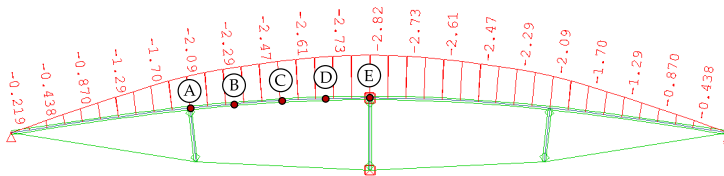


Figure 44: Bending moments  $M$  due to activation process.

|   | N [kN] | V [kN] | M [kNm] | $\mathcal{H}$ [kN] | P [kN] |
|---|--------|--------|---------|--------------------|--------|
| A | -6.97  | 1.05   | 2.09    | -6.88              | 49.68  |
| B | -7.03  | 0.98   | 2.29    | -6.87              | 49.68  |
| C | -7.03  | 0.91   | 2.47    | -6.87              | 49.84  |
| D | -7.02  | 0.77   | 2.73    | -6.87              | 50.2   |
| E | -7.03  | 0.69   | 2.82    | -6.86              | 49.91  |

**Table 23:** Section forces and static invariants of the rod segment A-E.

## 5.4 NUMERICAL TESTS ON BENDING-ACTIVE TIED ARCHES WITH THREE DEVIATORS

This section shows a set of simulations for bending-active tied arches with specific dimensions of members and materials properties. This study aims to: (a) provide examples of the results given in Chapter 4; (b) provide examples of the scalability of the solution and (c) find patterns of relationship between shape and the structural performance of this kind of structures under the load models posed by the Eurocode for footbridges. Simulations are carried out using the non-linear FE software SOFiSTiK.

To limit the number of cases and the complexity of the study, it focuses on symmetric structures with three equally spaced perpendicular deviators which remain perpendicular to the rod. The following common data have been considered: the upper rod is 4 m long continuous member with circular hollow cross-section with thickness equal to 10% of the radius; the deviator lengths are:  $h_q = 0.3$  m at quarters and  $h_m = 0.4$  m at midspan. The ratio between deviator lengths  $h_q/h_m = 0.75$  has been selected after carrying out a parametric study; this ratio provides practically equal axial forces in the deviators after activation and lower deflection under a frequent service load [17].

GFRP –material properties of GFRP are  $E = 30$  GPa,  $f_u = 500$  MPa– has been chosen as a material for the rod. Cables are not continuous; therefore, cable forces can be different in each cable segment. Steel is used for cables; the material properties of the selected cables are:  $E_s = 110$  GPa,  $f_{u_s} = 1570$  MPa (Fig. 45).

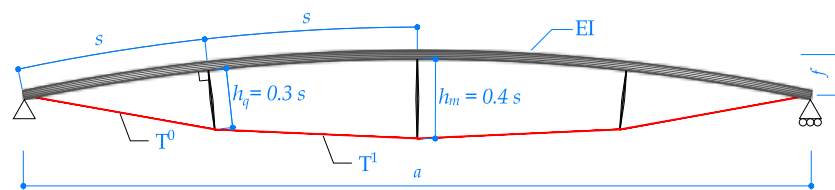


**Figure 45:** Definition of the input parameters.

|            | 1     | 2     | 3      | 4      | 5      | 6      |
|------------|-------|-------|--------|--------|--------|--------|
| $T^0$ [kN] | 2.475 | 7.211 | 11.678 | 15.892 | 19.890 | 23.629 |
| $T^1/T^0$  | 0.967 | 0.977 | 0.988  | 1.000  | 1.012  | 1.027  |
| $a$ [m]    | 3.996 | 3.975 | 3.935  | 3.875  | 3.798  | 3.703  |
| $f/a$      | 0.016 | 0.048 | 0.080  | 0.113  | 0.146  | 0.1811 |

**Table 24:** Values of activation forces and resulting geometric ratios for the sequence of bending-active tied arches (1-6) shown in Fig. 46. The definition of the parameters can be found in Fig. 45.

### 5.4.1 Relationship between shape and activation forces

Six different configurations for a bending-active tied arch with three equally spaced and perpendicular deviators are generated. The cross-section of the upper rod is a circular hollow cross-section with  $EI = 23.72 \text{ kN m}^2$ . Each self-stressed configuration is obtained introducing a force  $T^0$  in the outer cable; perpendicularity between rod and deviators is achieved selecting the corresponding force  $T^1$ . In this simulation, the force  $T^1$  is obtained by trial and error until the condition of perpendicularity between rod and deviators is achieved<sup>1</sup>. Table 24 shows the values of activation forces and the obtained geometric ratios for each structure (Fig. 46).

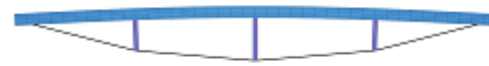
Figure 47 shows the relation between the non-dimensional shape ratio  $f/a$  and the activation force ratio in cables  $T^1/T^0$ . Because of the scalability of elastica solutions, these results can be generalised for flexible members of any length and stiffness, as long as deviators are equally spaced and perpendicular to the rod, where the length of central deviator equals 10% of the length of the rod and the length of lateral deviators equals 75% of the central deviator.

Using the Figure 47 and the results in Table 24, the configuration associated to a desired shape and size can be easily determined. For example, a 10 m span and 1.5 m rise arch ( $f/a = 0.15$ ), interpolating in Table 24, the force ratio  $T^1/T^0 = 1.014$ . For this  $f/a$  ratio, in the reference structure used in the simulations and previously defined in the beginning of the section,  $a = 3.770 \text{ m}$  and  $T^0 = 20.35 \text{ kN}$ . The scaling factor for the desired structure will be  $10/3.77 = 2.65$ ; therefore, applying the scale factor stated in section 4.2,  $EI/T^0$  should be  $2.65^2 = 7.0225$  times larger than in the reference structure. This can be done with a  $2.65 \cdot 4 = 10.6 \text{ m}$  long rod, using a stronger cross-section, or decreasing the activation force, or a combination of both.

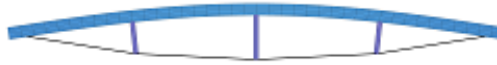
### 5.4.2 Stress levels in the rod after activation

The maximum normal stress (in absolute value) acting on the midspan cross-section of the rod after activation has been evaluated for 20 values of rod slenderness  $\bar{\lambda} = \frac{s}{\pi} \sqrt{\frac{A}{I}} \sqrt{\frac{f_u}{E}}$  (from  $\bar{\lambda} = 0.2$  to  $\bar{\lambda} = 2.5$ ) and 40 values of the rise-to-span ratio (from  $f/a = 0.01$  to  $f/a = 0.2$ ), with  $s = 1 \text{ m}$  (the length of the rod segment between deviators).

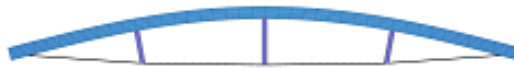
<sup>1</sup> Further details about these relationships can be found in Chapter 4.



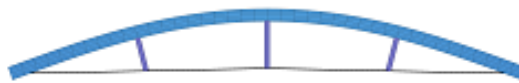
$$(1) T^0 = 2.475 \text{ kN}$$



$$(2) T^0 = 7.211 \text{ kN}$$



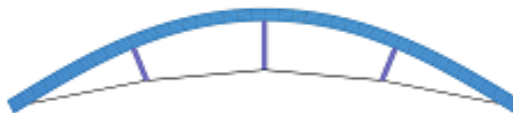
$$(3) T^0 = 11.678 \text{ kN}$$



$$(4) T^0 = 15.892 \text{ kN}$$



$$(5) T^0 = 19.890 \text{ kN}$$



$$(6) T^0 = 23.629 \text{ kN}$$

**Figure 46:** Different configurations for bending-active tied arches with three equally spaced deviators.

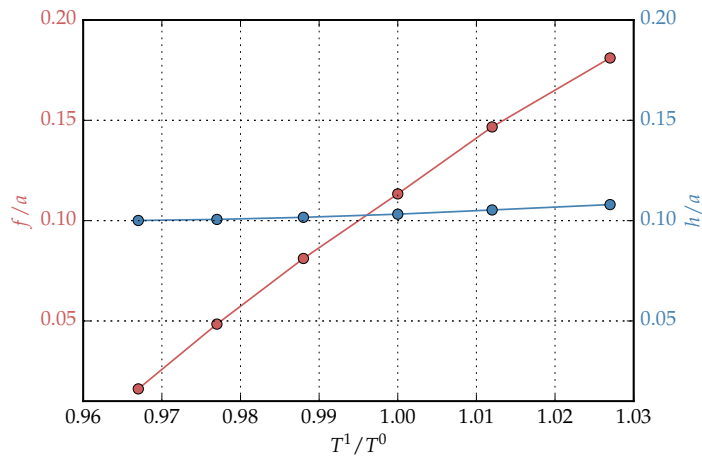


**Figure 47:** Relation between activation force ratios and non-dimensional shape ratios for a bending-active braced arch with three deviators equally spaced and perpendicular to the rod, where the length of central deviator equals 10% of the length of the rod and the length of lateral deviators equals 75% of the central deviator.

The evaluation of the stresses takes into account the axial force and the bending moment produced at midspan, where the curvature reaches its maximum and therefore the bending moment too. Figure 48 shows the curves corresponding to several ratio of stress-to-ultimate-strength that have been elaborated using the stress values provided by the simulations. Once the shape and size of the structure have been defined, the diagram allows to select the minimum slenderness of the flexural member compatible with a prescribed stress level.

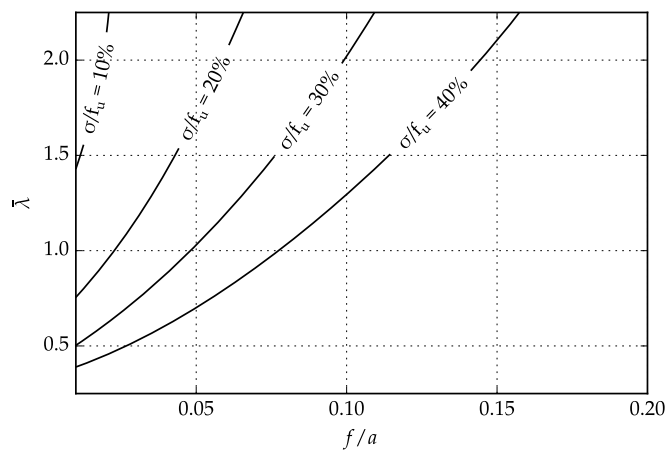


**Figure 48:** Stress ratio levels after activation in terms of rod slenderness and rise-to-span for a bending-active braced arch with three deviators equally spaced and perpendicular to the rod, where the length of central deviator equals 10% of the length of the rod and the length of lateral deviators equals 75% of the central deviator.

### 5.4.3 Structural performance of cables

The selection of the activating cables is crucial in the behaviour of the whole structure. Cables must be carefully designed since oversized cross-sections lead to insufficient cable stresses after the activation stage and undersized cross-sections may result in overall excessive flexibility.

The size of the cable is selected in terms of slenderness. The following definition of cable slenderness is introduced:

$$\bar{\lambda}_c = \frac{s}{d} \sqrt{\frac{f_{u_s}}{E_s}} \quad (97)$$

where  $s$  keeps being the length of the rod segment between deviators and  $d$  the external equivalent diameter of the cable. Among different commercial typologies of steel cable, a wire rope 7x19+0 is chosen: 6 individual strands made up of 19 steel wires wrapped around a core made up of the same strand. Although other wire rope typologies are possible.

To evaluate the structural response of the rod and cables in order to satisfy the design limit states, the loading value for footbridges defined by the Eurocode [41] is used. For the evaluation of the serviceability limit state, a distributed load corresponding to 40% of 5 kN/m<sup>2</sup> has been applied (frequent value of the service load). The loading pattern consists in a uniform load on a width that we choose to be 10% of the developed length of the rod (Fig. 49).

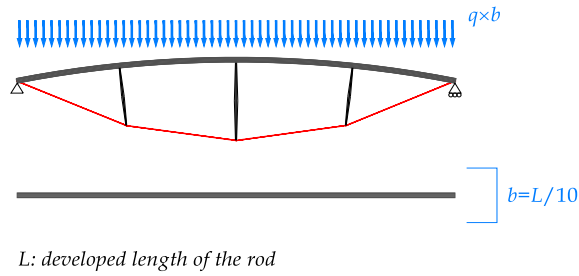


**Figure 49:** Loading model.

Two series of numerical experiments are carried out: in the first one the cable has been selected so that its slenderness be 15 times the rod slenderness; in the second, the cable slenderness is 5 times the rod slenderness. Within each set, stresses in the rod and cables have been evaluated for 20 values of rod slenderness (from  $\bar{\lambda} = 0.2$  to  $\bar{\lambda} = 2.5$ ) and 40 values of the rise-to-span ratio (from  $f/a = 0.01$  to  $f/a = 0.2$ ). Using the cable-rod slenderness ratio  $\bar{\lambda}_c/\bar{\lambda}$  as a parameter to define the size of the cable makes it possible to avoid configurations with oversized or undersized diameters with respect to the size of the rod. For example, Fig. 50 shows two configurations with the same rod slenderness value  $\bar{\lambda} = 1.5$  but with different cable-rod slenderness ratios  $\bar{\lambda}_c/\bar{\lambda}$ , which correspond with the lower and upper bounds 5 and 15 respectively.



**Figure 50:** Configurations with the same rod slenderness  $\bar{\lambda} = 1.5$  and different cable-rod slenderness ratios: a)  $\bar{\lambda}_c/\bar{\lambda} = 5$  and b)  $\bar{\lambda}_c/\bar{\lambda} = 15$ .

Results have been elaborated and summarised in Figure 51. It shows the region of the slenderness-shape diagram where for a selected rise-to-span ratio, the diagram allows to choose the cable-rod slenderness ratio compatible to reach at least 10% of the maximum allowable stress in cables after activation –in order to avoid slack cables– and at most 70% because of service loads. As can be seen, the choice of the cable-rod slenderness ratio restricts the choice of the rod slenderness for a given rise-to-span ratio: higher cable-rod slenderness ratios allow to select large slenderness rods, which may imply low global stiffness, in contrast, lower cable-rod slenderness ratios lead to oversized rod cross-sections, that are incompatible with keeping activation stresses low.

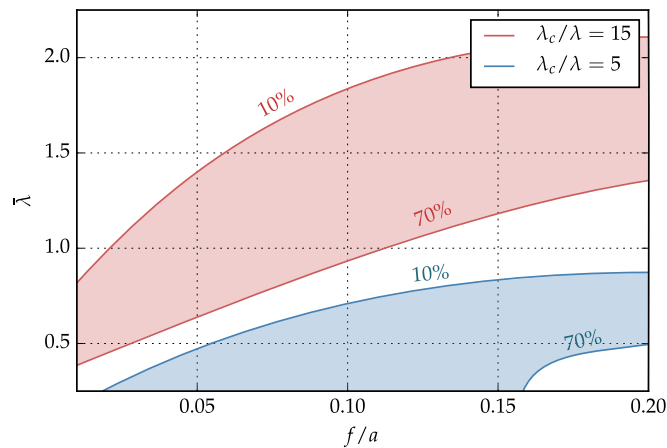


**Figure 51:** Region where stresses in cables are in the interval between 10% and 70% of the maximum allowable stress.

#### 5.4.4 Performance for serviceability limit state (SLS)

For checking the vertical displacement serviceability limit state, midspan deflections have been evaluated using the same previous set of simulations. Results are summarised in Figure 52. Using the diagram, for a selected rod slenderness, the cable can be chosen to achieve a threshold value of deflection. As expected, higher values of rod slenderness lead to larger deflections for a given cable-rod slenderness ratio.

For example, setting a rise-to-span ratio equals  $f/a = 0.10$  and a threshold value for the deflection equal to  $L/500$  –where  $L$  is the developed length of the rod–, two configurations are exemplified, each one corresponding to one of the studied cable-to-rod slenderness ratios: a) a rod slenderness  $\bar{\lambda} = 2$  with a cable slenderness  $\bar{\lambda}_c = 10$  or b) a rod slenderness  $\bar{\lambda} = 1.15$  with a cable slenderness  $\bar{\lambda}_c = 17.25$ . However, solution a) is incompatible with a proper level of stresses in cables (Fig. 52).

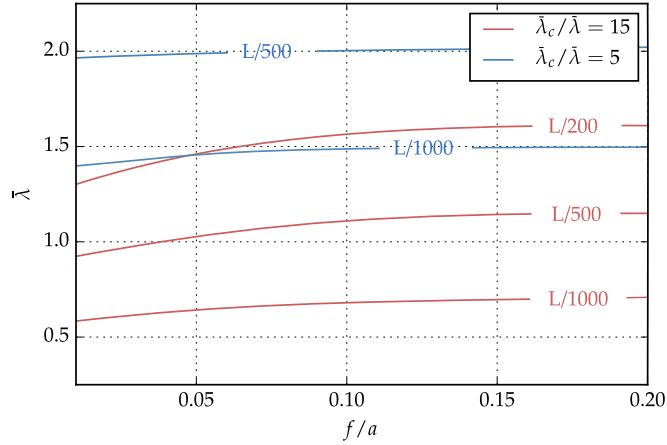


**Figure 52:** Dimensionless deflections from  $L/200$  to  $L/1000$  for different cable-rod slenderness ratios and a given load in terms of slenderness and shape.

#### 5.4.5 Performance for ultimate limit state (ULS)

A similar study has been carried out to assess the ultimate limit states, using the same set of previous structural proportions and cross-section dimensions. To obtain the design load value, the characteristic load value defined by the Eurocode ( $5 \text{ kN/m}^2$ ) is multiplied by the partial factor for actions  $\gamma = 1.35$ . The self-weight is not considered in the simulations aiming at simplifying the analysis by isolating the effect of external loads. Normal forces and bending moments in the rod have been checked, performing a non-linear analysis of the structural model.

Figure 53 shows the region of the slenderness-shape diagram where according to the Eurocode 3 the utilisation ratio is less than 1, for different configurations and a given design load. The shape of the graph is understood as follows: for more slender members the admissible region is reduced by the active member being prone to instability. Low values of the slenderness mean that activation is consuming a large part of the strength, and therefore the admissible region becomes also more limited. The larger values of the rise-to-span ratio correspond to a slenderness of 1.6.

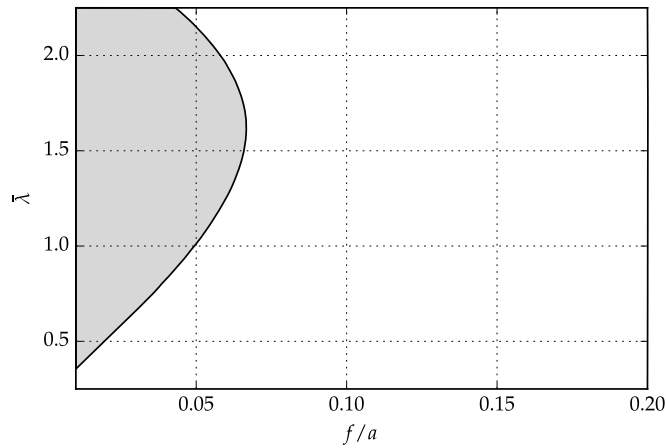


**Figure 53:** Region where the utilisation ratio in the rod is less than 1 for the ultimate limit state.

## 5.5 EXAMPLE

This section shows an example of how the configuration associated to a desired shape and size can be easily determined using the results presented in the previous section.

The design of the bending-active tied arch is based on the following requirements: bending-active rods are designed as 10 m long continuous GFRP members with thin-walled circular hollow cross-section, the height at midspan should be close to 10% of the rod length ( $h_m = 1$  m), the rise-to-span ratio is restricted to 5%, the maximum deflection for frequent loading must be lower than  $L/500$  and the structure has to bear a service load of  $5 \text{ kN/m}^2$ . The mechanical properties of GFRP rod and steel cables correspond to the same setup as in section 5.4.

As shown in Figure 54, for the selected rise-to-span ratio and choosing the cable slenderness as 15 times the rod slenderness, the maximum rod slenderness should be in the range of 1. Nonetheless, multiple solutions are possible; any point within the intersecting region (dark red) represents a feasible configuration. It is worth noting that for lower cable-rod slenderness ratios the structure becomes stiffer, but the stress level in the cables restricts considerably the range of solutions; Figure 54 also shows the case where selecting a low value for the cable-rod slenderness ratio ( $\bar{\lambda}_c/\bar{\lambda} = 5$ ) may lead to incompatible performances of rod and cables.

Using the definition of slenderness (Eq. 91), the target configuration is achieved using a circular hollow cross-section with an outer diameter of 190 mm and a thickness of 9.5 mm. Keeping the established structural proportions, the resulting steel cable is a wire rope 7x19+0 with a nominal diameter of 20 mm.

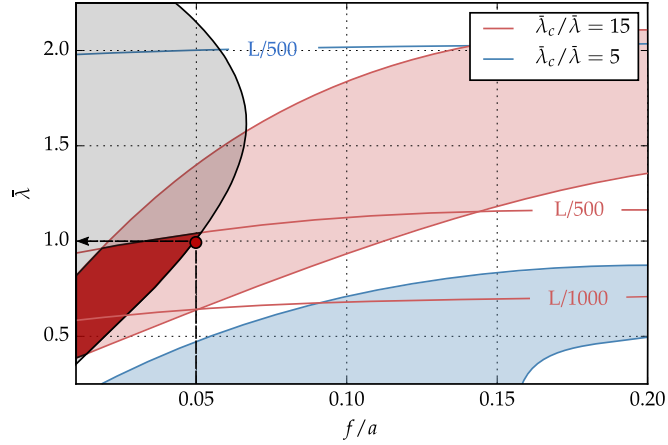


**Figure 54:** Design diagram for the example of the section 5.5.

## 5.6 PROCEDURE TO DESIGN BENDING-ACTIVE TIED ARCHES WITH AN ARBITRARY NUMBER OF DEVIATORS

In this section, a methodology to design bending-active tied arches with  $n$  deviators of any length, based on the results obtained in section 5.4 is shown.

The following procedure is a sequence of orderly steps to reach a feasible solution. As shown in the example in section 5.5, the problem may have multiple solutions and an iterative calculation would be necessary to reach the best of them. The process is as follows:

1. Define the mechanical properties  $E$ ,  $f_u$ , for the rod and cables. Deviators can be initially considered as rigid bodies.
2. Define the length of each segment of the rod  $s_i$ , for  $i \in \{1 \dots n\}$ , and the lengths of deviators  $h_i$ , for  $i \in \{1 \dots n-1\}$
3. Select the cross-sectional shape  $\Psi$  and slenderness  $\bar{\lambda}$  for the rod. This choice can be supported by the diagram 48 in a first step.
4. Select the typology and size of steel cables in terms of relative slenderness with the rod  $\bar{\lambda}_c = k \cdot \bar{\lambda}$ , being  $k$  the multiplying factor. It is suggested that  $k$  ranges from 10 to 20.
5. Obtain the configuration associated to a desired shape  $f/a$  by means of increasing or decreasing the tensioning force  $T^0$  (force in the outer cable). Perpendicularity between rod and deviators can be achieved introducing the corresponding force  $T^1$ .
6. Check stresses in the rod  $\sigma_{FF,R}$  and cables  $\sigma_{FF,C}$  after the activation process. Oversized cables cross-sections can lead to an insufficient stress level (risk of cables becoming slack) at the activation stage and the active member must be slender enough to keep stresses low and limit further problems due to cycling long-term loading. As explained in sections 5.2.1 and 5.4.3, it is suggested that stresses be around 30% of the material strength in the rod and over 10% of the cable strength after activation.

7. Simulate the load models and check the serviceability limit state and the ultimate limit state for the rod and cables. Maximum deflections at midspan  $v_{(L/2)}$  and stresses  $\sigma_{ULS,r}$ ,  $\sigma_{ULS,c}$  must be lower than the threshold value posed by codes.

Figure 55 shows the process outlined in a flow chart.

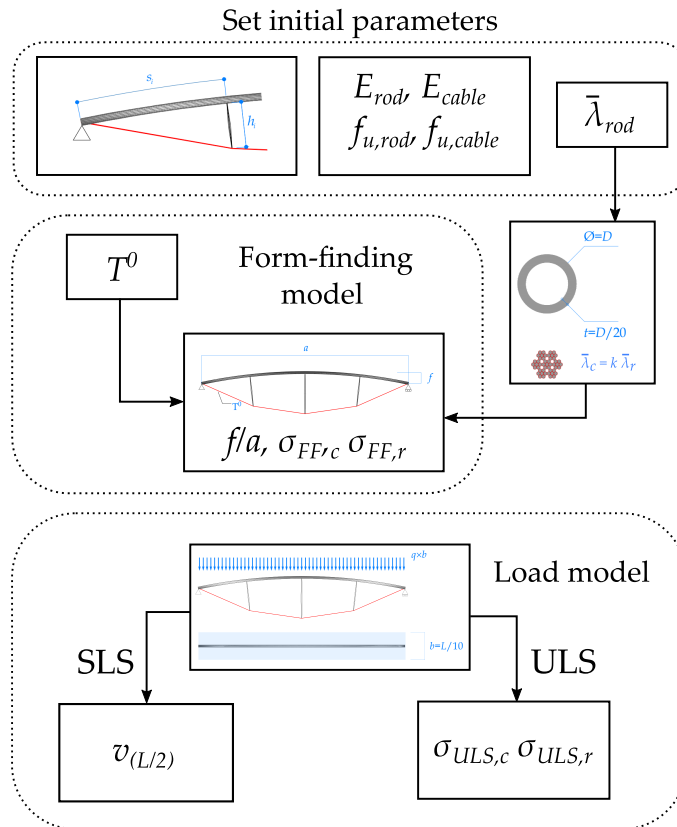


**Figure 55:** Procedure to design a bending-active tied arch with an arbitrary number of deviators.

## 5.7 SUMMARY

The design of bending-active structures is a challenging problem due to the non-linearity of the activation process, the coupling between: cross-section dimensions, structural shape and initial stress state, and the deformability and buckling sensitivity inherent to the resulting lightweight configurations. In this chapter, the activation process and the structural performance under external loads of bending-active tied arches with three perpendicular deviators have been studied.

In section 5.2, the exact solution of the elastica has been used for the evaluation of the self-stress state. Due to the scalability of the solution, the obtained results are applicable to the design of bending-active structures of any size and stiffness for bending-active braced arches. Taking advantage of this idea, in section 5.4 a set of simulations for a three-strut tied arch with perpendicular deviators are carried out. Relationship patterns between shape and activation forces have been obtained in terms of non-dimensional geometric ratios and rod slenderness, which demonstrates and exemplifies the results shown in Chapter 4.

Secondly, the serviceability limit state and the ultimate limit state have been studied separately by means of two series of numerical experiments. Maximum deflections and stresses in the rod and cables have been evaluated and compared to the limitations posed by the Eurocode for footbridges. The results have been elaborated and synthesised to produce non-dimensional diagrams useful for the design of bending-active tied arches with three deviators of any size and shape. The results show that the design space is limited, mainly because the magnitude of the load and limitations for deflections in serviceability limit states posed by codes are very restrictive. Less restrictive limitations would allow for wider design possibilities.

Section 5.5 shows an example that illustrates the way to obtain a feasible configuration compatible to a desired shape and size of a bending-active tied arch with three deviators, for the chosen materials and structural proportions. Finally, a procedure to extend the previous results to tied arches with different number and proportions of deviators has been detailed.

# 6

## DESIGN OF BENDING-ACTIVE TIED ARCHES BY USING A MULTI-OBJECTIVE OPTIMISATION METHOD

” *Engineering is the art of directing the great sources of power in nature for the use and convenience of man.*

– **Thomas Tredgold**  
(Engineer)

This chapter is an adaptation of the published peer-reviewed paper: Bessini, J.; Shepherd, P.; Monleón, S.; Lázaro, C.; (2020) "Design of bending-active tied arches by using a multi-objective optimisation method". *Structures*. Vol. 27, pp. 2319-2328. doi: 10.1016/j.istruc.2020.07.045

### 6.1 INTRODUCTION

The results obtained in the previous chapter for the performance of bending-active tied arches for pedestrian bridge applications show that the region of the design space where solutions comply with the design constraints is fairly limited, due primarily to the magnitude of the design loads and the tight limitations on stress and deflection posed by codes. Solutions are dominated by instability in the active members, minimum stresses in cables after activation and maximum allowable deflections for the serviceability limit state.

In Chapter 5, a series of simulations using specific sizes of members and material properties, for a certain length ratio between deviators were performed. With these results, general non-dimensional relations between activation forces and structural shapes were established in terms of non-dimensional geometric ratios and rod slenderness. Because of the scalability of the solutions, the results obtained from this study are applicable to the design of bending-active tied arches of any size and stiffness. However, these results cannot be extended to other bending-active braced arches with different length ratio between deviators and then, it would be necessary to replicate the numerical experiments for every potential structural configuration. Due to the large number of form-finding parameters, and the restrictive limitations posed by codes, the determination of the best structural configuration is a challenging process.

This chapter aims to build on the work done in the Chapter 5 by presenting a design procedure, that in an automated way, carries out the design process of the structure for every potential configuration. To achieve this, all the form-finding parameters involved in this problem are included as a variable input in the study.

These parameters are: the size and cross-sectional shape of the rod, the diameter of the cables and the deviator lengths at midspan and quarter-span sections. Additionally, a second load pattern with a non-symmetric uniform load on half-span has been considered to better understand the response of the structure under service loads.

For that purpose, a design tool to generate efficient structural configurations for braced bending-active tied arches using multi-objective optimisation strategies is proposed. Initially, a non-linear FE analysis is performed for each plausible configuration and at each generation of the optimisation algorithm. In a second step, a genetic algorithm classifies the solutions and establishes new structural configurations according to best performance. Solutions are evaluated in terms of stresses in the active member and cables, and maximum deflections, as required by design codes for pedestrian bridges. Finally, results are given in terms of non-dimensional parameters, which make them applicable to a wide variety of scales and cross-sectional sizes.

### 6.1.1 Outline of the chapter

The outline of the chapter reads as: In section 6.2 the problem is introduced and the considered variables in the multi-objective optimisation method are detailed. In section 6.3 the genetic algorithm is described and a sensitivity study is carried out to calibrate the method. The results obtained after the optimisation process are shown in section 6.4. In section 6.5 the solution is analysed from a structural point of view.

## 6.2 PROBLEM DESCRIPTION

To develop the proposed method, the topology of the bending-active tied arch remains the same as in the previous Chapter 5 (three equally spaced deviators with a 4 m long upper rod). The design of the deviators is beyond the scope of the present study. They should be defined in a second stage once the shape of the structure and the rod and cables have been obtained. The material properties of the rod and cables are shown in Table 31, where  $E$  is the elastic modulus and  $f_u$  is the ultimate strength of the selected material.

| Element | Material | $E$ (MPa) | $f_u$ (MPa) |
|---------|----------|-----------|-------------|
| Rods    | GFRP     | 30 000    | 400         |
| Cables  | Steel    | 110 000   | 1570        |

**Table 25:** Material properties.

As introduced above, there are five form-finding parameters in this problem: the size and cross-sectional shape of the rod, the diameter of the cables and the deviator lengths at midspan and at quarter-span sections. To populate the data set of the multi-objective optimisation problem, some of these parameters are introduced as non-dimensional variables. In the following, the input variables are detailed:

- The diameter and thickness of the circular hollow cross-section of the rod are given by the selected outer  $D_e$  and inner  $D_i$  diameters. The outer diameter

can vary from  $s/20$  to  $s/8$ , where  $s$  is the length of the rod segment between deviators; the inner radius is given by the ratio  $D_i/D_e$ , which can vary from 0.2 to 0.8. These limitations allow to get light active-members without risk of local buckling or crushing under the effect of external loads.

- The length of the deviator at midspan  $h_m$  can range from  $L/15$  to  $L/5$ , where  $L$  is the developed length of the rod. The length of the deviators at quarter-points  $h_q$  is defined by means of the ratio  $h_q/h_m$ . These geometrical constraints are selected from an aesthetic point of view.
- The diameter of cables  $d$  is determined by the cable-rod slenderness ratio  $\bar{\lambda}_c/\bar{\lambda}$ , using the same strategy as in Chapter 5.

Table 26 summarises the bounds chosen for the form-finding parameters.

| Variable                        | Lower bound | Upper bound |
|---------------------------------|-------------|-------------|
| $h_m$                           | $L/15$      | $L/5$       |
| $h_q/h_m$                       | 0.3         | 1           |
| $D_e$                           | $s/20$      | $s/8$       |
| $D_i/D_e$                       | 0.2         | 0.8         |
| $\bar{\lambda}_c/\bar{\lambda}$ | 5           | 15          |

**Table 26:** Upper and lower bounds for the input variables in the multi-objective optimisation method.

The design of the bending-active tied arch must also meet the functional requirements for footbridges posed by codes. Therefore, the analysis is restricted to arches with a rise-to-span ratio  $f/a$  close to 6%. This value corresponds with the maximum allowable gradient of the deck.

With the aim of obtaining self-stressed configurations with a particular rise-to-span ratio  $f/a$  to populate the data set of the multi-objective optimisation problem, each flat configuration (generated randomly from the values of the Table 26) is simulated for four values of activation forces  $T^0$  given by the relation between the bending stiffness of the rod  $EI$  and four critical lengths  $l_c$ , ranging from  $l_c = 1$  to  $l_c = 4$ , which remain constant for all the experiments. The number of values and their magnitudes have been selected after checking that with this number of shape parameters  $l_c$  and their corresponding activated shapes, at least one of them close to the desired non-dimensional shape ratio  $f/a = 6\%$ . Perpendicularity is achieved introducing the corresponding force  $T^1$ , as explained in Chapter 5. After activation, stresses in the rod are evaluated at midspan using the axial force and bending moment. Stresses in the cables are also quantified. Simulations have been carried out using the non-linear Finite Element (FE) software SOFiSTiK.

The second consideration in the design of bending-active structures is the serviceability limit state. To achieve this a distributed load corresponding to 40% of the 5 kN/m<sup>2</sup> service load is applied according to the loading model for footbridges posed by the Eurocode [41]. Deflections are calculated at midspan ( $D_m$ ) and at quarters ( $D_q$ ) using two loading patterns.

The first is a symmetric uniform load on a width chosen to be 10% of the developed length of the rod (Fig. 56). The second is a non-symmetric uniform load on half-span with the same width (Fig. 57).

For the evaluation of the ultimate limit state, the characteristic load value  $5 \text{ kN/m}^2$  is multiplied by the partial factor for actions  $\gamma = 1.35$  [41].

Normal forces and bending moments are assessed in the rod at the midspan cross-section considering the symmetric loading pattern and performing a FE non-linear analysis.

Due to the lightness of this kind of structures, the effects caused by the self-weight can be neglected in the simulations. This simplifies the analysis and allows to isolate the effect of external loads.

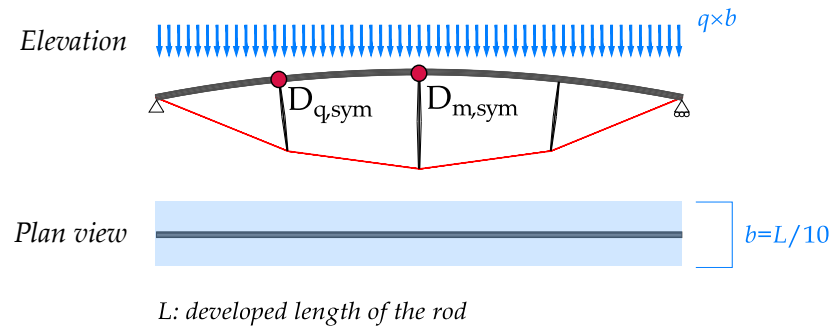


**Figure 56:** Symmetric loading pattern.

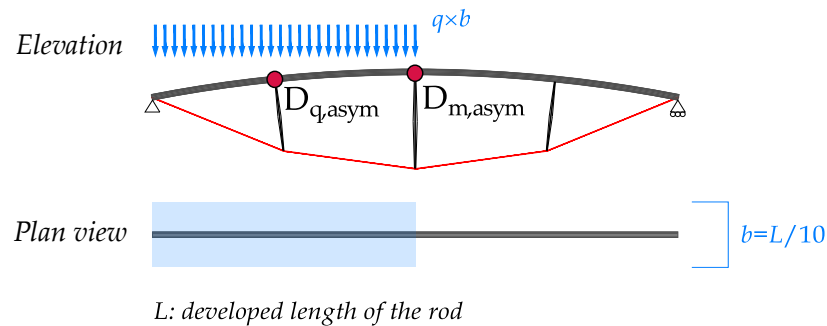


**Figure 57:** Non-symmetric loading pattern.

### 6.3 THE MULTI-OBJECTIVE OPTIMISATION PROBLEM

The computational framework presented in this paper combines two techniques to obtain efficient structural configurations: a non-linear FE analysis and a genetic algorithm. The process starts with the definition of the set of feasible solutions (*population*). Individuals are randomly initialised and composed of five genes that correspond to the form-finding parameters described in Table 26. Secondly, a non-linear FE analysis is performed in each generation for each individual, in order to evaluate the structural response of the tied arch. Finally, the genetic algorithm carries out fitness-based selection and recombination to produce the next generation of suitable structural configurations (Fig. 58).

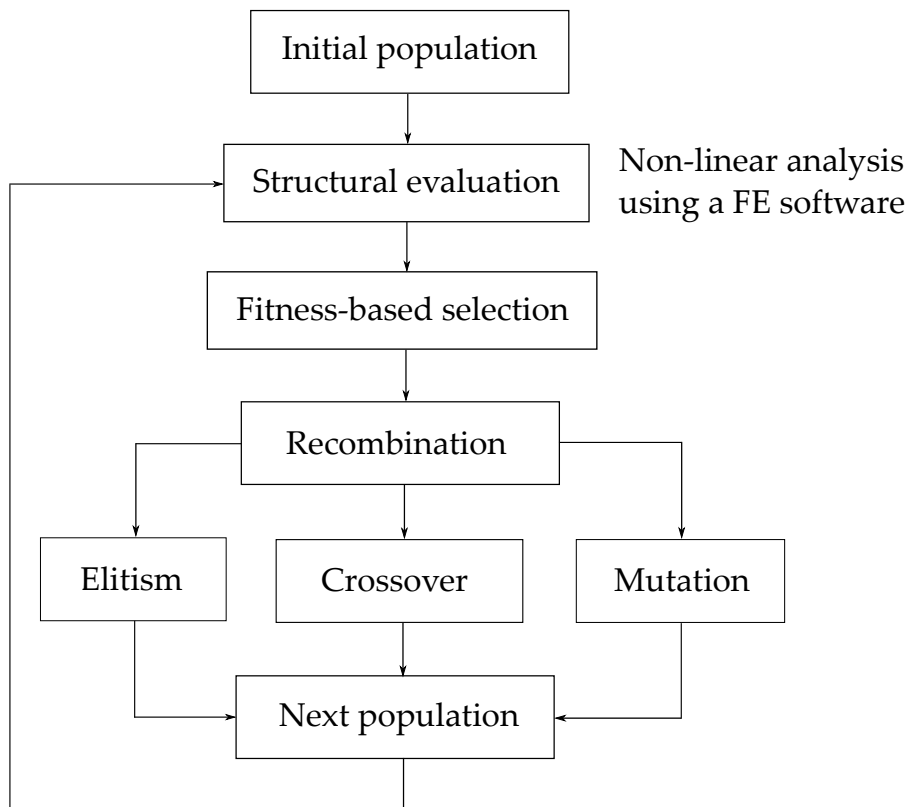


**Figure 58:** Flowchart of the design method.

### 6.3.1 Fitness

In the design of bending-active structures, the selection of member proportions determines the behaviour of the whole structure. Oversized cable cross-sections can lead to insufficient stress at the activation stage, and undersized cross-sections may result in an excessively flexible system. The active member is required to be slender enough to keep stresses low after activation. Moreover, oversized rod cross-sections lead to heavy solutions that are not interesting from an aesthetic point of view. To satisfy these requirements, four fitness objectives (cost functions) are considered in the proposed multi-objective minimisation problem to evaluate each structural configuration. Fitness function depends on: a) the utilisation ratio of the rod for the ultimate limit state  $R_{ULS}$ ; b) the utilisation ratio of cables after activation and for the serviceability limit state  $C_{FF-SLS}$ , where the resulting cable cross-section should be capable of reaching at least 10% of the maximum allowable stress after activation, and at most 70% under service loads; c) the maximum deflection at midspan  $D_m$  and at quarters  $D_q$  for serviceability limit state  $D_{SLS}$ , with the ratio  $L/1200$  as the target according to codes for footbridge applications; and d) the weight of the rod and cables  $W$  to guide the process towards structural configurations that are as light as possible.

The utilisation ratio of the rod has been calculated according to EN 1993-1-1 (see Eurocode 3, Eq. 62.2 [42]). The expression reads as follows:

$$\frac{N}{N_u} + \frac{M}{M_u} \quad (98)$$

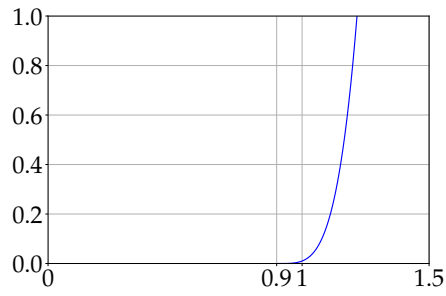
where  $N$  and  $M$  are the axial force and bending moment at the midspan cross-section respectively, produced either by the bending of an initial straight rod during the tensioning process or the application of external design loads;  $N_u$  and  $M_u$  are the design values of the ultimate axial forces and bending moments respectively, without considering buckling reduction factors. For cables, the expression is simplified due to the absence of bending moments:

$$\frac{N}{N_u} \quad (99)$$

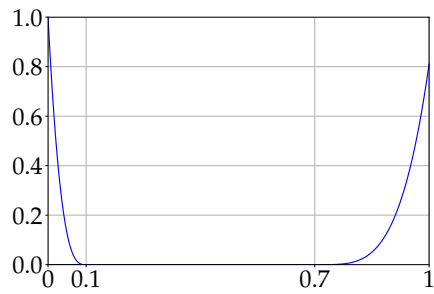
The fitness score of each individual ( $i$ ) and at each generation ( $t$ ) is obtained as the weighted summation of the fitness functions (eq. 100). The weight for each fitness function has been selected according to the relative importance of the variables, defined by the user. The part of the fitness score related to serviceability limit state  $F_c (D_{SLS})$ , has been obtained as the equally weighted summation of the fitness function  $F_c (D_{l,p})$  for each non-dimensional deflection  $D_{l,p}$  considering the different loading patterns (symmetric and non-symmetric) and positions (at midspan and at quarters) (eq.101).

$$\text{Fitness}_i^t = 0.4F_a (R_{ULS}) + 0.1F_b (C_{FF-SLS}) + 0.25F_c (D_{SLS}) + 0.25F_d (W) \quad (100)$$

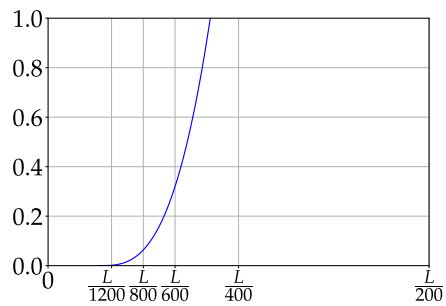
$$F_c (D_{SLS}) = \frac{1}{4}F_{c1} (D_{q,sym}) + \frac{1}{4}F_{c2} (D_{m,sym}) + \frac{1}{4}F_{c3} (D_{q,asym}) + \frac{1}{4}F_{c4} (D_{m,asym}) \quad (101)$$



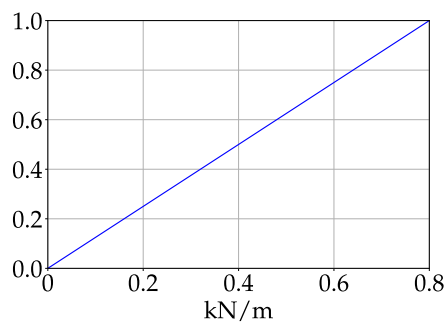
$$(a) F_a \begin{cases} 0, & \text{if } R_{ULLS} \leq 0.9 \\ 100 (R_{ULLS} - 0.9)^4, & \text{if } R_{ULLS} > 0.9 \end{cases}$$



$$(b) F_b \begin{cases} 1000 (0.1 - C_{FF})^3, & \text{if } C_{FF} < 0.1 \\ 0, & \text{if } 0.1 \leq C_{FF} \leq 0.7 \\ 100 (C_{FF} - 0.7)^4, & \text{if } C_{FF} > 0.7 \end{cases}$$



$$(c) F_c \begin{cases} 0, & \text{if } D_{L,p} \leq \frac{L}{1200} \\ 5 \cdot 10^6 \left( D_{L,p} - \frac{L}{1200} \right)^3, & \text{if } D_{L,p} > \frac{L}{1200} \end{cases}$$



$$(d) F_d = 1.25 W \text{ with } W \text{ in kN/m}$$

**Figure 59:** Fitness functions considered in the multi-objective optimisation problem.

### 6.3.2 Selection

The selection component is based on the so-called proportional selection technique [48]. This selection strategy allocates each individual a probability of being selected, proportional to its relative fitness score, which is computed by dividing the fitness of each individual by the sum of all fitness values, normalising to 1. Since the optimisation method is a minimisation problem, we cannot apply this technique directly. Instead we use  $1 - \text{fitness}$ , so that individuals with a lower fitness score will be more likely to be chosen as a parent. Using this technique, the best individuals can be selected multiple times for breeding.

### 6.3.3 Recombination and evolution

Among existing crossover techniques, the one-point crossover has been implemented in this research. Every pair of parents are each cut at a random position (crossover point) and the genes on one side of the crossover point are swapped to generate two new individuals [45]. After recombination, each individual has a 40% probability of mutation (see section 6.3.4). In this case, one of its genes, randomly selected, adopts a new value within the initial predefined bounds. This technique introduces diversity into the population, which prevents the algorithm from becoming trapped in a local minimum [50]. Finally, the successor population is generated using replacement with elitism, where the best individual from the current population is carried over unaltered to the next generation.

The genetic algorithm iterates until it reaches a configuration whose fitness score remains unimproved for at least 100 consecutive iterations.

### 6.3.4 Sensitivity study

To improve the genetic algorithm performance, a sensitivity study has been carried out to determine an efficient set of genetic algorithm parameters. The set of experiments obtain the optimum population size and probability of mutation. It has been considered that all fitness functions are equally weighted and a maximum number of iterations of 300. In Table 27, it can be observed that setting a large population does not lead to a better solution. On the other hand, with small populations, a probability of mutation close to 40% offers the best outcome. In addition, setting small populations is advantageous from the point of view of reducing the computational cost.

| Experiment | Population | Mutation [%] | Fitness <sub>i</sub> <sup>300</sup> |
|------------|------------|--------------|-------------------------------------|
| E1         | 25         | 0            | 0.0200                              |
| E2         | 25         | 30           | 0.0155                              |
| E3         | 25         | 40           | 0.0151                              |
| E4         | 25         | 50           | 0.0156                              |
| E5         | 50         | 40           | 0.0156                              |
| E6         | 100        | 30           | 0.0154                              |
| E7         | 100        | 40           | 0.0155                              |

**Table 27:** Experiments to select the population size and probability of mutation.

## 6.4 RESULTS

Results are given in terms of non-dimensional parameters and shown graphically to better understand the evolution of the form-finding variables through the multi-objective optimisation process. Figure 60 shows the range of genome values for the initial population considered in the problem, which has been randomly defined using a Sobol sequence [91]. This method distributes the points evenly and uniformly. Figure 60 a) depicts the length of the central deviator and the length ratio between deviators; Figure 60 b) provides information about the cross-section of the rod; Figure 60 c) establishes the member ratio between rod and cables. In Figure 61, the population distribution and the results obtained (red points) are shown at iteration number 500, which satisfies the design constraints. Figures 62 and 63 show the evolution of the fitness function and the different evaluated utilisation ratios during the multi-objective optimisation process.

Table 28 shows the form-finding variables obtained at different stages of the multi-objective optimisation process with geometries shown in Figure 64. Tables 29 and 30 show the utilisation ratios of the rod and cables and the maximum span-deflection ratios for the structural solution reached in the optimisation process.

|    | Iter | Fitness | $h_m/s$ | $h_q/h_m$ | $\bar{\lambda}$ | $D_i/D_e$ | $\bar{\lambda}_c$ |
|----|------|---------|---------|-----------|-----------------|-----------|-------------------|
| a) | 1    | 0.0549  | 0.393   | 0.925     | 1.767           | 0.673     | 8.47              |
| b) | 5    | 0.0268  | 0.595   | 0.697     | 2.404           | 0.575     | 8.47              |
| c) | 150  | 0.0149  | 0.448   | 0.697     | 1.887           | 0.701     | 7.28              |
| d) | 500  | 0.0148  | 0.447   | 0.697     | 1.891           | 0.695     | 7.26              |

**Table 28:** Form-finding variables for different configurations.

| After activation |        | ULS    |        |
|------------------|--------|--------|--------|
| Rod              | Cable  | Rod    | Cable  |
| 0.3529           | 0.0771 | 0.9551 | 0.2233 |

**Table 29:** Utilisation ratios of the rod and cables for the solution reached.

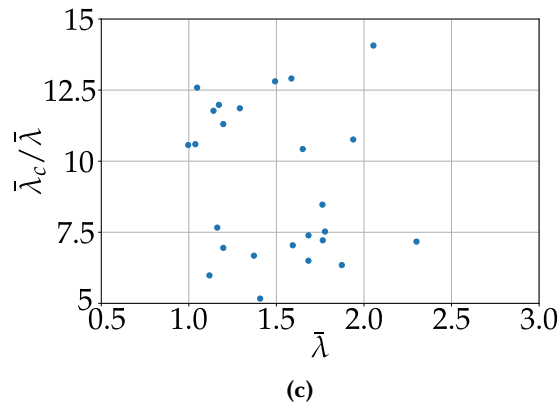
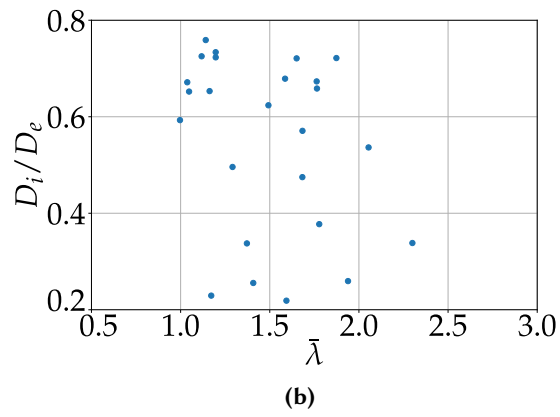
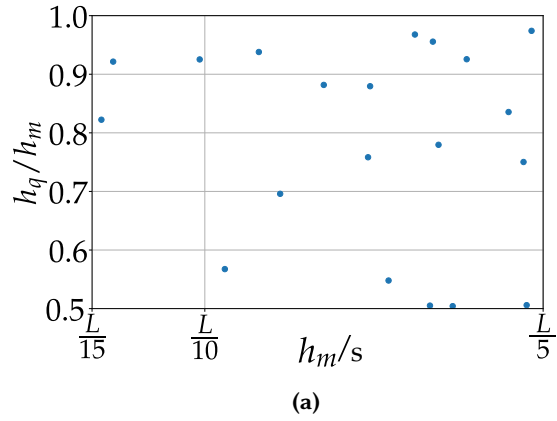


**Figure 60:** Initial population.

| SLS [mm]    |             |              |              |
|-------------|-------------|--------------|--------------|
| $D_{q,sym}$ | $D_{m,sym}$ | $D_{q,asym}$ | $D_{m,asym}$ |
| 2.88        | 3.30        | 0.83         | 2.70         |

**Table 30:** Maximum deflections (in mm) for the solution reached.

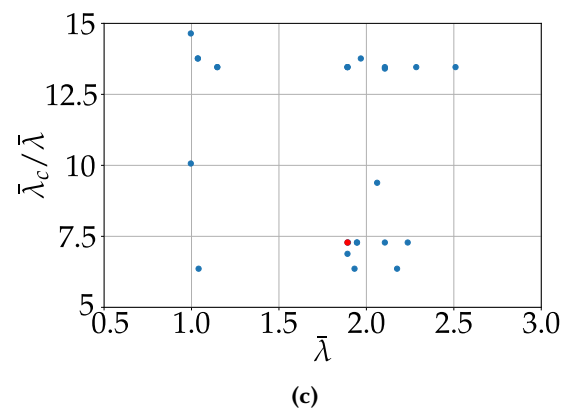
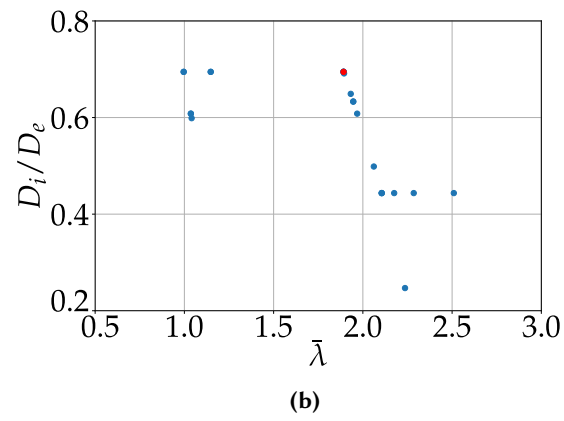
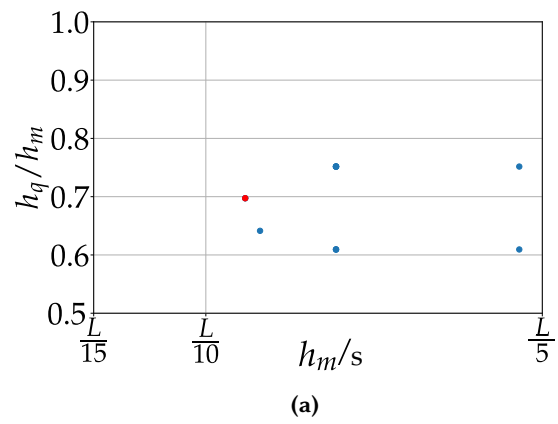


**Figure 61:** Distribution of the population and results (red points) at final iteration.

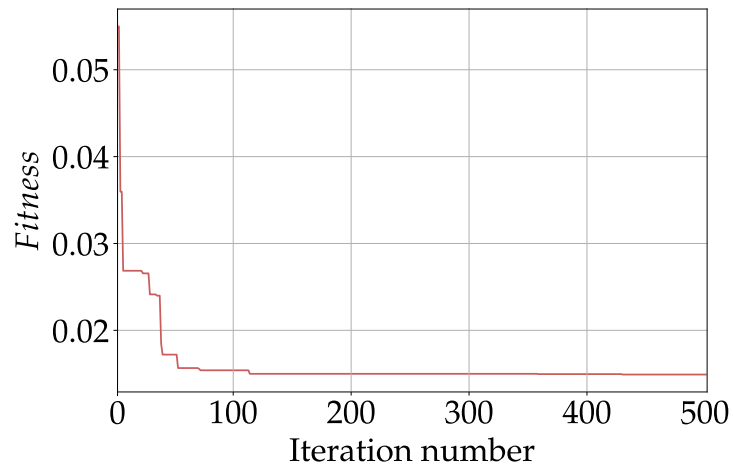


**Figure 62:** Evolution of the fitness function.

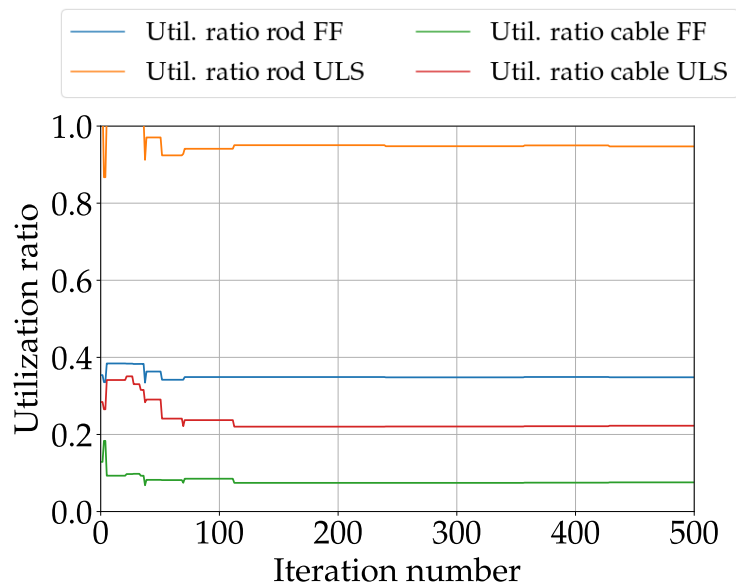


**Figure 63:** Utilisation ratios of the rod and cables after activation (FF) and for the ultimate limit state (ULS).

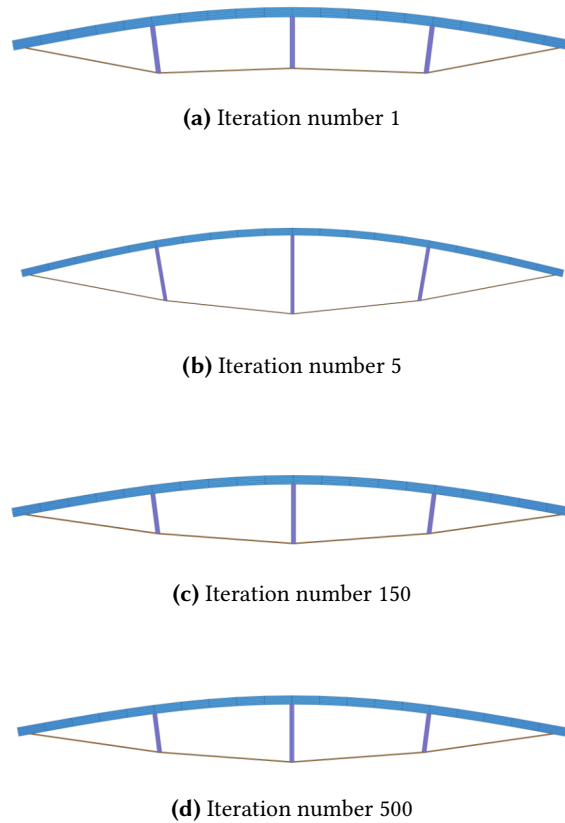


**Figure 64:** Configuration for bending-active tied arches at different iterations.

As can be seen from the results shown in Tables 28, 29 and 30 the genetic algorithm evolves towards efficient solutions characterised by active members with moderate values of slenderness, minimal cross-sections for the ultimate limit state of the structure and cable cross-sections slightly oversized, that provide the required global stiffness to the tied arch, at the expense of a low, but sufficient, cable stress after activation (Fig. 63).

Regarding the cross-sectional shape of the rod, the genetic algorithm tends to converge on solutions with ratios  $D_i/D_e \approx 0.6$ . This value maximises the stiffness and minimises the cross-sectional area, which favors light structural schemes and supports the assumption made in previous work [18] and Chapter 5.

The evaluation of the stress in the flexible member after activation is another important aspect in the design of bending-active structures. High stresses can lead to the emergence of long-term strains due to creep in GFRP materials. Consequently, stresses after activation should be within 30% - 60% of the maximum allowable stress to avoid this phenomenon [34, 64]. In the solution obtained, stresses in the rod after activation are limited to 35% of the allowable stress, which is a moderate and desirable value. For the evaluation of deflections the limitation posed by the Eurocode for footbridges has been considered. The maximum value for deflections must be lower than  $L/1200$ , where  $L$  is the span length. In the solution reached, the active member is 4 m long  $L$  and maximum deflections are shown in Table 30. For each value, the limitation  $L/1200$  is fulfilled.

The outcomes of the experiment are expressed in terms of non-dimensional parameters. As shown in [18], for a given member cross-section, outcomes can be generalised for flexible members of any length and stiffness, as long as: the shape

of the bending-active arch is equivalent. This means that the deviators are equally spaced and perpendicular to the rod; deviator at midspan are 44% of the developed length of the rod; the length of the other two is 70% of the central deviator (Table 28, configuration C) and the relation between external loads remains constant. For example, for the design of a footbridge consisting of a 12 m long continuous active member with a rise-to-span ratio  $f/a$  of 6%, according to the rod slenderness (1.891) and cable slenderness (13.728) obtained in the study, the tied arch can be built using a circular hollow cross-section with an outer diameter of 190 mm and a thickness of 30 mm and a steel cable with a diameter of 26 mm.

## 6.5 STRUCTURAL ANALYSIS AND VERIFICATION

From a structural point of view, it is crucial to understand why the obtained solution is optimal. This section aims to explain why the algorithm tends to this configuration and how the form-finding parameters influence the structural behaviour of the solution. For that purpose, the analysis focuses on the final solution after 500 iterations. In order to better understand the outcomes, the optimal solution is compared with a 'bad' solution (first iteration of the algorithm). In this way, it is possible to appreciate the improvement of the structural solution.

Among the different form-finding parameters, the length of the deviators are the most critical to the behaviour of the whole structure. Comparing the structure with a truss girder, the length of the deviator at midspan defines the height of the beam, which directly influences on the overall stiffness of the system. As expected, higher values of the deviator length at midspan lead to smaller deflections (Figs. 65 and 66).

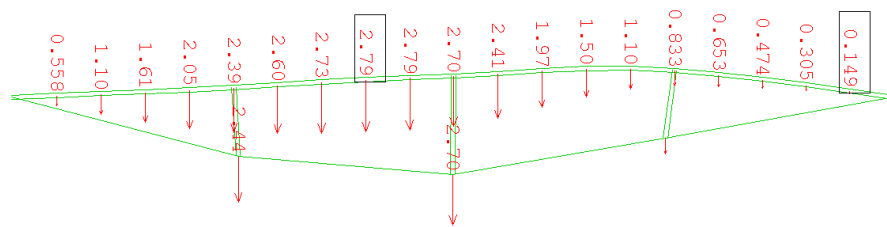


**Figure 65:** Vertical deflections (mm) due to the non-symmetric loading pattern for the serviceability limit state (optimal solution).

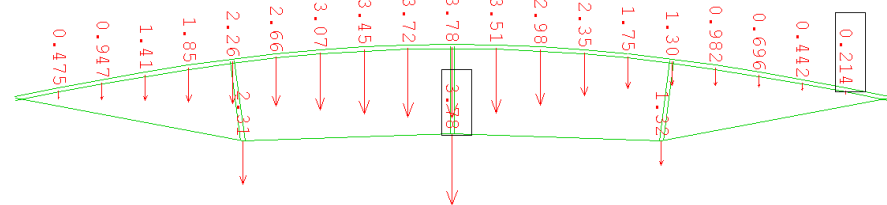


**Figure 66:** Vertical deflections (mm) due to the non-symmetric loading pattern for the serviceability limit state (bad solution).

Another important aspect is the ratio between deviator lengths  $h_q/h_m$ . Figures 67 and 68 show the bending moments in the rod obtained from a FE model at the form-finding stage. As can be seen, for a ratio  $h_q/h_m \approx 0.7$ , the maximum value for the bending moment is located at midspan, where higher curvatures are expected, and decreases gradually until zero at the ends. This behaviour is the expected structural response in elastica-shaped active arches.

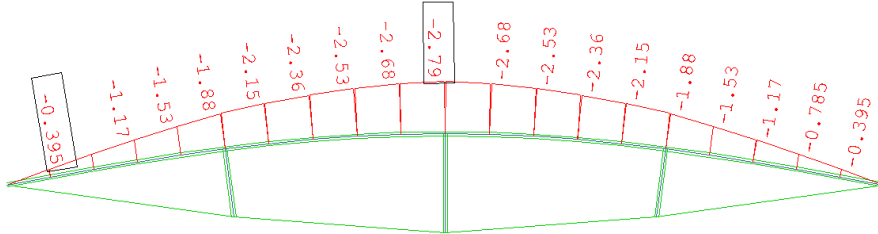


**Figure 67:** Bending moments  $M$  (kN.m) in the rod due to activation process (optimal solution).

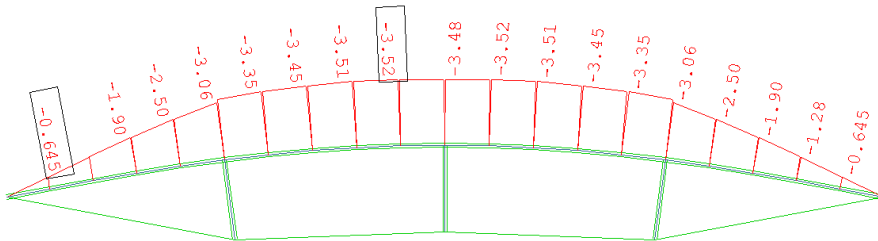


**Figure 68:** Bending moments  $M$  (kN.m) in the rod due to activation process (bad solution).

As can be observed in Figures 69 and 70, the ratio between deviator lengths  $h_q/h_m$  also influences their behaviour. For example, in the configuration corresponding to the 'bad' solution (Fig. 70), the deviator at midspan works under tension, and it could therefore be replaced by a cable. However, this structural scheme is not the most efficient to bear the action of the design loads posed by the Eurocode for footbridges. Therefore, it seems desirable to obtain configurations where deviators work under compression.

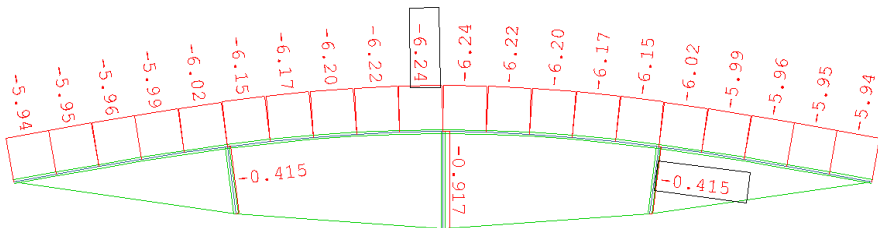


**Figure 69:** Axial forces  $N$  (kN) in the rod and deviators due to activation process (optimal solution).

The selection of the cables is also crucial in the behaviour of the whole structure. As mentioned in the previous section, solutions are characterised by cable cross-sections slightly oversized. The optimisation method evolves towards solutions where cables are designed to avoid cable slackness and provide maximum stiff-



## 6.6 SUMMARY

This chapter presents a design tool based on multi-objective optimisation for obtaining efficient structural configurations for bending-active tied arches. The structural optimisation has been carried out by a genetic algorithm, in which each plausible structural configuration has been evaluated in terms of stresses in the active member and cables, maximum deflections for serviceability limit state and lightness of the structure, according to the limitations posed by the Eurocode for footbridges. A sensitivity analysis has been carried out to improve the performance of the genetic algorithm. It is worth highlighting that it leads to genetic algorithms with small population sizes, which is also advantageous to reduce the computational cost of the simulations. Results are given in terms of non-dimensional parameters to make them applicable to the design of bending-active structures of any size and stiffness. Results show that solutions are mainly dominated by the magnitude of the design loads and limitations for deflections for the serviceability limit state. Less restrictive limitations or a different structural application such as roofing module would allow for a wider range of design alternatives. Section 6.4 shows an example based on the scalability of the solution. Finally, in section 6.5 the optimal solution reached by the algorithm has been analysed and verified from a structural point of view.



# 7

## EXPERIMENTAL FOOTBRIDGE BASED ON THE ACTIVE BENDING PRINCIPLE

” *For me, the most important part of the composition is the structure. What interests me the most is the expressive potential of structural forms.*

— **Félix Candela**

(Architect, engineer, builder and structural artist)

### 7.1 INTRODUCTION

Unlike the case of dome-shaped gridshells structures, active bending has hardly been explored in the field of pedestrian bridges. The need to achieve a tradeoff between strength and flexibility of structural members, while meeting the tight serviceability limitations posed by codes, becomes a design challenge whose solution may not straightforward. This is probably the reason there are fewer examples and built structures are practically non-existent [12, 26].

The results obtained in Chapters 5 and 6 regarding the performance for bending-active tied arches show that the design space to built short footbridges is rather narrow, however, it is open enough to explore the feasibility of some configurations. Building on this idea, this chapter presents the design of a 5 m span footbridge prototype using GFRP tubes, steel cables and steel deviating struts.

The design process comprises different stages. Firstly, the structural concept and the activation process have been tested by means of different small-scale models using glass-fiber rods and 3D printed joints. In a second step, structural proportions and cross-section dimensions have been selected from the results of a parametric study, which takes into account the limitations posed by the Eurocode for footbridges. Finally, the detail design has been carried out to fabricate and assembly the structure.

#### 7.1.1 Outline of the chapter

The outline of chapter is as follows: Section 7.2 introduces the basic principles for the design and the determination of the structural configuration. The numerical analysis of the self-stress state and serviceability state for the three-dimensional structure is developed in section 7.3. Finally, the fabrication and assembling process of the prototype are detailed in section 7.4.

## 7.2 DESIGN

### 7.2.1 Specifications

The design of the lightweight footbridge prototype is based on the following functional requirements: the maximum gradient of the deck is restricted to 6% and the width of the deck should be close to 1 m. The span should be in the range of 5 m, as the prototype is intended to be handled by a small number of people. The structural height at midspan should be close to 10% of the span, in accordance with the most typical values of height-to-span ratios used for footbridges. The structure should be also designed to resist the design load value posed by the Eurocode [41].

### 7.2.2 Materials

GFRP is selected for bending-active members, since it provides high flexural strength and adequate stiffness [36]. Steel is used for cables, deviators and custom-made joints. As explained in Chapter 5, cables must be carefully designed since oversized cross-sections lead to insufficient stresses after the activation stage and undersized cross-sections may result in overall excessive flexibility. Table 31 shows the material properties of the different elements involved in the design.

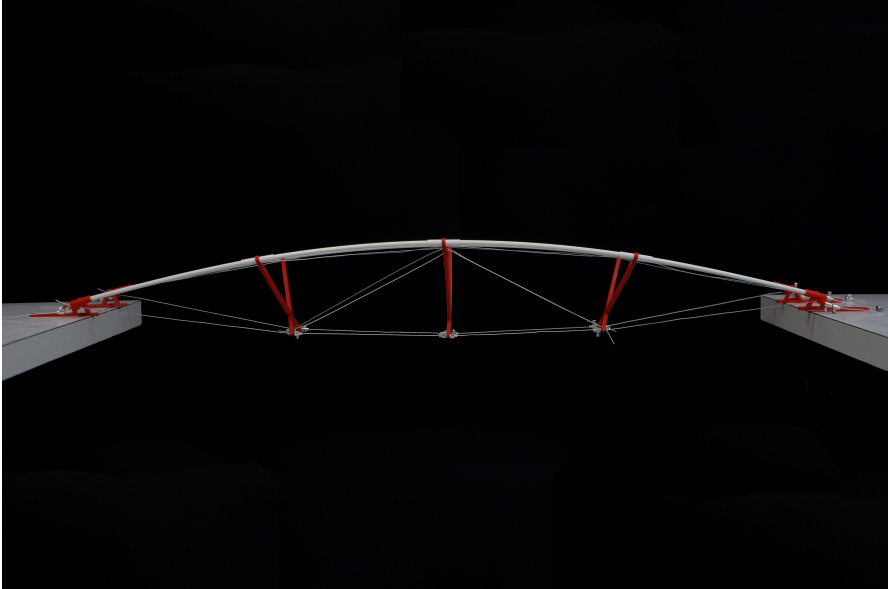
| Element           | Material | E (GPa) | $f_y$ (MPa) | $f_u$ (MPa) |
|-------------------|----------|---------|-------------|-------------|
| Rods              | GFRP     | 35      |             | 500         |
| Cable 7x7+0       | Steel    | 105     |             | 1570        |
| Struts and joints | Steel    | 210     | 275         |             |

**Table 31:** Material properties of the prototype.

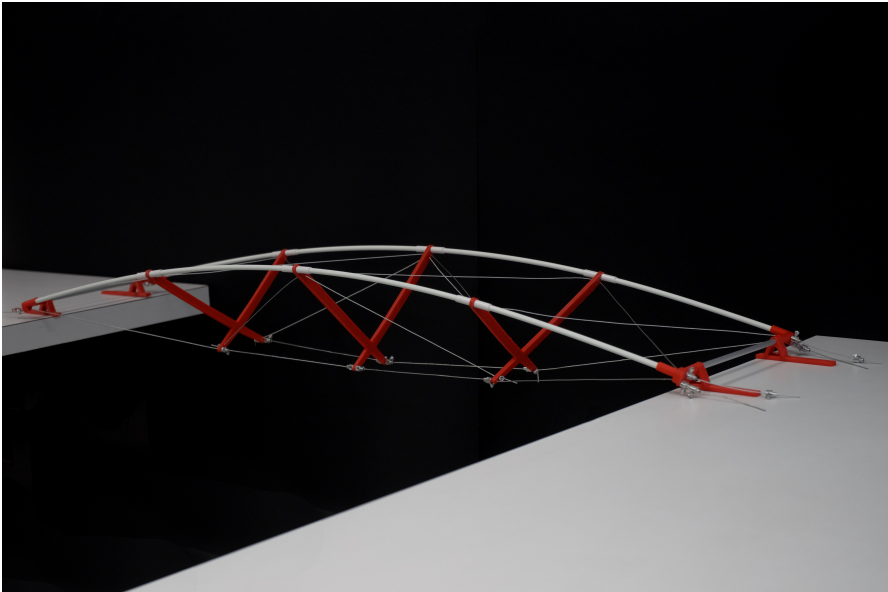
### 7.2.3 Conceptual design

The structural concept starts from a couple of planar bending-active tied arches that are independently activated. In a first stage, conceptual models were built to better understand the activation process and the three-dimensional behaviour.

Figure 73a shows the basic structural system: a flexible active member (white element) is bent through the combined action of a lower cable and three deviators (red elements). Additional diagonal members are added after activation to increase the stiffness of the system. To achieve a stiff three-dimensional system, deviators were designed as X-shaped diaphragms in the conceptual model (Fig. 73b). With this arrangement, the bending-active members were constrained to remain in vertical planes. At this stage it was crucial to realise the importance of the ratio between deviator lengths and the need to carry out a parametric study to select the structural proportions and member dimensions.



(a)



(b)

Figure 73: Conceptual model with 3D-printed joints and X-shaped deviators.

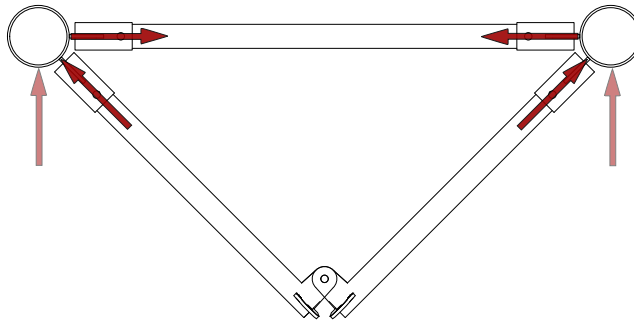


**Figure 74:** Force diagram after connecting the bending-active arches. In red colour, internal forces on the rod exerted by the struts. In pink colour, their resultant, which is (ideally) vertical.

X-diaphragms were subject to significant in-plane bending moments. To avoid this situation, the design of transverse structural elements evolved to triangular (and trapezoidal) cells (Fig. 74). This new design led to the following construction sequence: Initially, both flexible rods will be independently activated to form two planar bending-active tied arches. After that, both arches will be connected by hinged links at the level of the cable, and by means of horizontal members of equal length at the level of the rods (to achieve a constant deck width); they pull the rods inwards, forcing them to remain in vertical planes. Thereby, forces in deviators and horizontal struts have vertical resultants acting on the activated rod. Finally, diagonal cables and braces will be added to increase the torsional stiffness and complete the three-dimensional system.

As starting point and before the manufacture of the prototype, the footbridge was modelled by trial and error using a CAD software in order to assess the proportions of the solution. With the goal of achieving a structure as slender as possible, different sets of rod and cable cross-sections were considered. Figure 75 shows the side perspective rendered view of a very initial test, which stands out for a not very slender aspect of the bent rods. These infographics were also useful to examine the convenience of using wooden pallets (also called skids) for the deck. This wooden element is typically used as a flat transport structure to hold and store goods in a stable fashion. Their efficiency (they can resist up to 60 times their own weight) and sustainable character (most of them are recycled elements), make them an ideal solution for use as footbridge pavement.



**Figure 75:** Side perspective rendered view of the prototype.

### 7.2.4 Determination of the structural configuration

In this section, different potential configurations with specific dimensions of members are analysed in order to define the geometry of the most suitable planar bending-active braced arch system. For that purpose, simulations have been performed using the non-linear FE software SOFiSTiK.

The analysis focuses on symmetric structures with three equally spaced deviators. This distribution is advantageous for limiting the length between deviators (approximately 1.25 m) and is also suitable for supporting the deck. The following common data have been considered: GFRP rods are designed as 4.90 m long continuous members with hollow circular cross-section; connections between rod and deviators are free to rotate; the cross-section of the main cables is chosen to reach 10% of the maximum allowable stress after prestressing. The length of the deviator at midspan  $h_m$  is selected so that its vertical projection is equal to 0.5 m. The length of quarter-span deviators  $h_q$  is chosen as variable parameter defined by means of the ratio  $h_q/h_m$ , which can range from  $h_q/h_m = 0.5$  to  $h_q/h_m = 1$ . These last boundaries are selected to obtain a harmonious and aesthetic structure. The circular hollow cross-section of the rod is characterised by the rod slenderness parameter  $\bar{\lambda}$  (see Chapter 5, equation 91). Therefore, the two variables to be determined in this study are: (a) the slenderness of the rod  $\bar{\lambda}$  and (b) the ratio  $h_q/h_m$ . They define the size of the rod cross-section and the length of quarter-span deviators. Figure 76 is included in order to clarify the definition of the form-finding parameters.

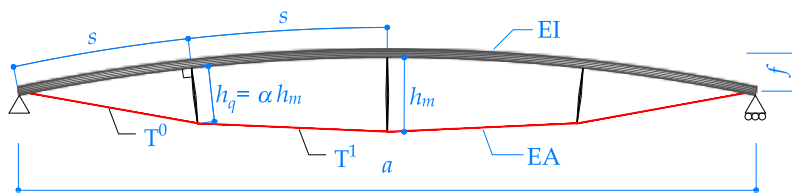


**Figure 76:** Definition of the parameters for the bending-active tied arch.

To evaluate each configuration, stresses in the rod and cables after activation have been assessed. Serviceability limit state has been also checked. For that purpose, a distributed load corresponding to 40% of the 5 kN/m<sup>2</sup> service load is applied according to EN 1991-2 [41]. With the aim of simplifying the evaluation of the serviceability limit state, deflections are only quantified at midspan at this stage. The loading pattern is a symmetric uniform load on a width chosen to be 10% of the developed length of the rod, as it has been previously done in Chapters 5 and 6. Results are expressed by diagrams in terms of rod slenderness  $\bar{\lambda}$  and the ratio  $h_q/h_m$ .

Figures 77 and 78 show the influence of the relation between deviator lengths  $h_q/h_m$  on the structural response of the planar arch. In this set of simulations, forces in cables have been adjusted to meet the functional requirement  $f/a \simeq 6\%$ , maximum allowable gradient of the deck. In this way, all solutions are comparable to each other. Simulations have been replicated for two values of rod slenderness,  $\bar{\lambda} = 1.5$  and  $\bar{\lambda} = 3$ . The first diagram 77 shows the relation between axial forces in deviators for different ratios  $h_q/h_m$ . As can be seen, the results obtained are practically independent from the rod slenderness value considered. It can also be concluded that as the deviator length at quarters decreases, the deviator at midspan is more loaded. The second diagram 78 represents the dimensionless inverse of the deflections at midspan. In this case, deflections are minimised when the value of the

rod slenderness is low. A ratio  $h_q/h_m = 0.75$  has been selected: with it, axial forces in deviators are practically equal after activation and the dimensionless deflection  $L/v$  under frequent load is minimised (in absolute value).

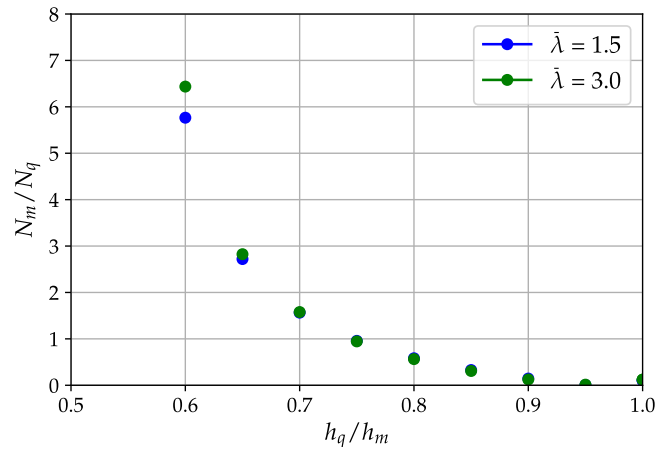


**Figure 77:** Relation between axial forces in deviators after activation for different ratios  $h_q/h_m$ .

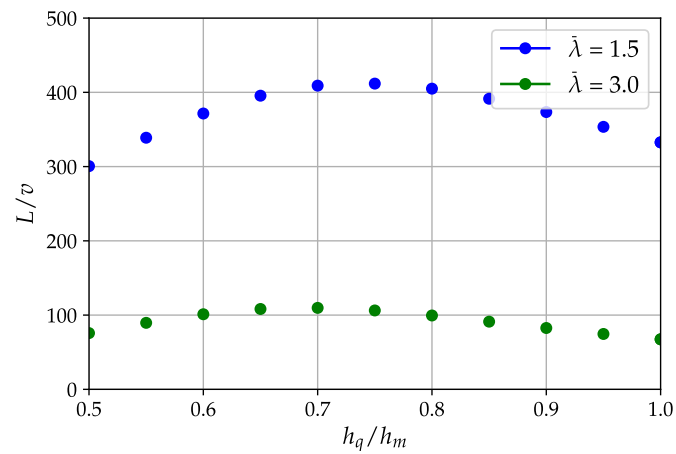


**Figure 78:** Dimensionless inverse of the deflections at mispan for different ratios  $h_q/h_m$  and rod slenderness.

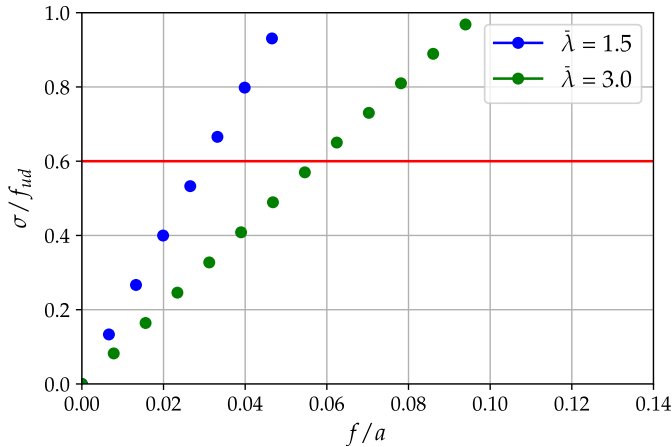


**Figure 79:** Stress levels after activation in terms of rod slenderness  $\bar{\lambda}$  and rise-to-span of the structure  $f/a$ .

Figure 78 gives the misconception that the choice of low rod slenderness values is favourable because deflections are lower. However, this diagram does not consider the stress level produced as a result of the form-finding process, which is the most limiting restriction in the design of bending-active structures. In GFRP materials, it is estimated that stresses after activation shall be limited to 30% - 60% of the maximum allowable stress to avoid the emergence of long-term strains due to creep [36, 64]. Figure 79 shows the evaluation of the normal stresses produced by the bending effect at midspan –where maximum curvatures are reached–, in terms of the ratio  $f/a$  and rod slenderness  $\bar{\lambda}$  for the selected ratio  $h_q/h_m = 0.75$ . It allows to choose the rod slenderness compatible to reach the 60% of the design ultimate strength<sup>1</sup>  $f_{ud} = f_u/3$ , for a given rise-to-span ratio  $f/a$ . As expected, lower values of rod slenderness  $\bar{\lambda}$  lead to higher stresses as the curvature of the rod increases. Using the diagram, two limit configurations are possible: (a) a rod slenderness  $\bar{\lambda} = 1.5$  with a rise-to-span ratio  $f/a = 3\%$ ; (b) a rod slenderness  $\bar{\lambda} = 3$  with a rise-to-span ratio  $f/a = 6\%$ .

Both configurations have been evaluated in terms of structural stiffness  $K$  (Fig. 80). In this analysis, the structural stiffness  $K$  is defined as the ratio  $K = F/v$ , where  $v$  is the maximum deflection of the system for a certain applied load  $F$ . The diagram depicts the relationship between the rise-to-span ratio  $f/a$  and the increase in stiffness  $\Delta K$  with respect to a flat configuration, in other words, a conventional structure with a straight rod. The diagram shows that the structural system is stiffer as the curvature of the rod increases. A second key observation is that slender rods are more advantageous in terms of increased stiffness  $\Delta K$  for a given structural shape  $f/a$ . For example, setting a rod slenderness  $\bar{\lambda} = 1.5$  and rise-to-span ratio  $f/a = 3\%$ , the difference in stiffness  $\Delta K$  when comparing the solution with a flat structure is about 5%. However, choosing a rod slenderness value  $\bar{\lambda} = 3$ , which allows to reach the prescribed functional requirement  $f/a = 6\%$  in terms of stresses (Fig. 79), the system is 15% stiffer than its equivalent straight configuration. In parallel, it is necessary to check that in absolute terms the system is sufficiently stiff in order to validate the design.

<sup>1</sup> The partial safety factor of the GFRP material has been selected considering the short-term and long-term effects [38].

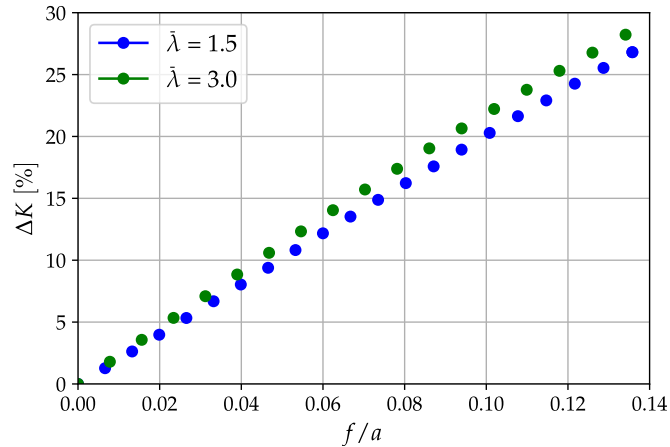


**Figure 80:** Increase in stiffness  $\Delta K$  after activation in terms of rod slenderness  $\bar{\lambda}$  and rise-to-span of the structure  $f/a$ .

Moreover, active members with a high rod slenderness are advantageous because they allow to reach higher curvatures during the form-finding process and are easy to manipulate during construction, which reduces labour and costs considerably. These observations highlight the suitability of bending-active systems on the search of efficient uses of technological materials and high-tech concept-design-erection-processes to produce aesthetic lightweight structures such as footbridges or roofing applications.

On the basis of the foregoing, a rod slenderness  $\bar{\lambda} = 3$  has been chosen. From commercial solutions, it can be achieved using a circular hollow cross-section with an outer diameter of 50 mm and a thickness of 3.5 mm. The cross-section of the main cables has been chosen to reach a minimum level of stress after prestressing. For the selected wire rope typology, the size of the cable selected is 4 mm. Struts are thin-walled circular cross-section with an outer diameter of 22 mm and a thickness of 2.5 mm.

### 7.3 VERIFICATION OF LIMIT STATES

This section shows the evaluation of the self-stress state and serviceability state for the three-dimensional structure. For that purpose, the simulations have been also performed with the FE software SOFiSTiK.

#### 7.3.1 Self-stress state

The equilibrium configuration of the structure has been found simulating the actual erection process, which is divided in multiple steps. Initially, the form-finding process starts from a couple of unstressed tied arches that are separated from each other by 1 meter at rod level and connected by a hinged joint at cable level. The beam-ends nodes of the elements that simulate the deviators at midspan section are fully fixed to achieve a stable system and to avoid numerical instabilities (Fig. 81a). After that, both arches are independently activated to form two planar bending-active tied arches (Fig. 81b). Then, the rods are forced outwards to reach the desired

deck width. For that purpose, virtual cables that are shortened by prestressing forces are used (Fig. 81c). This manoeuvre is carried out in two steps. First, rods are moved outwards until a separation of 1 meter is reached at the quarter span sections. The achieved distance between rods is then kept by introducing horizontal struts (Fig. 81d). The last adjustment is conducted at rods ends. In this case, the deck width is fixed at 0.8 meters. Finally, diagonal cables and braces are added to become the system stiffer (Fig. 81e).

Table 32 shows the evolution of the section-forces for the active members and cables during the activation process. Section forces diagrams are available in the Appendix A. The analysis of the structural response of the horizontal struts is another interesting point, as they work in a different way as the erection process progresses. Table 33 shows how horizontal struts behave at the different stages. As can be seen, when struts are installed, they work in compression (with the exception of the strut at midspan, which only resists the horizontal component due to the activation of the arches). However, as the rods are pulled outwards to add the successive horizontal struts, the previous ones, already installed, change their response from a state of compression to a state of traction.

|    | Rod at midspan cross-section |              |              | Outer cable | Inner cable |
|----|------------------------------|--------------|--------------|-------------|-------------|
|    | N (kN)                       | $M_y$ (kN.m) | $M_z$ (kN.m) | N (kN)      |             |
| b) | -0.66                        | 0.33         | 0.35         | 0.70        | 0.66        |
| e) | -1.09                        | 0.47         | 0.23         | 1.01        | 0.89        |

**Table 32:** Section forces in the rod and cables during the activation process.

|    | Strut at midspan | Strut at quarters | Strut at rod ends |
|----|------------------|-------------------|-------------------|
|    | N (kN)           |                   |                   |
| c) | 0.34             | -                 | -                 |
| d) | -0.16            | -0.22             | -                 |
| e) | -0.24            | 0.10              | -0.3              |

**Table 33:** Section forces in the horizontal struts during the activation process.

Stress levels in the rod and cables due to the activation process have been quantified using the section forces previously shown in Table 32. The maximum stress in the rod at the form-finding stage is:

$$\sigma_{r,FF} = \frac{N}{A} + \frac{M_y + M_z}{I} \frac{d}{2} = 149.6 \text{ MPa} \quad (102)$$

Cables are evaluated taking into account that both outer and inner positions are working in a very similar stress range. The maximum stress is calculated for the outer cable:

$$\sigma_{c,FF} = \frac{N}{A} = 97.5 \text{ MPa} \quad (103)$$

The utilisation ratios for the rod and cables are obtained according to the EN 1993-1-1 [42], as previously explained in Chapters 5 and 6. The utilisation ratio for the rod is calculated as follows:

$$\frac{\sigma_{r,FF}}{f_{u_r}} = \frac{149.6}{500} = 0.3 \quad (104)$$

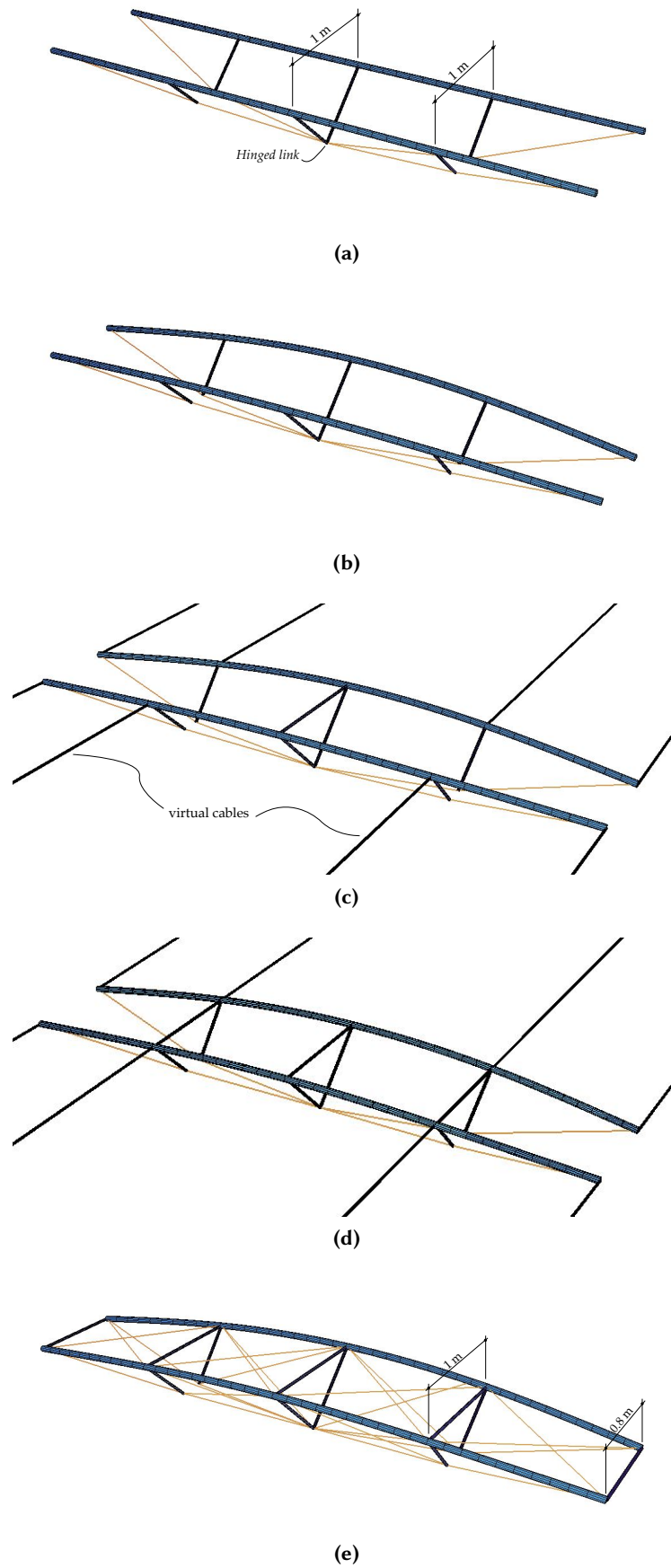


**Figure 81:** Simulation of the assembling process of the structure.

The utilisation ratio for the cable is:

$$\frac{\sigma_{c,FF}}{f_{uc}} = \frac{97.5}{1570} = 0.06 \quad (105)$$

As it can be seen, the activation process is consuming about the 30% of the ultimate strength of the material of the rod after activation, which is an acceptable threshold to avoid long-term strains. Cables are slightly oversized, as their utilisation ratio is around 6%, which provides the required global stiffness to the arch, at the expense of a low, but sufficient, cable stress after activation. As expected, results are similar to the ones shown in Chapters 5 and 6.

### 7.3.2 Dead load

Apart from the self-weight of the bending-active tied arches and service loads, the structure has to resist the dead load caused by the installation of four standard European pallets that act as the deck of the footbridge. The dead load of the deck is  $0.2 \text{ kN/m}^2$ . Table 34 shows the resulting section forces in the rod (at midspan cross-section) and in cables. The maximum deflection due to this load case is equal to 6 mm. This deflection is not considered in the calculations of the active deflection, which is only calculated with the service loads.

| Rod at midspan cross-section |              |              | Outer cable | Inner cable |
|------------------------------|--------------|--------------|-------------|-------------|
| N (kN)                       | $M_y$ (kN.m) | $M_z$ (kN.m) | N (kN)      |             |
| -1.71                        | 0.46         | 0.23         | 1.5         | 1.3         |

**Table 34:** Section forces in the rod and cables due to the installation of the pallets.

### 7.3.3 Serviceability state

As previously explained, the serviceability state has been evaluated according to the loading models posed by the Eurocode for footbridges [41]. The magnitude and position of the loads are adjusted so that a load testing can be performed in the laboratory using 20 kg sandbags to verify the results. Sandbags are modelled as vertical loads that act directly on the custom-made joints, since the pavement (pallets) rests on them. Depending on the distribution of the sandbags over the structure, different load cases result. Three cases are evaluated: (a) a symmetric load case; (b) a non-symmetric load case and (c) a torsional load case. They are described in the following sections. All load models as well as the numerical results can be consulted in the Appendix A.

#### 7.3.3.1 Symmetric load case

The symmetric load case consists in placing 10 sandbags uniformly distributed over the two most centered pallets of the footbridge, which is equivalent to a mass of 200 kg, 100 kg per pallet. Table 35 shows the resulting section forces in the rod (at midspan cross-section) and cables for this load case. The maximum vertical displacement is located at midspan and is equal to 12 mm. This means an approximate ratio  $f/a$  of  $L/400$ .

| Rod at midspan cross-section |                       |                       | Outer cable | Inner cable |
|------------------------------|-----------------------|-----------------------|-------------|-------------|
| N (kN)                       | M <sub>y</sub> (kN.m) | M <sub>z</sub> (kN.m) | N (kN)      |             |
| -2.87                        | 0.44                  | 0.23                  | 2.5         | 2.2         |

**Table 35:** Section forces in the rod and cables due to the symmetric load case for the load testing.

The stress levels in the rod and cables have also been calculated for the service states, in order to evaluate the utilisation ratio of the structural elements when different external loads act. Using the section forces (Table 35), the maximum stress in the rod due to the symmetric load case is obtained as follows:

$$\sigma_{r,Sym} = \frac{N}{A} + \frac{M_y + M_z}{I} \frac{d}{2} = 126.1 \text{ MPa} \quad (106)$$

The maximum stress is obtained in the outer cables:

$$\sigma_{c,Sym} = \frac{N}{A} = 348.2 \text{ MPa} \quad (107)$$

The utilisation ratio for the rod is:

$$\frac{\sigma_{r,Sym}}{f_{ur}} = \frac{126.1}{500} = 0.25 \quad (108)$$

The utilisation ratio for the cable is:

$$\frac{\sigma_{c,Sym}}{f_{uc}} = \frac{348.2}{1570} = 0.22 \quad (109)$$

It is worth noting that the utilisation ratio for the rod is slightly lower when service loads are applied than after activation. This is because the application of an external load causes in the active member a curvature increment of positive sign, which compensates the negative curvature induced during the activation process, resulting in a lower value of the bending moment.

### 7.3.3.2 Non-symmetric load case

The non-symmetric load case consists of loading half of the footbridge using 10 sandbags. This is equivalent to loading two pallets on one side of the footbridge. In Table 36 the section forces in the rod (at midspan cross-section) and cables for this load case are shown. The maximum vertical displacement is located at quarters and is equal to 7.5 mm. At midspan, the maximum deflection is equal to 6.1 mm. This means approximate ratios  $f/a$  of  $L/600$  and  $L/800$ .

| Rod at midspan cross-section |                       |                       | Outer cable | Inner cable |
|------------------------------|-----------------------|-----------------------|-------------|-------------|
| N (kN)                       | M <sub>y</sub> (kN.m) | M <sub>z</sub> (kN.m) | N (kN)      |             |
| -2.52                        | 0.45                  | 0.23                  | 2.4         | 1.9         |

**Table 36:** Section forces in the rod and cables due to the non-symmetric load case for the load testing.

Stresses are calculated in the same way as in the previous cases. From Table 36, the maximum stress in the rod for the non-symmetric load case is:

$$\sigma_{r,Non-sym} = \frac{N}{A} + \frac{M_y + M_z}{I} \frac{d}{2} = 127.2 \text{ MPa} \quad (110)$$

The maximum stress in cables is:

$$\sigma_{c,Non-sym} = \frac{N}{A} = 334.3 \text{ MPa} \quad (111)$$

The utilisation ratio for the rod is:

$$\frac{\sigma_{r,Non-sym}}{f_{ur}} = \frac{127.2}{500} = 0.25 \quad (112)$$

The utilisation ratio for the cable is:

$$\frac{\sigma_{c,Non-sym}}{f_{uc}} = \frac{334.2}{1570} = 0.21 \quad (113)$$

As it can be observed, both symmetric and non-symmetric load cases lead to similar results in terms of utilisation ratio.

### 7.3.3.3 Torsional load case

The torsional load case consists of loading the half area of the most centered pallets of the footbridge using 10 sandbags. In this way, the global torsional stiffness, as well as the lateral stability can be checked. Table 37 shows the section forces in the rod (at midspan cross-section) and in cables for this load case. For this analysis, the maximum deflection is located at midspan and is equal to 7.6 mm. As expected, this load pattern causes rotation of footbridge cross-sections. The vertical displacement due to the rotation of the central cross-section at one side is equal to 2.1 mm.

| Rod at midspan cross-section |              |              | Outer cable | Inner cable |
|------------------------------|--------------|--------------|-------------|-------------|
| N (kN)                       | $M_y$ (kN.m) | $M_z$ (kN.m) | N (kN)      |             |
| -2.52                        | 0.47         | 0.23         | 2.1         | 1.8         |

**Table 37:** Section forces in the rod and cables due to the torsion load case for the load testing.

Finally, from Table 37, the maximum stress in the rod is obtained as follows:

$$\sigma_{r,Torsion} = \frac{N}{A} + \frac{M_y + M_z}{I} \frac{d}{2} = 130.8 \text{ MPa} \quad (114)$$

The maximum stress in cables is:

$$\sigma_{c,Torsion} = \frac{N}{A} = 292.5 \text{ MPa} \quad (115)$$

The utilisation ratio for the rod is:

$$\frac{\sigma_{r,Torsion}}{f_{ur}} = \frac{130.8}{500} = 0.26 \quad (116)$$

The utilisation ratio for the cable is:

$$\frac{\sigma_{c,Torsion}}{f_{uc}} = \frac{292.5}{1570} = 0.19 \quad (117)$$

This load case leads to similar stress levels as in the previous load cases.

## 7.4 FABRICATION

A detailed design of the prototype has been developed. Figures 82a and 82b show rendered views of the transverse frames composed of inclined deviators, horizontal struts between rods and bottom hinged links.



(a)



(b)

**Figure 82:** Detail of deviators; 82a at midspan, 82b at quarters.

The final structure weights around 1.2 kN and the resisted load-to weight ratio is close to 17.



**Figure 83:** Experimental footbridge based on the active-bending principle.

#### 7.4.1 Fabrication of the nodes

The design of the nodes depends on their position and function. They have to comply several conditions:

- **Strength:** the node has to transmit the tension and compression forces in a safe way.
- **Size:** the optimisation of the node is crucial to keep a slender appearance and to reduce as much as possible the final weight of the structure.
- **Adaptability:** special attention must be paid to the orientation of gusset plates because in the final configuration the different parts of the main cables are not contained in a single plane.

Figures 84a and 84b show the first design of the nodes by using 3D printing. These 1:1 models were useful to validate the geometric interaction with the rest of the structural elements. Afterwards, they were used by the manufacturer as a reference to fabricate the final steel joints.

The manufacture of these nodes using steel as a material was not without difficulties; finding a manufacturer willing to fabricate such a small quantity of complex pieces became a challenge. After some iterations with different technicians, a metal shop offered a compromise solution. Figures 85a and 85b show the reached solution.

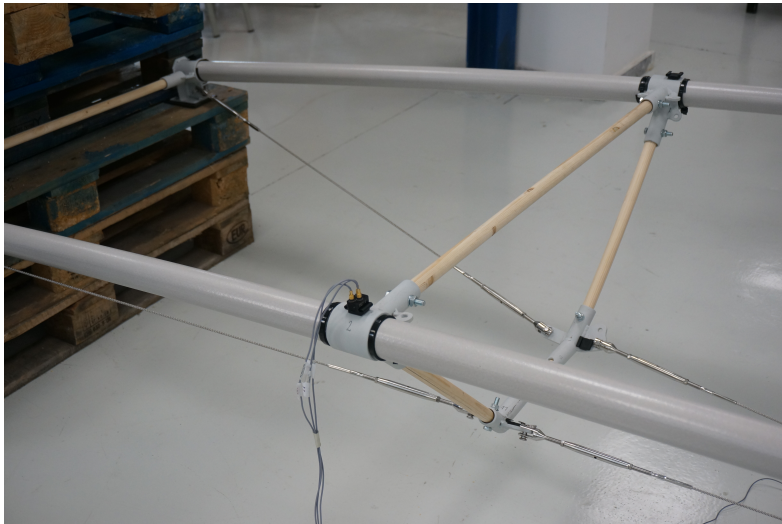


(a)



(b)

**Figure 84:** Reproduction of the custom-made joints by using 3D printing.



(a)



(b)

**Figure 85:** Detail of the custom-made steel joints.

### 7.4.2 Assembling process

The assembly process involves the activation of the structure. Therefore, it should reproduce the sequence described in section 7.3.1. It has been designed to be handled by a small number of people and without the use of heavy tools. The erection sequence is summarised as follows:

1. Each unstressed arch is prepared on a flat surface with all the necessary elements (Fig. 86).
2. The tensioning process starts with the installation of the ratchet at both ends of the rod (Fig. 87).
3. The rod is bent by the action of the ratchet pulling at both ends. The designer can control the curvature of the arch by modifying the ratchet tension (Fig. 88).
4. The main cables are connected taking advantage of the ratchet tension. After that, the tensioning forces are transferred from the ratchet to the cables (Fig. 89). In this prototype, cables are adjusted by reaching the desired shape of the arch, but for larger structures, the author suggests the use of tension measuring instruments to ensure the level of pre-stress in the cables. It is also worth mentioning the need for a tensioning plan for the cables to deal with the loss of pre-stress over time.
5. The bending-active tied arches are placed at the final position (Fig. 90) and connected by a hinged joint at cable level (Fig. 91).
6. The horizontal struts are installed to reach the desired deck width (Figs. 92, 93)
7. Diagonal cables and braces are added to stiffen the structural system.

The prototype has been assembled twice. The first time, it was assembled by only one person in one day. The second assembly involved two people, spending around five hours. As can be seen in the pictures, the first assembly was carried out with wooden deviators and the second with steel deviators. This is because the wooden deviators were not strong enough. From the point of view of robustness, all the main cables that make up the primary system are important, however, the installation of diagonal cables makes the overall system more robust. In this direction, the design of the additional cables could be also addressed by taking into account the breakage of a main cable.



**Figure 86:** Erection process of the prototype (a).



**Figure 87:** Erection process of the prototype (b).

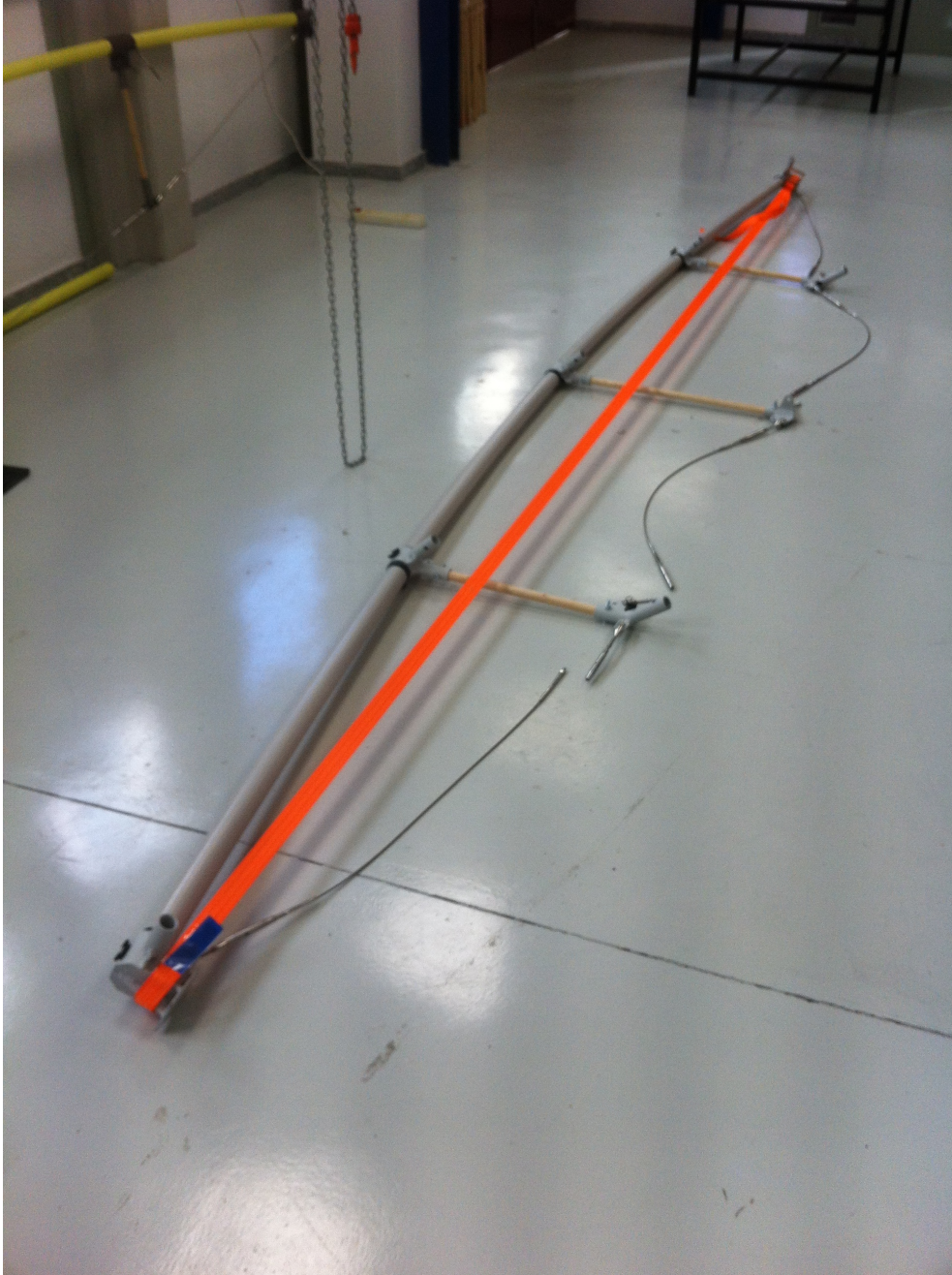


**Figure 88:** Erection process of the prototype (c).



**Figure 89:** Erection process of the prototype (d).



**Figure 90:** Erection process of the prototype (e).



**Figure 91:** Erection process of the prototype (f).



**Figure 92:** Erection process of the prototype (g).



**Figure 93:** Erection process of the prototype (h).

### 7.4.3 Future works

Static and dynamic experimental tests are planned to validate the FEM results and the overall structural response. Unfortunately, the outbreak of the COVID-19 pandemic interrupted the activities in laboratories and the inclusion of these results in the PhD thesis has not been possible.

## 7.5 SUMMARY

This chapter presents the design of a short span bending-active footbridge prototype. Starting with concept models, a parametric study has been performed to define the most suitable structural bending-active tied arch configuration. Secondly, a FE model has been built to evaluate the structural behaviour of the footbridge. This model takes into account the assembling process of the structure and the evaluation of the serviceability state. Stresses in the active member and cables and maximum deflections have been assessed. Finally, the fabrication and assembling process of the prototype have described in detail. The prototype reflects the current state of the exploration process and emphasises that lightness and efficiency can be achieved through active bending.



**Figure 94:** The experimental footbridge prototype in service.



# 8

## CONCLUSIONS AND FUTURE RESEARCH

” *The technical literature on structural engineering abounds with theoretical works of a mathematical nature, but few publications are concerned with the various kinds of structures or the fundamental reasons for their existence.*

– **Eduardo Torroja y Miret**  
(Structural engineer)

### 8.1 SUMMARY OF RESULTS

As seen in the literature, elastic gridshells and other bending-active structures have increasingly become focus of research and experimental realisations in recent times because they exploit the following advantages:

- Low consumption of materials resulting in lightweight systems.
- Possibility to use bio-based materials (timber, bamboo).
- Original members are straight, and joints are repetitive.
- Curved structural shapes, not limited to canonical forms, can be achieved.

However, they are not free from drawbacks:

- The equilibrium configuration cannot be determined beforehand due to the non-linearity of the structural response of the active members.
- Some suitable materials have less-desirable properties (brittle failure modes of GRFP, limited strength and/or durability of exposed bio materials, or high prices in the case of high-strength steel).
- Full assembly on the ground and subsequent lifting is limited to small to medium scales. Interferences between members and supports during the lifting process may cause difficulties.
- Limited applicability in the case of structures with larger loads, like bridges or footbridges, mainly because of stiffness requirements.

In this PhD thesis, the applicability of the active bending principle for the design of lightweight structures, in particular pedestrian bridges, has been explored and assessed. This has been carried out from three points of view:

- Computational form-finding and simulation.
- Structural performance and efficiency.
- Design and construction.

The first part of this work presents a novel form-finding method based on the geometrically exact rod model (or Reissner-Simo beam theory). The geometrically exact model was designed to handle the mechanical problem of very flexible rods, considering displacements of the beam centreline and rotations of the cross-sections as independent variables and manipulating 6 degrees-of-freedom per node (3 translational and 3 rotational) to provide a complete description of the kinematics and a straightforward definition of rotational boundary conditions.

In this context, the main contribution of the author has been the numerical implementation of this mechanical model into a dynamic relaxation (explicit) algorithm. The specialisation of Reissner-Simo's model to the dynamic relaxation procedure relies on: (a) the derivation of element end forces from the internal virtual work equation (sect. 3.4.2); (b) the derivation of the expression of the change of orientation in the element (sect. 3.4.3); (c) the definition of the numerical step using Newmark's algorithm and the full expression of the inertial torques (Eq. 39b); and (d) the update of angular velocities considering that nodal frames are changing (Eq. 44). In contrast to the work of other authors, a design strategy where the form-finding process is driven by kinematic constraints has been implemented. The equilibrium configuration is achieved by defining restrictions at end nodes and using the beam length as a design parameter. The numerical examples have also shown the ability and accuracy of the method to simulate the deformation process of the active members starting from an initial geometry far from the equilibrium solution.

Despite the dynamic relaxation algorithm developed in this PhD thesis has provided reliable results in terms of accuracy and computational cost, the redirection of the PhD objectives to the field of practise and application has motivated the use of other more direct form-finding techniques, suited for the specific structural type developed in the thesis. For this reason, this tool has not been used in the following chapters of thesis, giving way to a semi-analytical method supported by FEM modelling and, in a further step, enhanced by optimisation.

The second part of the thesis focuses on the development and structural analysis of a promising structural type to build lightweight structures, in particular pedestrian bridges or roofing applications, named by the author as *bending-active braced (or tied) arch* and consisting of a slender beam with an attached lower cable in tension and bracing struts (deviators) balancing the forces between them. This system is based on the well-established structural type, the *beam string*, and takes advantage of the possibilities offered by the active bending paradigm: when a slender beam is used, the tension in the cable induces curvature in the beam and increases the structural depth of the system. This opens new formal possibilities and results in lightweight structures at the expense of increasing their overall flexibility. The target shape of the system is achieved as a result of the tensioning process and needs to be pre-determined by means of a particular analysis.

In a first approach, a novel analytical design procedure has been proposed to generate shapes for this kind of structures. This procedure is based on the observation that each segment of the activated rod between deviators behaves as a segment of elastica; this enables the use of closed-form expressions to evaluate the shape and induced stress level in the active member. This study made possible to establish a direct relation between shape and activation forces for a given material and cross-sectional shape in terms of non-dimensional magnitudes, which makes it applicable to wide variety of scales and cross-section properties.

Once the target shape has been determined, the assessment of the structural performance with regard to with the limitations posed by the Eurocode for footbridges is crucial to ensure the appropriateness of the solution. For that purpose, a finite number of computer simulations have been conducted to find patterns of relationship between structural shape, activation stress levels, and limits of utilisation, using the non-linear finite element analysis with the software package SOFiSTiK. With the results of the study, general non-dimensional diagrams have been devised to design bending-active tied arches with three deviators of a particular geometry and member proportioning.

In order to obtain efficient solutions without limitation of geometrical restrictions, the author has automated the design process developing a multi-objective optimisation tool based on a genetic algorithm. This genetic algorithm assigns a fitness value to each plausible structural configuration considering the weight of the structure, stresses in the active member and cables, and maximum deflections in the serviceability limit state, according to the limitations posed by the Eurocode for footbridges. Then, the algorithm classifies, selects, and combines the best specimens to reach a configuration that minimises the fitness function according to best performance.

The results obtained regarding the performance of simple tied arch systems for pedestrian footbridge applications have shown that the limits of solutions for Eurocode footbridge loads are dictated by (a) instability in the active members, (b) maximum stress after activation, (c) minimum stresses in the activation cables and (d) maximum allowable deflections. Therefore, the resulting design space is rather narrow, mainly because of the magnitude of the load and the severe limitations for deflections in service limit states posed by the code. A wider solution space should be possible for structures subject to moderate loads and/or with less severe serviceability conditions.

In the third last of the thesis, the design, fabrication and assembling of an experimental lightweight bending-active footbridge has been presented. Using the knowledge earned along the development of the thesis, a 5 m span footbridge prototype has been designed and built. The design process has been carried out by using different techniques. Firstly, small-scale models using glass-fiber and 3D printed joints have been used to better understand the activation process. Secondly, structural proportions have been selected using a parametric study. In order to validate the feasibility of the system, numerical tests have simulated the assembling process and load testing. The fabrication and assembling processes have been also described. The erection process has demonstrated that the prototype can be efficiently assembled by just 1 (or 2) people. Currently, the prototype is awaiting laboratory tests.

## 8.2 MAIN CONCLUSIONS

During the development of this PhD thesis, several research questions regarding the applicability of active bending to the design of pedestrian bridges have been raised. Some of these questions were already introduced in Chapter 1. This section aims to answer them, from the author's point of view and considering what was learned during this research.

### *WHERE ARE THE LIMITS OF APPLICABILITY FOR BENDING-ACTIVE STRUCTURES?*

It is difficult to say where the limits are, but it is easy to identify them. It can be said that the main limitation when designing a bending-active structures is the overall flexibility of the system. In most cases, the need to use slender members to keep activation stresses low during the tensioning process results in overly light configurations that do not meet the limitations for deflections posed by the codes. For instance, the Eurocode establishes a maximum dimensionless deflection of  $L/1200$  for footbridges under frequent service loads; however, our prototype would have a maximum deflection of  $L/400$  under the mentioned loading, which is quite far from the Eurocode limitation. Therefore, active bending should be limited to those situations where flexibility is not an issue or where service loads are moderate.

### *IS IT POSSIBLE TO BUILD STRUCTURES WITH LARGER LOADS LIKE PEDESTRIAN BRIDGES?*

Yes, it is possible. This has been demonstrated in this thesis. However, as explained before, the flexibility of the system is not compatible with the restrictions for deflections posed by the Eurocode. This observation must be understood in the context of this work, since the study is limited to GFRP materials. The use of other promising materials, such as an ultra-high performance concrete (UHPFRC) could considerably improve the structural behaviour of the system regarding deformations.

### *ARE BENDING-ACTIVE STRUCTURES ADVANTAGEOUS OVER PASSIVE (STANDARD) ONES?*

This is the key question... and there is still no clear answer. Each typology has advantages and disadvantages. For example, bending-active structures are easy to manipulate; they are made up of slender (light) elements, which are easy to fabricate and transport. A passive structure with a curved shape is, in general, more expensive. In addition, the comparison of solutions with equal weight (passive vs. bending-active) is advantageous for the bending-active ones, because curvature increases the stiffness. However, the shallow cross-sections of the bent members required for the activation result in structures that are lighter, but at the same time more flexible than conventional structures. As already mentioned, this can be disadvantageous for certain applications with strict deformability requirements.

### *IS FURTHER RESEARCH INTO ACTIVE BENDING INTERESTING?*

Definitely, it is interesting. The fact is that there is an increasing interest in investigating the behaviour of very flexible structures. However, a lot of attention has been directed to the development of computational form-finding tools and realisations of sculptural nature. In my opinion, to advance knowledge in the field of structural performance would be the most profitable strategy in order to better understand how these structures can be applied taking into account all limitations.

### 8.3 FUTURE LINES OF RESEARCH

The following theoretical and experimental areas are suggested for further research in this area:

**FORMULATION OF A LARGE DEFORMATION MODEL FOR SLENDER BEAMS** The recent interest in the finite element implementation of beams undergoing very large displacements has been already mentioned in the state of the art. One of the most relevant results of this research is the numerical implementation of a dynamic relaxation algorithm using a geometrically exact beam model (6 degrees-of-freedom per node). This tool has already shown promising results, but still has room for improvement. An interesting development path is the adaptation of the numerical framework to make the method applicable to structures composed of multiple active members and cables. Another challenging line of research is the incorporation of a shear-free model for non-linear flexible beams with 4 DoFs (Kirchhoff's theory) into the finite element model implementation. For very slender rods, shear deflections are negligible, and the rotation of the cross-section is partially determined by the tangent to the deformed centreline (Kirchhoff rods). The number of rotational degrees of freedom can be reduced to only one, but there are few non-linear implementations in the literature because the underlying mathematical modelling is far from trivial. In this connection, there are previous works with different approaches, for example, Du Peloux et al. [39] proposed an element with 4 DoFs based on finite-difference discretisations.

**DEVELOPMENT OF AN ALTERNATIVE CONCEPT TO FABRICATE, ASSEMBLE AND ERECT MEDIUM SCALE BENDING ACTIVE SYSTEMS** A system composed of progressively activated individual elements (kit-of-parts) would be a practical alternative to building with long continuous members. The overall concept of this novel system, as well as the detailing of member cross sections, joints and activation procedure must be developed.

**APPLICATION OF ULTRA-HIGH PERFORMANCE CONCRETE (UHPRC) AS A MATERIAL TO DESIGN BENDING-ACTIVE MEMBERS** The concept of *bending* concrete is not a new one: Dante Bini introduced a method to build domes in the 1960s by casting the mixture on a membrane, and then inflating it before the concrete has set. Recently, Kromoser and Kolleger [52] have developed a variant of Bini's method by casting thin flat panels of textile reinforced concrete and bending them into a 3D shape by means of an inflatable membrane, once the concrete has hardened. The resulting domes show a smeared cracking pattern in the target curved shape. This approach is close to active bending, the main difference being the fact that the material cracks and is not working elastically during activation. UHPRC in active members is expected to lead to structural systems that are still lightweight and have reduced material consumption, but have higher ductility and robustness as those built with GFRP or even timber, and possibly, allow to achieve larger scales.

The research group is currently working on the design and manufacturing of an experimental bending-active short footbridge made of ultra-high-performance concrete (UHPC). The footbridge is composed of a thin UHPC prestressed slab, UHPC deviators and stainless-steel tensioning cables. The UHPC prestressed flexible slab is cast in an initially flat shape; once the concrete hardens, it is elastically bent in the

longitudinal direction by means of the strut-and-cable system to achieve the desired structural configuration. Figure 95a shows the slab casted in an initially flat shape and Figure 95b shows the final shape upside-down after the tensioning process.



(a) Initial configuration.



(b) Final configuration after the tensioning process.

**Figure 95:** Bending-active short footbridge made of ultra-high-performance concrete (UHPC).

## APPENDIX



# A

## NUMERICAL RESULTS FOR THE PROTOTYPE FE MODEL

This appendix shows the resulting section forces diagrams and vertical deflections from the simulation of the experimental bending-active footbridge in the FE software SOFiSTiK.

### A.1 FORM-FINDING PROCESS

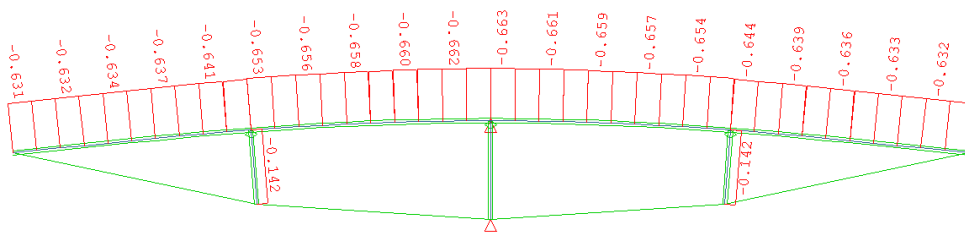


**Figure 96:** Axial forces  $N$  (kN) in the rod and deviators due to activation process (stage (a)).

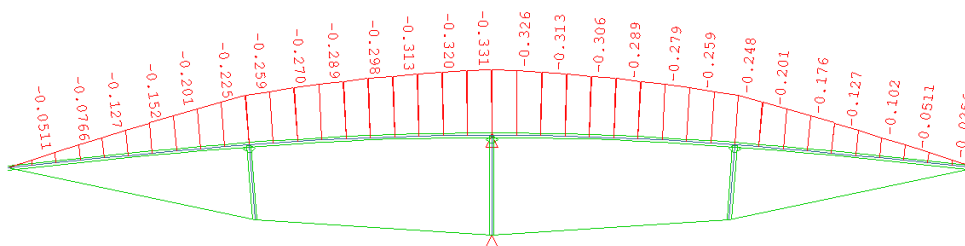


**Figure 97:** Bending moments  $M_y$  (kN.m) in the rod and deviators due to activation process (stage (a)).

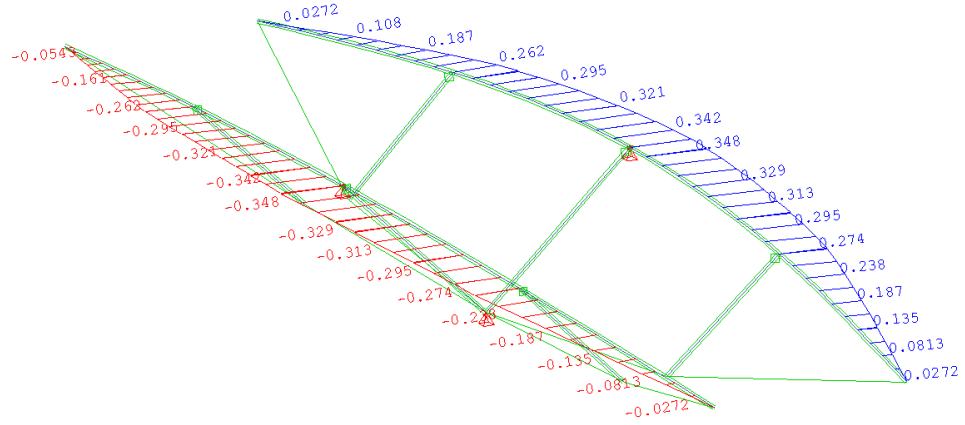


**Figure 98:** Bending moments  $M_z$  (kN.m) in the rod and deviators due to activation process (stage (a)).

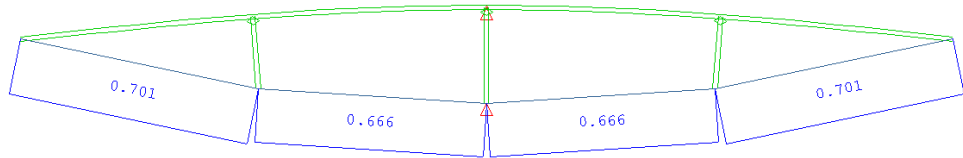


**Figure 99:** Axial forces  $N$  (kN) in cables due to activation process (stage (a)).

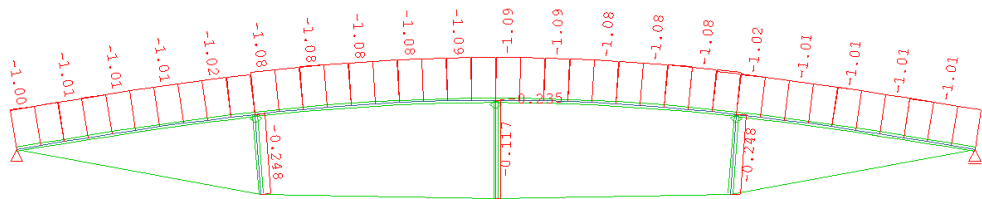


**Figure 100:** Axial forces  $N$  (kN) in the rod and deviators due to activation process (stage (e)).

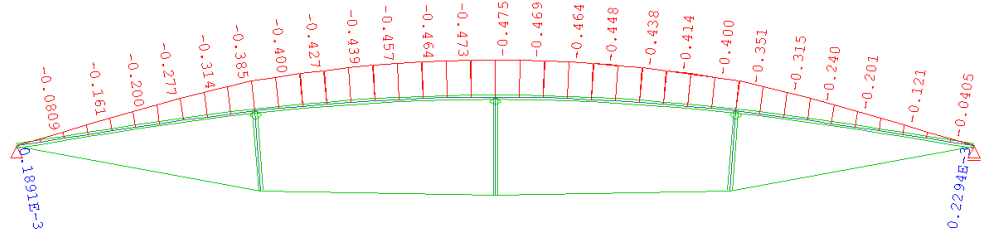


**Figure 101:** Bending moments  $M_y$  (kN.m) in the rod and deviators due to activation process (stage (e)).

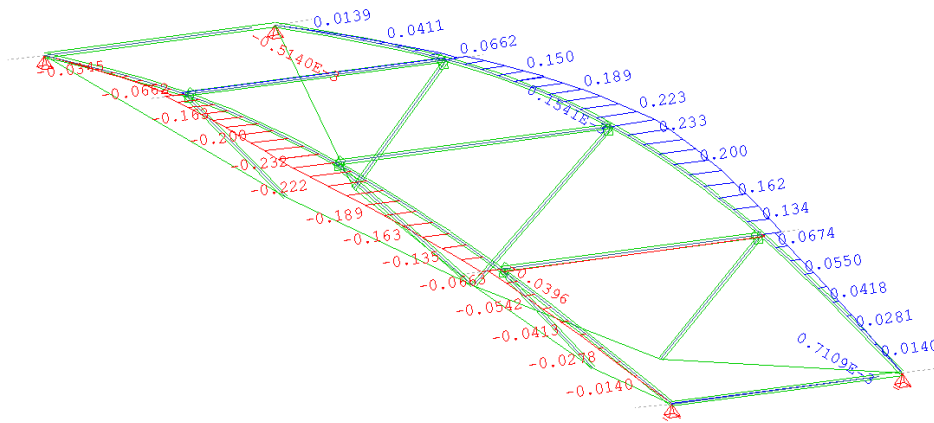


**Figure 102:** Bending moments  $M_z$  (kN.m) in the rod and deviators due to activation process (stage (e)).

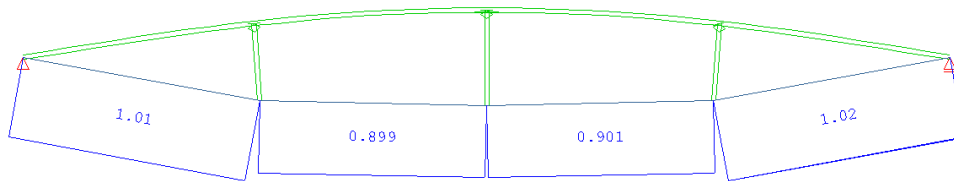


**Figure 103:** Axial forces  $N$  (kN) in cables due to activation process (stage (e)).

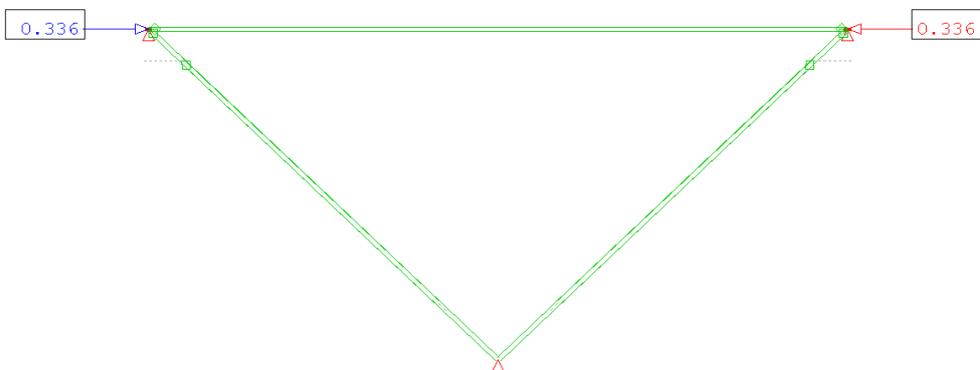


**Figure 104:** Axial forces  $N$  (kN) in midspan strut due to activation process (stage (c)).

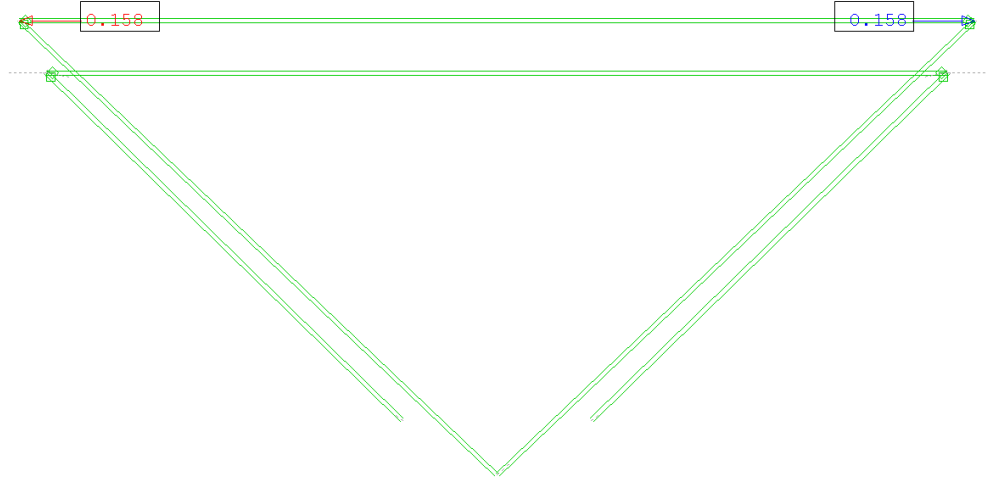


**Figure 105:** Axial forces  $N$  (kN) in midspan strut due to activation process (stage (d)).

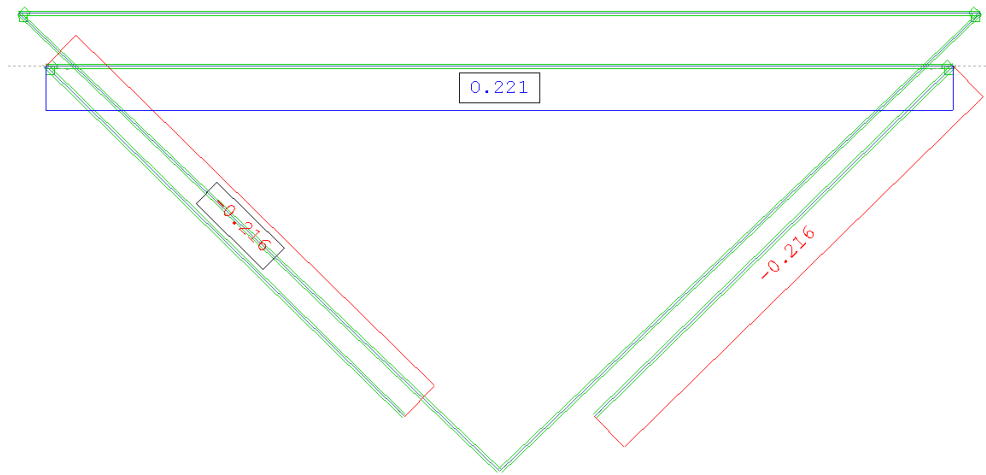


**Figure 106:** Axial forces  $N$  (kN) in quarter strut due to activation process (stage (d)).

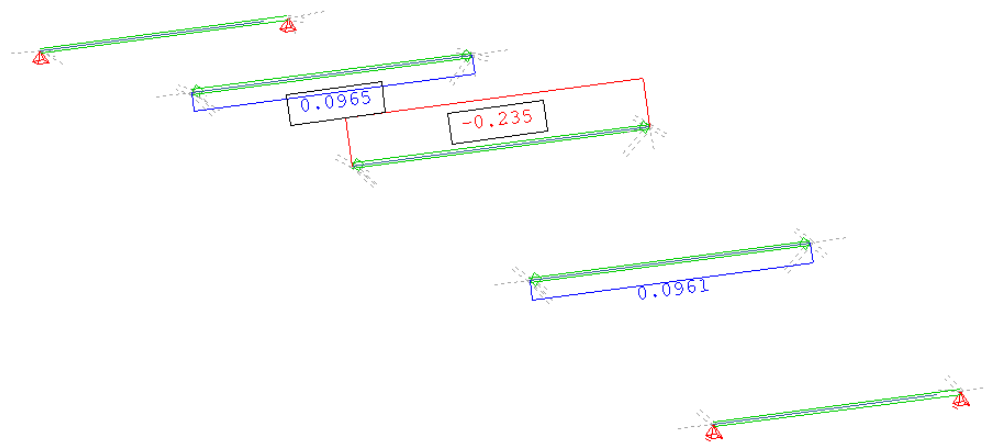


**Figure 107:** Axial forces  $N$  (kN) in midspan and quarter struts due to activation process (stage (e)).

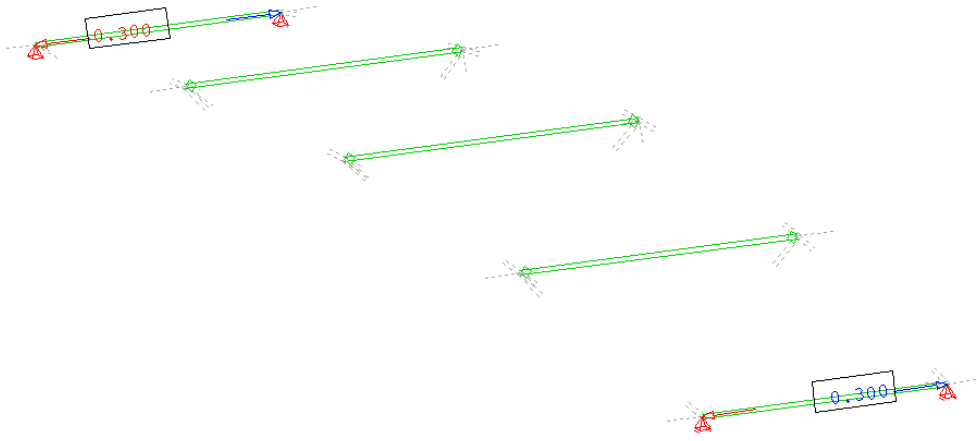


**Figure 108:** Axial forces  $N$  (kN) in end struts due to activation process (stage (e)).

## A.2 LOAD TESTING

### A.2.1 Dead load (pallets)

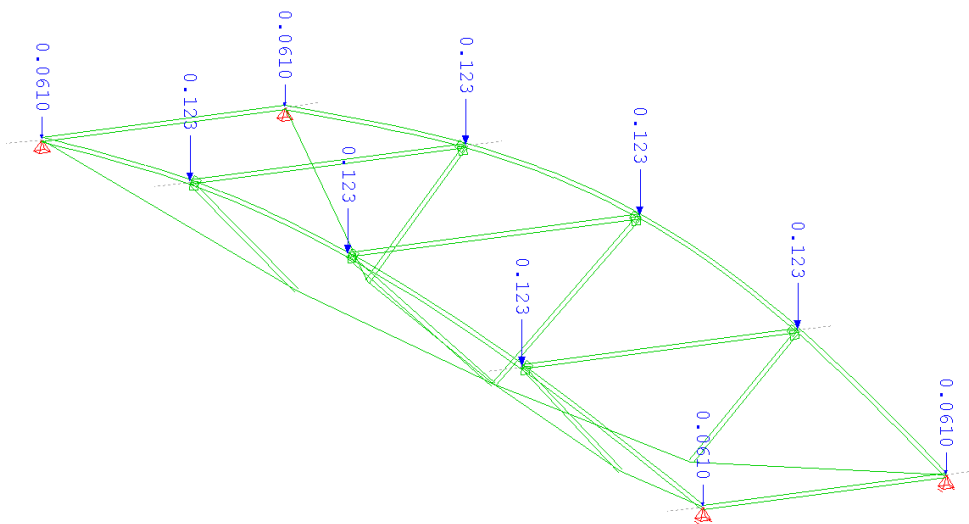


**Figure 109:** Loading pattern (kN) due to the installation of the pallets.



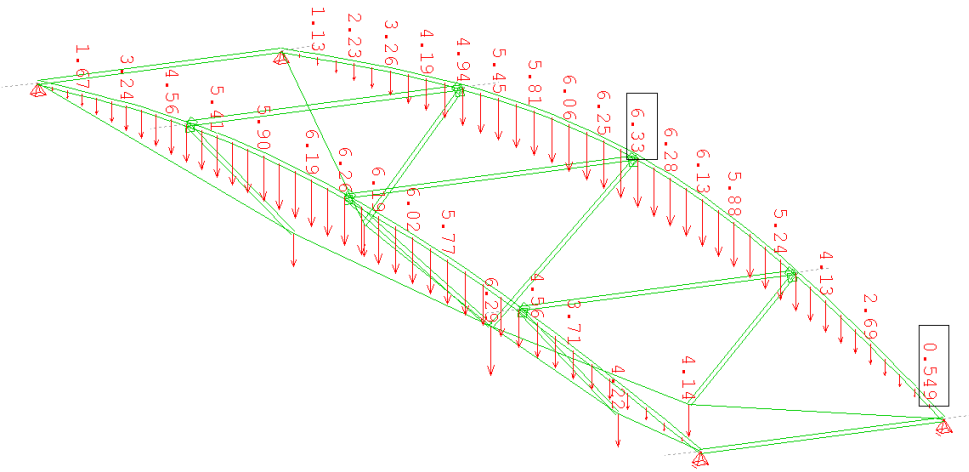


**Figure 114:** Vertical deflections (mm) due to the installation of the pallets.

**A.2.2 Symmetric load case**

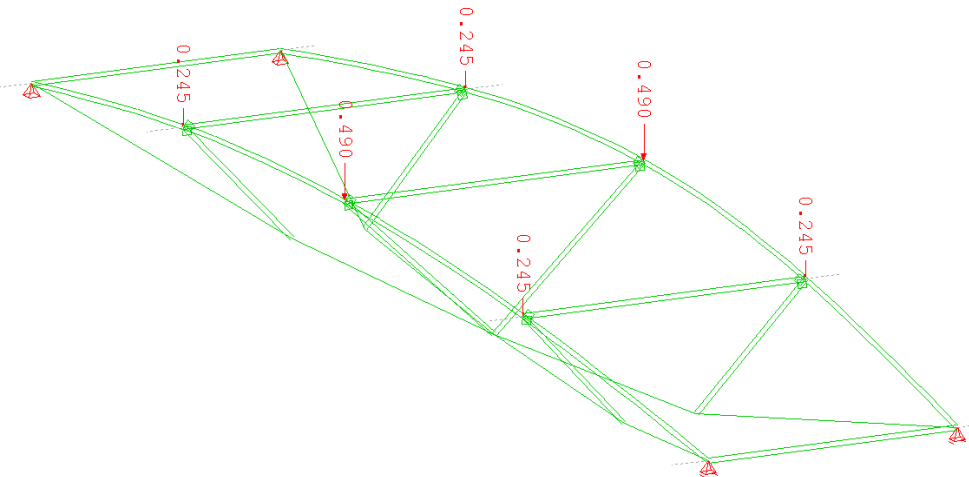


**Figure 115:** Loading pattern (kN) due to the symmetric loading pattern for the load testing.

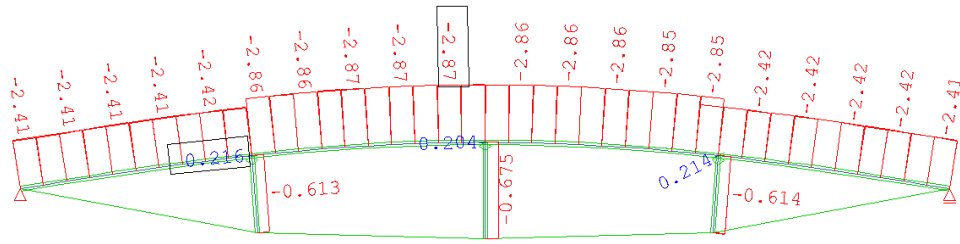


**Figure 116:** Axial forces  $N$  (kN) in the rod and deviators due to the symmetric loading pattern for the load testing.

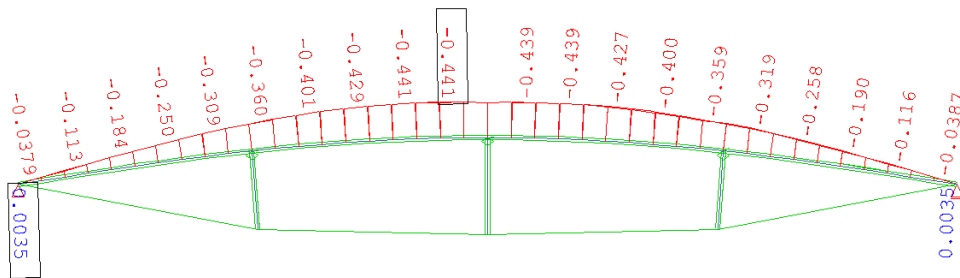


**Figure 117:** Bending moments  $M_y$  (kN.m) in the rod and deviators due to the symmetric loading pattern for the load testing.

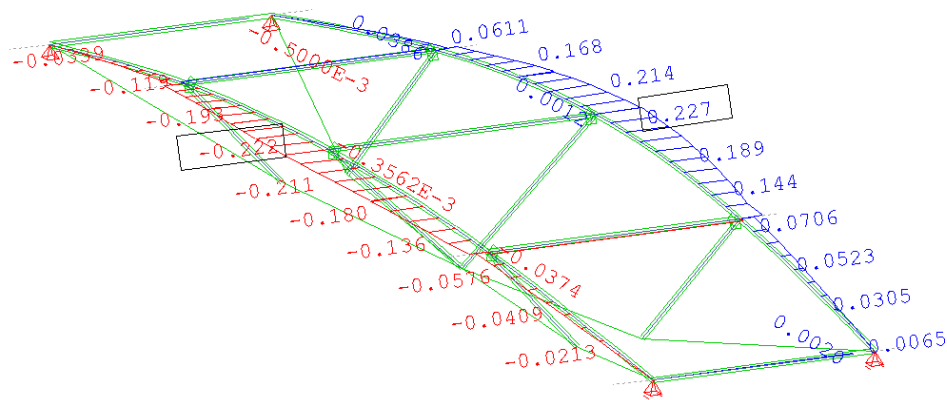


**Figure 118:** Bending moments  $M_z$  (kN.m) in the rod and deviators due to the symmetric loading pattern for the load testing.

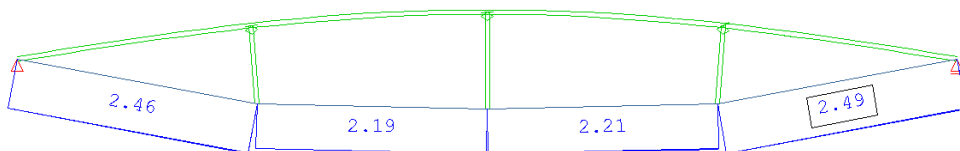


**Figure 119:** Axial forces  $N$  (kN) in cables due to the symmetric loading pattern for the load testing.

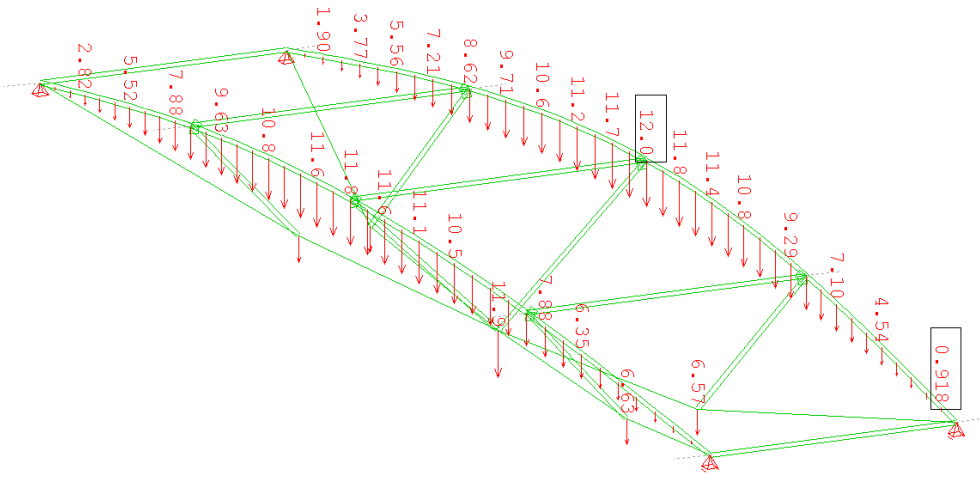


**Figure 120:** Vertical deflections (mm) due to the symmetric loading pattern for the load testing.

### A.2.3 Non-symmetric load case

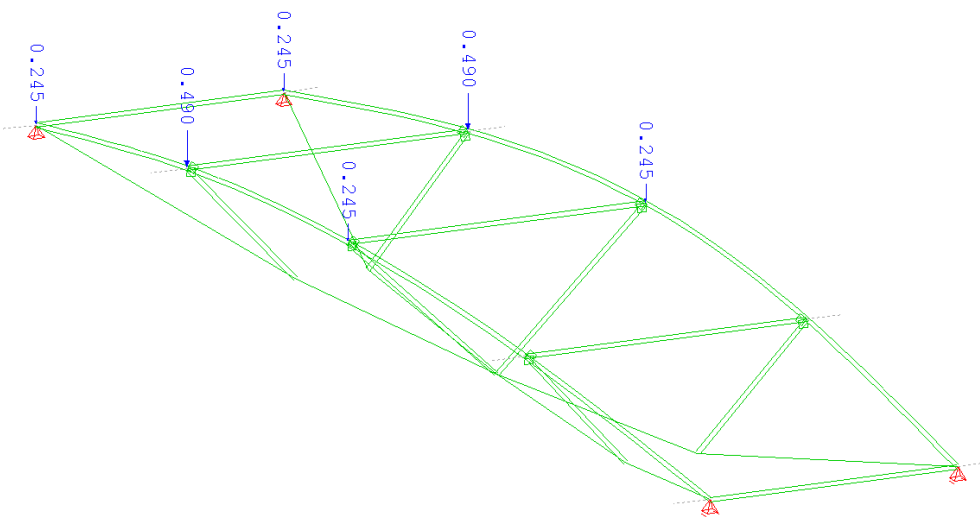


**Figure 121:** Loading pattern (kN) due to the non-symmetric loading pattern for the load testing.



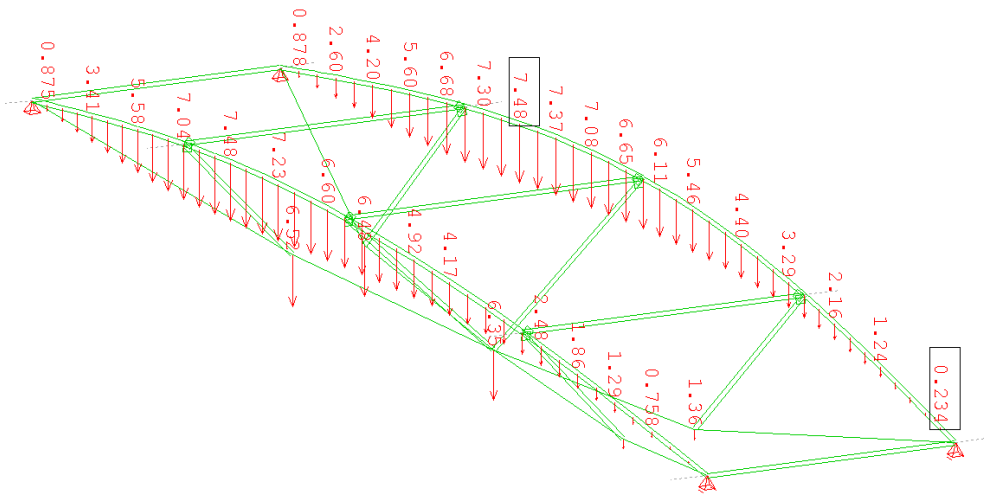


**Figure 126:** Vertical deflections (mm) due to the non-symmetric loading pattern for the load testing.

**A.2.4 Torsional load case**

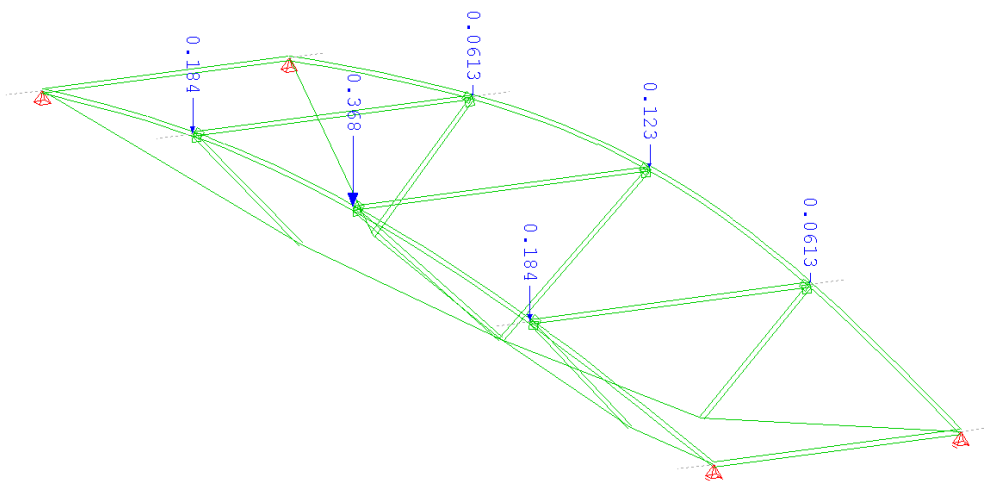


**Figure 127:** Loading pattern (kN) due to the torsional load case for the load testing.

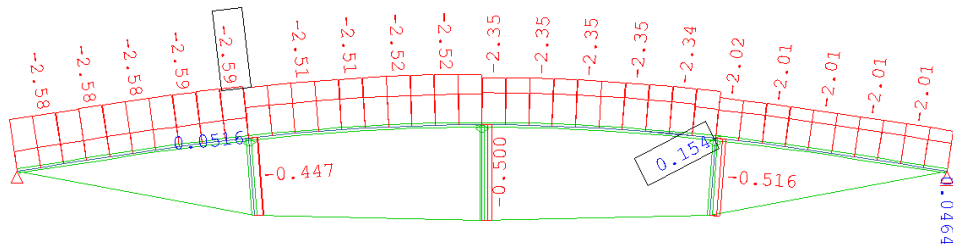


**Figure 128:** Axial forces  $N$  (kN) in the rod and deviators due to the torsional load case for the load testing.

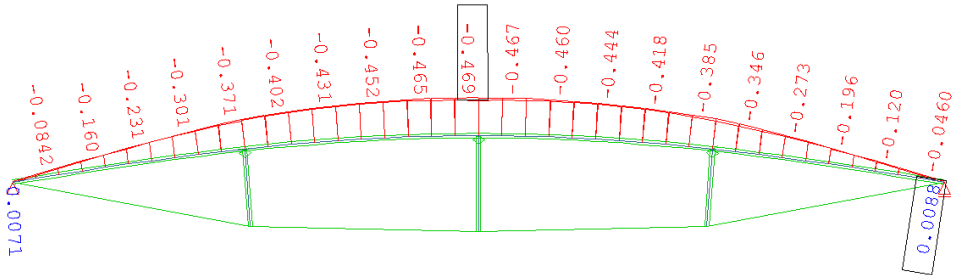


**Figure 129:** Bending moments  $M_y$  (kN.m) in the rod and deviators due to torsional load case for the load testing.

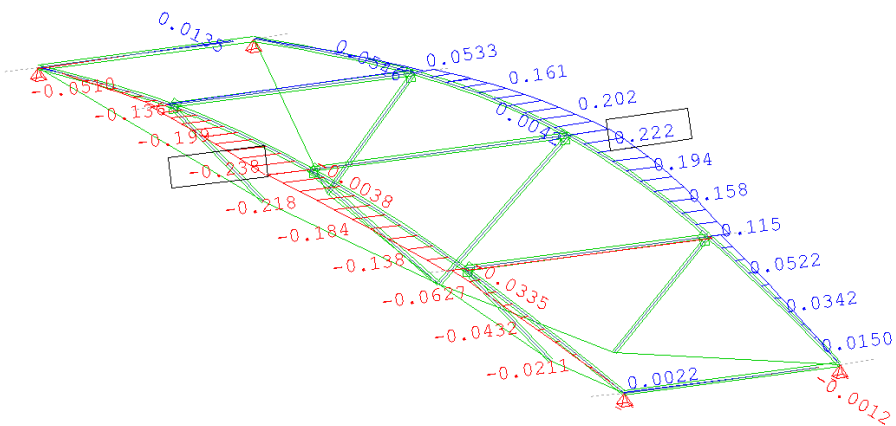


**Figure 130:** Bending moments  $M_z$  (kN.m) in the rod and deviators due to the torsional load case for the load testing.

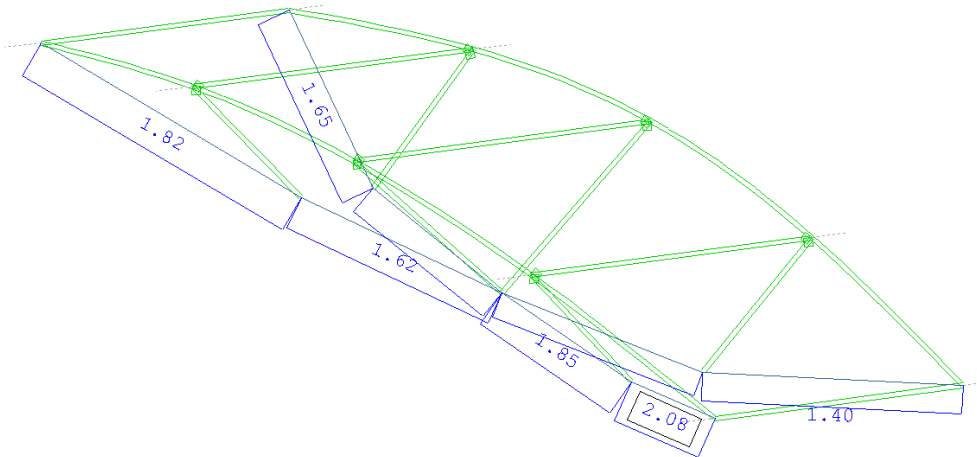


**Figure 131:** Axial forces  $N$  (kN) in cables due to the torsional load case for the load testing.

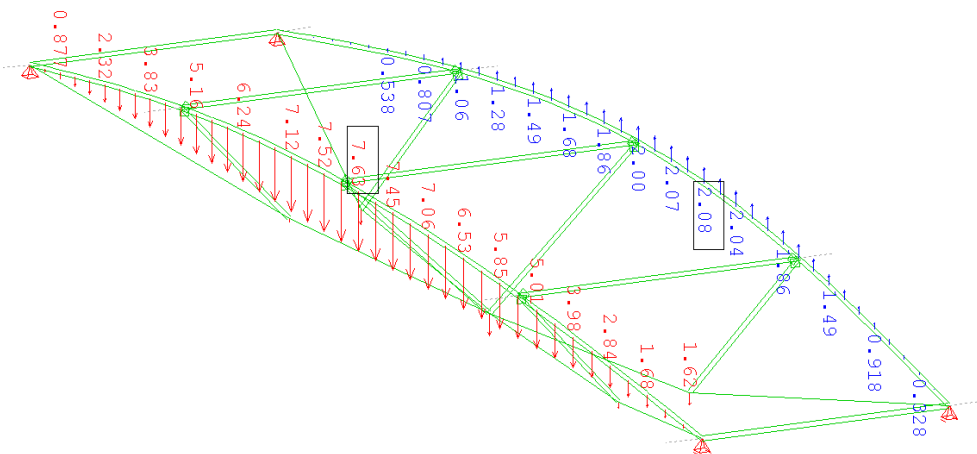


**Figure 132:** Vertical deflections (mm) due to the torsional load case for the load testing.



## ABOUT THE AUTHOR

Juan Gabriel Bessini Muñoz was born in Valencia, Spain on June 20th 1990. He attended his elementary and primary education at the school *Eliseo Vidal* and the secondary education at the school *I.E.S. n° 27 La Misericordia*. Immediately after, he began his studies of Civil Engineering at the School of *Ingenieros de Caminos, Canales y Puertos* at the Universitat Politècnica de València (UPV). He graduated as a Civil Engineer with Honours in his final dissertation in 2014. In September of 2014, he moved to Madrid (Spain) to study the MSc in *Structures, Foundations and Materials Engineering* at the Universidad Politécnica de Madrid (UPM). After finishing his studies, he came back to Valencia to start as a PhD candidate at the *Department of Mechanics of Continuous Media and Theory of Structures* of UPV. During the last five years, he has been investigating computational methods to simulate the structural behaviour of very flexible members and their structural performance. His main target was to understand how novel techniques can help designing lightweight structures. During his research he has been lucky enough to spend some months in the *University of Bath* (UK) as a visiting student. During this stay, he investigated about multi-objective optimisation strategies and parametric models. Also, he has attended to several international scientific conferences in the field of lightweight and spatial structures. *HafenCity University Hamburg* (Germany), *Massachusetts Institute of Technology (MIT)*, Boston (EEUU) or the *Polytechnic University of Barcelona* (Spain) are the most relevant places where he has presented his work. Currently, he is developing his career in the private industry as a structural engineer, bringing together research and practice.



## BIBLIOGRAPHY

- [1] S. Adriaenssens. “Stressed spline structures”. PhD thesis. Bath, 2000.
- [2] S. Adriaenssens, M. Barnes, and C. Williams. “A new analytic and numerical basis for the form-finding and analysis of spline and gridshell structures”. In: *Computing Developments in Civil and Structural Engineering* (1999), pp. 83–91.
- [3] S. Adriaenssens and M. R. Barnes. “Tensegrity spline beam and grid shell structures”. In: *Engineering Structures* 23.1 (2001), pp. 29–36. DOI: [10.1016/S0141-0296\(00\)00019-5](https://doi.org/10.1016/S0141-0296(00)00019-5).
- [4] J. Argyris. “An excursion into large rotations”. In: *Computer Methods in Applied Mechanics and Engineering* 32.1-3 (Sept. 1982), pp. 85–155. ISSN: 00457825.
- [5] F. Armero and J. Valverde. “Invariant Hermitian finite elements for thin Kirchhoff rods II: The linear three dimensional case”. In: *Comput. Methods Appl. Mech. Eng.* 213-216 (2020), pp. 458–485.
- [6] M. F. Ashby. *Material selection in mechanical design*. MRS Bulletin, 2005.
- [7] M. R. Barnes. “Form finding and analysis of tension structures by dynamic relaxation”. In: *International Journal of Space Structures* 14 (1999), pp. 89–104.
- [8] M. R. Barnes, S. Adriaenssens, and M. Krupka. “A novel torsion/bending element for dynamic relaxation modeling”. In: *Computers & Structures* 119 (2013), pp. 60–67. DOI: [10.1016/j.compstruc.2012.12.027](https://doi.org/10.1016/j.compstruc.2012.12.027).
- [9] K. J. Bathe and Bolourchi S. “Large displacement analysis of three-dimensional beam structures”. In: *International Journal for Numerical Methods in Engineering* 14.7 (1979), pp. 961–986.
- [10] A. Bauer. “CAD-integrated isogeometric analysis and design of lightweight structures”. PhD thesis. Munchen, 2020.
- [11] A. Bauer et al. “Nonlinear isogeometric spatial Bernoulli beam”. In: *Computer Methods in Applied Mechanics and Engineering* 303 (2016), pp. 101–127.
- [12] O. Baverel et al. “Concept of a beam prestressed by bending: Application to a footbridge in composite materials”. In: *Journal of the International Association for Shell and Spatial Structures* 51.3 (2010), pp. 99–106.
- [13] T. Belytschko and B. J. Hsieh. “Non-linear transient finite element analysis with convected co-ordinates”. In: *Int. Jour. Numer. Meth. Eng.* 7 (1973), pp. 255–271. DOI: [10.1002/nme.1620070304](https://doi.org/10.1002/nme.1620070304).
- [14] M. Bergou et al. “Discrete elastic rods”. In: *ACM Transactions on Graphics* 27 (2008). DOI: [10.1145/1360612.1360662](https://doi.org/10.1145/1360612.1360662).
- [15] F. Bertails et al. “Super-helices for predicting the dynamics of natural hair”. In: *Proceedings of ACM SIGGRAPH 2006*. Vol. 25. ACM Transactions on Graphics 3. 2006.
- [16] J. Bessini, C. Lázaro, and S. Monleón. “A form-finding method based on the geometrically exact rod model for bending-active structures”. In: *Engineering Structures* 152 (2017), pp. 549–558.

- [17] J. Bessini et al. “Design of an experimental lightweight footbridge based on the active bending principle”. In: *Proceedings of the IASS Annual Symposium 2018*. Boston, 2018.
- [18] J. Bessini et al. “Efficiency-based design of bending-active tied arches”. In: *Engineering Structures* 200, 109681 (2019).
- [19] R. L. Bishop. “There is more than one way to frame a curve”. In: *The American Mathematical Monthly* 82.3 (1975), pp. 246–251.
- [20] S. Bouaziz et al. “Shape-up: Shaping discrete geometry with projections”. In: *Comput. Graph. Forum* 31 (2012), pp. 1657–1667.
- [21] L. Bouhaya, O. Baverel, and J. F. Caron. “Optimization of gridshell bar orientation using a simplified genetic approach”. In: *Structural and Multidisciplinary Optimization* 50 (2014), pp. 839–848.
- [22] L. Boulic and J. Schwartz. “Design Strategies of Hybrid Bending-Active Systems Based on Graphic Statics and a Constrained Force Density Method”. In: *Journal of the International Association for Shell and Spatial Structures* 54.4 (2018), pp. 267–275. DOI: [10.20898/j.iass.2018.198.038](https://doi.org/10.20898/j.iass.2018.198.038).
- [23] S. Brancart et al. “Bending-active reciprocal structures based on equilateral polyhedral geometries”. In: *Proceedings of the IASS Annual Symposium 2017*. 2017.
- [24] C. Brandt-Olsen. *K2Engineering*. <https://github.com/CecilieBrandt/K2Engineering>. Accessed: 2020-07-23.
- [25] A. Cardona and M. Geradin. “A beam finite element non-linear theory with finite rotations”. In: *Int. Jour. Numer. Meth. Eng.* 26 (1988), pp. 2403–2438. DOI: [10.1002/nme.1620261105](https://doi.org/10.1002/nme.1620261105).
- [26] J. F. Caron, S. Julich, and O. Baverel. “Selfstressed bowstring footbridge in FRP”. In: *Composite Structures* 89.3 (2009), pp. 489–496. ISSN: 0263-8223. DOI: <https://doi.org/10.1016/j.compstruct.2008.11.009>.
- [27] M. A. Crisfield. *Non-linear Finite Element Analysis of Solids and Structures. Volume 2: Advanced Topics*. John Wiley & Sons, 1997.
- [28] M. A. Crisfield and G. Jelenić. “Objectivity of strain measures in the geometrically exact three-dimensional beam theory and its finite-element implementation”. In: *Proceedings of the Royal Society A: Mathematical, Physical and Engineering Sciences* 455.1983 (Mar. 1999), pp. 1125–1147. DOI: [10.1098/rspa.1999.0352](https://doi.org/10.1098/rspa.1999.0352).
- [29] P. Cuvilliers et al. “A comparison of two algorithms for the simulation of bending-active structures”. In: *Int. J. Sp. Struct* (2018).
- [30] B. D’Amico, A. Kermani, and H. Zhang. “Form finding and structural analysis of actively bent timber grid shells”. In: *Engineering Structures* 81 (2014), pp. 195–207. DOI: [10.1016/j.engstruct.2014.09.043](https://doi.org/10.1016/j.engstruct.2014.09.043).
- [31] B. D’Amico, H. Zhang, and A. Kermani. “A finite-difference formulation of elastic rod for the design of actively bent structures”. In: *Engineering Structures* 117 (2016), pp. 518–527. DOI: [10.1016/j.engstruct.2016.03.034](https://doi.org/10.1016/j.engstruct.2016.03.034).
- [32] B. D’Amico et al. “A finite-difference formulation of elastic rod for the design of actively bent structures”. In: *Comput. Struct.* 117 (2015), pp. 163–176. DOI: [10.1016/j.compstruc.2015.04.006](https://doi.org/10.1016/j.compstruc.2015.04.006).

- [33] A. Day. “An introduction to dynamic relaxation”. In: *Engineer 1965* 331.219 (May 1965), pp. 218–221.
- [34] C. Douthe. “Etude de structures élancées précontraintes en matériaux composites : application à la conception des gridshells”. 2007ENPC0728. PhD thesis. 2007. URL: <http://www.theses.fr/2007ENPC0728/document>.
- [35] C. Douthe, O. Baverel, and J. F. Caron. “Form-finding of a Grid Shell in Composite Material”. In: *Journal of the International Association for Shell and Spatial Structures* 47 (2006), pp. 53–62.
- [36] C. Douthe, O. Baverel, and J. F. Caron. “Gridshell in composite materials: Towards wide span shelters”. In: *Journal of the International Association for Shell and Spatial Structures* 48.3 (2007), pp. 175–180.
- [37] C. Douthe, J. F. Caron, and O. Baverel. “Gridshell structures in glass fibre reinforced polymers”. In: *Construction and Building Materials* 24.9 (2010), pp. 1580–1589.
- [38] L. Du Peloux. “Modeling of bending-torsion couplings in active-bending structures : application to the design of elastic gridshells”. PhD thesis. 2017.
- [39] L. Du Peloux et al. “Formulation of a 4-DoF torsion/bending element for the formfinding of elastic gridshells”. In: *Proceedings of the IASS Symposium 2015*. Amsterdam, 2015, pp. 1–15.
- [40] L. Du Peloux et al. “From shape to shell: a design tool to materialize freeform shapes using gridshell structures”. In: *Design Modeling Symposium*. Berlin, Deutschland, 2011.
- [41] *EN 1991-2 Eurocode 1: Actions on structures - Part 2: Traffic loads on bridges*. 2003.
- [42] *EN 1993-1-1 Eurocode 3: Design of steel structures - Part 1-1: General rules and rules for buildings*. 2005.
- [43] E. Happold and W. Liddell. “Timber lattice roof for the Mannheim Bundesgartenschau”. In: *The Structural Engineer* 53.3 (1975), pp. 99–135.
- [44] J. Harding et al. “The Ongreening Pavilion”. In: *Advances in Architectural Geometry 2014*. Springer International Publishing, 2014, pp. 295–308.
- [45] O. Hasańceby and F. Erbatur. “Evaluation of crossover techniques in genetic algorithm based optimum structural design”. In: *Computer & Structures* 78 (2000), pp. 435–448.
- [46] A. Ibrahimbegovic. “On finite element implementation of geometrically non-linear Reissner’s beam theory: three-dimensional curved beam elements”. In: *Comput. Meth. Appl. Mech. Eng.* 11 (1995), pp. 11–26. DOI: [10.1016/0045-7825\(95\)00724-F](https://doi.org/10.1016/0045-7825(95)00724-F).
- [47] A. Ibrahimbegovic. “On the geometrically exact formulation of structural mechanics and its applications to dynamics, control and optimization”. In: *Comptes Rendus Mécanique* 331.5 (May 2003), pp. 383–394. DOI: [10.1016/S1631-0721\(03\)00062-7](https://doi.org/10.1016/S1631-0721(03)00062-7).
- [48] McCall J. “Genetic algorithms for modelling and optimisation”. In: *Journal of Computational and Applied Mathematics* 184 (2005), pp. 205–222.

- [49] G. Jelenić and M. A. Crisfield. “Geometrically exact 3D beam theory: implementation of a strain-invariant finite element for statics and dynamics”. In: *Computer Methods in Applied Mechanics and Engineering* 171.1-2 (Mar. 1999), pp. 141–171. DOI: [10.1016/S0045-7825\(98\)00249-7](https://doi.org/10.1016/S0045-7825(98)00249-7).
- [50] A. Konak, D. Coit, and A. Smith. “Multi-objective optimization using genetic algorithms: A tutorial”. In: *Reliability Engineering & System Safety* 91 (2006), pp. 992–1007.
- [51] N. Kotelnikova-Weiler et al. “Materials for actively-bent structures”. In: *International Journal of Space Structures* 28.3-4 (2013), pp. 229–240.
- [52] B. Kromoser and J. Kollegger. “Pneumatic forming of hardened concrete - building shells in the 21st century”. In: *Struct. Concr.* 16.2 (2015), pp. 161–171.
- [53] R. La Magna. *Bending-Active Plates :Strategies for the Induction of Curvature through the Means of Elastic Bending of Plate-based Structures*. Ed. by Jan Knippers. Universität Stuttgart - Institut für Tragkonstruktionen und Konstruktives Entwerfen, 2017.
- [54] P. Längst et al. “The potentials of isogeometric analysis methods in integrated design processes”. In: *Proceedings of the IASS Annual Symposium 2017 - Interfaces: architecture.engineering.science*. Hamburg, 25–25 September 2017. 2017.
- [55] C. Lázaro. “Formulación material y espacial del modelo geoméricamente exacto de piezas alargadas”. PhD thesis. 2005.
- [56] C. Lázaro, J. Bessini, and S. Monleón. “Mechanical models in computational form finding of bending-active structures”. In: *International Journal of Space Structures* 33.2 (2018), pp. 86–97. DOI: [10.1177/0266351118794277](https://doi.org/10.1177/0266351118794277).
- [57] C. Lázaro, J. Bessini, and S. Monleón. “Shape and performance of bending-active tied arches”. In: *Proceedings of the IASS Annual Symposium 2018*. Boston, 2018.
- [58] C. Lázaro, S. Monleón, and J. Bessini. “Tangent stiffness in point-loaded elastica arches”. In: *Proceedings of the IASS Annual Symposium 2017*. Hamburg, 2017.
- [59] C. Lázaro, S. Monleón, and J. Casanova. “Can the force density method be extended for active bending structures?” In: *Proceedings of the IASS Annual Symposium 2015*. Amsterdam, 2015.
- [60] C. Lázaro et al. “A review on geometrically exact models for very flexible rods”. In: *Proceedings of the IASS Annual Symposium 2016*. Tokyo, 2016.
- [61] B. Lefevre, C. Douthe, and O. Baverel. “Buckling of elastic gridshells”. In: *Journal of the International Association for Shell and Spatial Structures* 56.3 (2015), pp. 153–171.
- [62] B. Lefevre et al. “A 4-degree-of-freedom Kirchhoff beam model for the modeling of bending–torsion couplings in active-bending structures”. In: *International Journal of Space Structures* 32.2 (June 2017), pp. 69–83.
- [63] J. Li and J. Knippers. “Rotation formulations for dynamic relaxation – with application in 3D framed structures with large displacements and rotations”. In: *Proceedings of the IASS-APCS Symposium 2012*. Seoul, 21–24 May 2012. 2015.

- [64] J. Lienhard. *Bending-active structures : Form-finding strategies using elastic deformation in static and kinetic systems and the structural potentials therein*. Ed. by Jan Knippers. itke Forschungsberichte 36. Universität Stuttgart - Institut für Tragkonstruktionen und Konstruktives Entwerfen, 2014.
- [65] J. Lienhard, R. La Magna, and J. Knippers. “Form-finding bending-active structures with temporary ultra-elastic contraction elements”. In: *WIT Transactions on the Built Environment* 136 (2014), pp. 107–116. DOI: [10.2495/MAR140091](https://doi.org/10.2495/MAR140091).
- [66] J. Lienhard, S. Schleicher, and J. Knippers. “Bending-active Structures – Research Pavilion ICD/ITKE”. In: *Proceedings of the IABSE-IASS Symposium – Taller, Longer, Lighter*. Ed. by Dennis Nethercot and Sergio Pellegrino. 2011.
- [67] AEH. Love. *A Treatise on the Mathematical Theory of Elasticity*. New York: Dover, 1944.
- [68] C. Meier, A. Popp, and W. A. Wall. “An objective 3D large deformation finite element formulation for geometrically exact curved Kirchhoff rods”. In: *Comput. Methods Appl. Mech. Eng.* 278 (2014), pp. 445–478.
- [69] P. Nicholas, E. Lafuente-Hernández, and C. Gengnagel. “The Faraday Pavilion: activating bending in the design and analysis of an elastic gridshell”. In: *Proceedings of the Symposium on Simulation for Architecture & Urban Design (SimAUD 2013)*. San Diego (CA), USA, 7–10 April, 2013. Society for Modeling & Simulation International, 2013, pp. 154–161.
- [70] K. Noda and Y. Kanebako. “Structural design of pre-bent dimensional lumber suspenarches”. In: *Proceedings of the IASS Annual Symposium 2018*. Boston, 2018.
- [71] J. R. H. Otter et al. “Dynamic relaxation”. In: *Proceedings of the Institution of Civil Engineers* 35.4 (Dec. 1966), pp. 633–656. DOI: [10.1680/iicep.1966.8604](https://doi.org/10.1680/iicep.1966.8604).
- [72] F. Otto, J. Henniske, and K. Matsushita. *IL10 - Gitterschalen*. Stuttgart, 1974.
- [73] D. Piker. *How does Kangaroo solver work?* <https://discourse.mcneel.com/t/how-does-kangaroo-solver-work/92075/3/>. Accessed: 2020-07-22.
- [74] D. Piker. *KANGAROO PHYSICS*. <https://www.food4rhino.com/app/kangaroo-physics/>. Accessed: 2020-07-22.
- [75] D. Piker. “Kangaroo: Form finding with computational physics”. In: *Architectural Design* 83.2 (2013).
- [76] S. Pone et al. “Construction and form-finding of a post-formed timber gridshell”. In: *Structures and Architecture: Concepts, Applications and Challenges - Proceedings of the 2nd International Conference on Structures and Architecture (ICSA 2013)*. Guimaraes, Portugal, 24–26 July 2013. CRC Press, 2013, pp. 245–252.
- [77] S. Pone et al. “Specialised algorithms for different project stages in a post-formed timber gridshell design”. In: *Proceedings of the 3rd International Conference on Structures and Architecture*. Guimarães, Portugal, 2016.

- [78] P.M. Reis. “A perspective on the Revival of Structural (In) Stability With Novel Opportunities for Function: From Buckliphobia to Buckliphia”. In: *J. Appl. Mech.* 82.1 (2015).
- [79] E. Reissner. “On one-dimensional finite-strain beam theory: The plane problem”. In: *Stud. Appl. Math.* 52 (1973), pp. 87–95. DOI: [10.1007/BF01602645](https://doi.org/10.1007/BF01602645).
- [80] M. Ritto-Corrêa and D. Camotim. “On the differentiation of the Rodrigues formula and its significance for the vector-like parameterization of Reissner-Simo beam theory”. In: *International Journal for Numerical Methods in Engineering* 55.9 (Nov. 2002), pp. 1005–1032. ISSN: 00295981. DOI: [10.1002/nme.532](https://doi.org/10.1002/nme.532).
- [81] J. Rombouts et al. “A novel shape optimization approach for strained gridshells: Design and construction of a simply supported gridshell”. In: *Engineering Structures* 192 (2019), pp. 166–180. ISSN: 0141-0296. DOI: <https://doi.org/10.1016/j.engstruct.2019.04.101>. URL: <http://www.sciencedirect.com/science/article/pii/S0141029618336071>.
- [82] D. Rutten. “Galapagos: On the Logic and Limitations of Generic Solvers”. In: *Architectural Design* 83.2 (2013), pp. 132–135. DOI: [10.1002/ad.1568](https://doi.org/10.1002/ad.1568).
- [83] M. Saitoh. “40 years after-development and possibility of beam string structures”. In: *Proceedings of the IASS Annual Symposium 2019*. 2019.
- [84] Y. Sakai and M. Ohsaki. “Discrete elastica for shape design of gridshells”. In: *Engineering Structures* 169 (2018), pp. 55–67. ISSN: 0141-0296. DOI: <https://doi.org/10.1016/j.engstruct.2018.05.002>. URL: <http://www.sciencedirect.com/science/article/pii/S0141029617338695>.
- [85] Y. Sakai, M. Ohsaki, and S. Adriaenssens. “A 3-dimensional elastic beam model for form-finding of bending-active gridshells”. In: *International Journal of Solids and Structures* 193-194 (2020), pp. 328–337. ISSN: 0020-7683. DOI: <https://doi.org/10.1016/j.ijsolstr.2020.02.034>. URL: <http://www.sciencedirect.com/science/article/pii/S0020768320300810>.
- [86] E. Schling et al. “Design and construction of the asymptotic pavilion”. In: *VIII International Conference on Textile Composites and Inflatable Structures*. Structural Membranes 2017, 207.
- [87] M. Seixas et al. “Active Bending and Tensile Pantographic Bamboo Hybrid Amphitheater Structure”. In: *J. Int. Assoc. Shell Spat. Struct.* 58.3 (2017).
- [88] G. Senatore and D. Piker. “Interactive real-time physics: An intuitive approach to form-finding and structural analysis for design and education”. In: *Computer-Aided Design* 61 (2015), pp. 32–41. DOI: [10.1016/j.cad.2014.02.007](https://doi.org/10.1016/j.cad.2014.02.007).
- [89] J. C. Simo. “A finite strain beam formulation. The three-dimensional dynamic problem. Part I”. In: *Computer Methods in Applied Mechanics and Engineering* 49.1 (1985), pp. 55–70. DOI: [10.1016/0045-7825\(85\)90050-7](https://doi.org/10.1016/0045-7825(85)90050-7).
- [90] J. C. Simo and L. Vu-Quoc. “A geometrically-exact rod model incorporating shear and torsion-warping deformation”. In: *International Journal of Solids and Structures* 27.3 (1991), pp. 371–393.
- [91] I. Sobol. “Uniformly distributed sequences with an additional uniform property”. In: *USSR Computational Mathematics and Mathematical Physics* 16(5) (1976), pp. 236–242.

- [92] V. Sonnevile, A. Cardona, and O. Bruls. “Geometrically exact beam finite element formulated on the special euclidean group  $SE(3)$ ”. In: *Comput. Meth. Appl. Mech. Eng.* 268 (2014), pp. 451–474. DOI: [10.1016/j.cma.2013.10.008](https://doi.org/10.1016/j.cma.2013.10.008).
- [93] E. L. Starostin and G. H. M. Van Der Heijden. “The shape of a Möbius strip”. In: *Nature Materials* 6 (2007), pp. 563–567. DOI: [10.1038/nmat1929](https://doi.org/10.1038/nmat1929).
- [94] GMBH structure and TUM. *Kiwi!3D*. <https://www.kiwi3d.com/>. Accessed: 2020-07-12.
- [95] T. Teschemacher et al. “Realization of CAD-integrated shell simulation based on isogeometric B-rep analysis”. In: *Adv. Model. Simul. Eng. Sci.* 5.1 (2018).
- [96] D. Wakefield. “Dynamic relaxation analysis of pretensioned networks supported by compression arches”. PhD thesis. London, 1980.
- [97] Wikipedia. *Yurt*. <https://en.wikipedia.org/wiki/Yurt>. Accessed: 2020-07-23.
- [98] O. C. Zienkiewicz and R. L. Taylor. *Finite Element Method: Volume 2, Solid Mechanics*. Boston: Butterworth-Heinemann, 2000.